Measurements of the drift velocity using a small gas chamber for monitoring of the CMS muon system

von

Jens Frangenheim

vorgelegt der

Fakultät für

Mathematik, Informatik und Naturwissenschaften

der Rheinisch-Westfälischen Technischen Hochschule Aachen

im Juni 2007

angefertigt im

III. Physikalischen Institut A

Professor Dr. Thomas Hebbeker

Zweitgutachter: Professor Dr. Christopher Wiebusch

Abstract

This diploma thesis presents measurements of the drift velocity of electrons in gas. A small gas detector (VDC[1]) is used. This chamber is intended for measurement and monitoring of the drift velocity in the gas of the muon chambers of the gas detector system in the barrel area of the CMS-detector[2] at the European Research Center for Particle Physics CERN near Geneva.

The drift velocity is, together with the drift time, a key parameter for measurements with drift chambers.

The aim of this thesis is to perform test measurements to determine parameters of the chamber and also to estimate systematic errors.

Beside the drift velocity, further parameters of the gas like the pressure and the temperature are measured and accounted for. For the further work with the VDCs, analysis software has been created which is used for the analysis of the measurements.

Parallel to this work, necessary improvements, e.g. for the high voltage robustness, were also implemented and tested.

In addition, studies and test measurements are done to develop a new trigger system based on small semiconductor light detectors.

---

[1]**V**elocity **D**rift **C**hamber
[2]**C**ompact **M**uon **S**olenoid

Zusammenfassung

Diese Diplomarbeit behandelt Messungen der Driftgeschwindigkeit von Elektronen in Gas. Ein kleiner Gasdetector (VDC[3]) wird benutzt. Dieser ist für die Messung und Überwachung der Driftgeschwindigkeit im Gas für die Myonkammern des Gasdetektorsystems im zentralen Bereich des CMS-Detektors[4] am Europäischen Forschungszentrum für Teilchenphysik CERN bei Genf vorgesehen.

Die Driftgeschwindigkeit ist, zusammen mit der Driftzeit, grundlegender Messparameter der Teilchendetektorart Driftkammer.

Ziel dieser Arbeit ist es, Testmessungen durchzuführen und damit Parameter der Kammer einzustellen sowie systematische Fehler zu ermitteln und zu bestimmen.

Neben der Driftgeschwindigkeit werden weitere Parameter wie Druck und Temperatur gemessen und in die Auswertung mit einbezogen.

Für die weitere Arbeit mit dem Messsystem werden entsprechende Auswertungsprogramme erstellt.

Parallel zu dieser Arbeit werden notwendige Verbesserungen, wie z.B. für die Hochspannungsfestigkeit, vollzogen und getestet.

Zusätzlich werden Studien und Testmessungen gemacht, um ein neues Auslösesystem basierend auf kleinen Halbleiterlichtdetektoren zu entwickeln.

---

[3]**V**elocity **D**rift **C**hamber
[4]**C**ompact **M**uon **S**olenoid

Contents

Contents

Contents

1. Introduction

1.1. Particle physics

The foundation of modern physics are the mathematical methods established by Sir Isaac Newton (1643-1727), who has built the basic for the systematical exploration of natural phenomena. Modern physics tries to find laws for processes in nature and to understand the composition of structures in order to predict processes in nature. In order to test and find such laws, nature is investigated by experiments.

Elementary particle physics was termed "high energy physics" in the past in allusion of certain experimental methods. Today's name describes the contents more accurately. Elementary particle physics can be considered as the most basic branch of physics and its roots are as old as mankind itself and it reaches much more backward than Newton's time.

1.1.1. Aims of Present Particle Physics

> Wissen, was die Welt im Innersten zusammenhält [Goe87].

The target of elementary particle physics is the exploration of the constituents of matter and its interactions. Almost 2600 years ago the Greek philosopher Demokrit introduced the concept of atoms and created the fundamental idea of an "elementary particle". The definition of the item elementary particle has its origin in philosophy. The following definition should be universally valid:

> *An elementary particle is not divisible, it has no inner structure and is point like* [Berg02].

These attributes are proven for today's elementary particles down to a maximum size of 10^{-18} m. By definition of the term elementary particle the targets of elementary particle physics are fixed:

- Find the composition of matter to resolve smaller and smaller structures (particles).

- Discover simple and uniform descriptions of the basic particle interactions.

The final aim could be the postulation of a so called "Theory Of Everything", which describes all interactions grounded on a basic principle.

1.1.2. History of Particle Physics

As stated above Demokrit introduced the concept of atoms 600 years BCE and thus the first elementary particles. Already the Greek considered the world to be made of four elements: earth, water, air and fire, see Fig. 1.1.
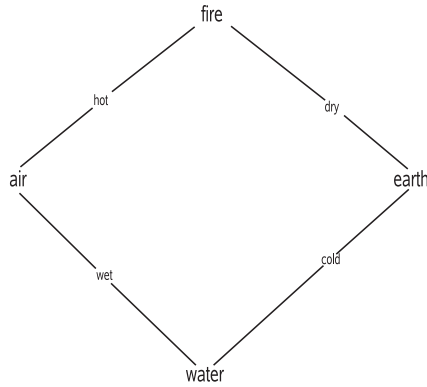
Figure 1.1.: *The four classical elements [Wik07].*

This picture already implied a considerable amount of unification. There is a low number of elements corresponding to elementary particles and there is a simple way of conversation/interaction between the constituents.

For a long time it was questionable if matter is divisible or if it consists of indivisible constituents. Not until the 19th century this question was picked up by Dalton in favor of the indivisibility, who revealed the law of constant mass proportions. Within chemistry Julius Lothar Meyer (1830-1895) and Dmitri Ivanovich Mendeleev (1834-1907) created a list of elementary particles by establishing the periodic system of the elements. The hypothesis of indivisible atoms was disproved indirectly by Ernest Rutherford (1871-1937) in 1919 by the first artificial nuclear reaction, where one element was transformed into another. In 1938 the fission of atomic nuclei was demonstrated by Otto Hahn (1879-1668) and collaboration. The discovery of today's elementary particles started in 1897 with the discovery of the electron by Joseph John Thomson (1856-1956) and the direct measurements of the tau neutrino in 2000 by the DONUT experiment[1] [Hal84, Fey87] is the latest found elementary particle.

1.2. Technique of Particle Physics

To study elementary particles and their interactions microscopes are needed to resolve smaller and smaller structures with higher and higher resolution.

Similar to a light microscope, where the resolution is limited by the wave length, the uncertainly relation for the space component Δx and the momentum component Δp:

$$\Delta x \cdot \Delta p > \frac{\hbar}{2} \tag{1.1}$$

$\hbar$ = Plank's constant $/2\pi$) holds for general purposes. With a large momentum transfer Δp it is possible to resolve small structures Δx. To compare this with light microscopes one has to write the wave length as $\lambda = h/p$ (h = Plank's constant). Thus, to resolve small structures of the size x (or λ) one needs a particle with high momentum. This is the basis of accelerator physics (1.2.1).

1.2.1. Accelerator Physics

In an accelerator experiment (charged) particles are brought to high energies and therefore high momenta to explore small structures. If these particles collide with others they (or the particles

---

[1]a fixed target experiment at Fermi lab (Chicago)

of their substructure) will scatter or new particles will be produced using the kinetic energy[2]. Using these processes the interactions between the particles or their substructure resp. the new particles can be studied. Therefore around the place of collision suitable experiments (the detectors) are built which measure and trace the scattered/produced particles.

1.2.2. Astro(particle) Physics

Here high energetic particles do not come from human-built accelerators but from space. The density of particles is much lower and is not suitable for collision experiments. But cosmic particles reach energies which are far above the energies that can be achieved by accelerators. By determining the source of those particles, information about astronomic objects can be gained.

1.2.3. High Precision Experiments

Also at energy scales which are much below the maximal technically reachable energies, or even at very small energy scales, hints of new elementary particles and specific phenomena can be found. With high precision hints to effects (and particles) at higher energy scales can be detected. Important examples are the (g-2)-experiments[3] [BNL07].

1.3. Outline

This diploma thesis will deal with accelerator physics (Sec. 1.2.1). It deals with a part of an experimental setup to discover new particles like the Higgs boson (Sec. 2.5) or Susy particles (Sec. 2.7.1), new interactions in the form of new gauge bosons (e.g. W') or to reveal substructures of matter (Sec. 2.7.2).

The name of the experimental setup is the **L**arge **H**adron **C**ollider [LHC07]. It consists of a 27 km long tunnel in form of a circle in which high energy particles, protons, are collided. Four experiments detect the particles produced in proton-proton or heavy ion collisions and try to find hints for new phenomena. One of these experiments is the **C**ompact **M**uon **S**olenoid Detector, a general purpose detector. It consists of several sub detectors.

One of these sub detectors is the Barrel Muon System which includes the muon chambers (drift chambers, Chap. 4). In these detectors traversing charged particles generate free electrons. These electrons drift through the gas inside the chambers with a certain velocity before they are registered. The drift velocity has to be known precisely because it is needed to calculate the path length of the traversing particles. It depends very strongly on the gas quality and purity. Thus, by e.g. leaks in the gas system, the drift velocity can change.

To monitor the drift velocity in the gas, special small drift chambers, called **V**elocity **D**rift **C**hambers, will be installed monitoring the gas flowing into and out of the muon chambers. The setup, test and improvements of these VDCs and measurements with these chambers will be the object of this diploma thesis.

---

[2]mass is just a form of energy (see Sec. 2.1.2 Equ. 2.2)

[3]measurements of the anomalous magnetic moment of e.g. muons

1. Introduction

2. The Standard Model
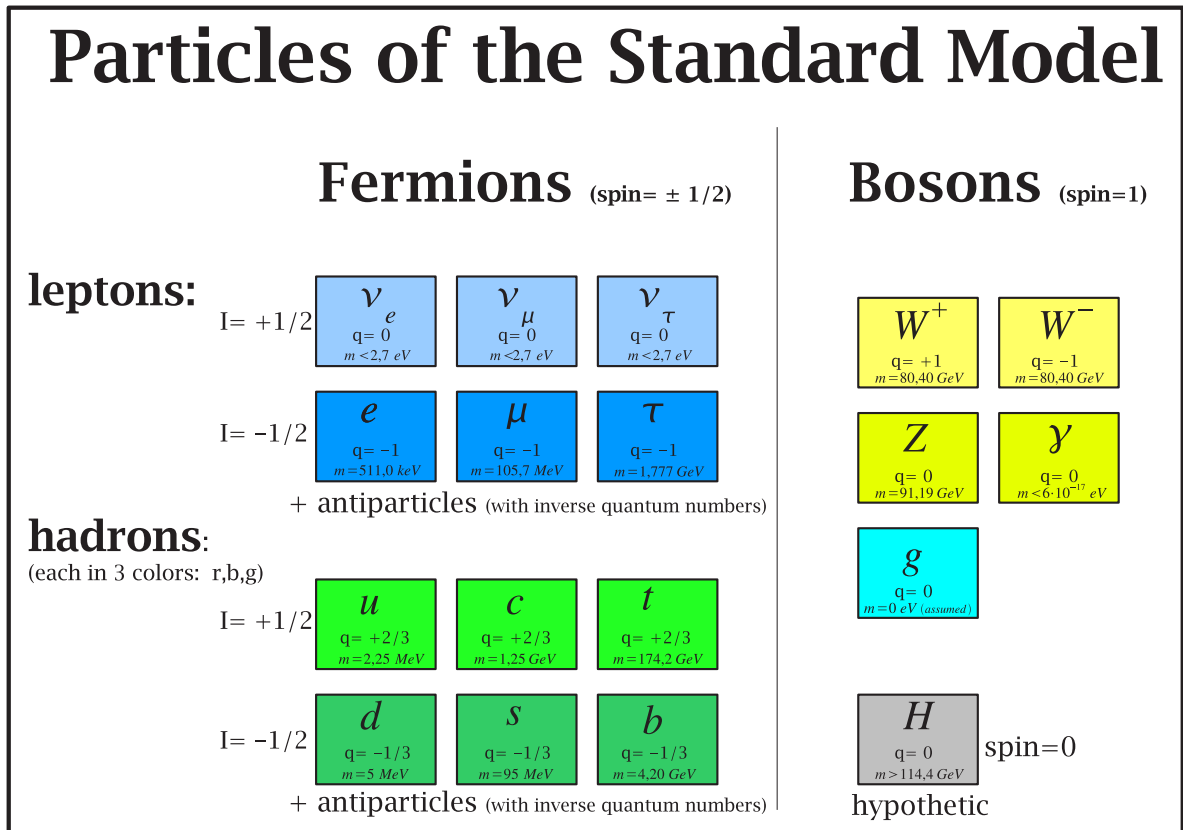
Figure 2.1.: *The particles of the Standard Model and their mass m, electrical charge q and weak isospin I. There are three columns (called families) of fermions with identical parameters except their masses. Particle data from [PDG06].*

The Standard Model is the current theory of particle physics describing the elementary particles and (most of) their interactions: the electroweak interaction (Sec. 2.4) and the strong interaction (Sec. 2.6). Its foundations are symmetry principles (Sec. 2.1.1), special relativity (Sec. 2.1.2), relativistic quantum mechanics (Sec. 2.1.3 and Sec. 2.1.4, or more precisely: quantum field theory), and the gauge principle (Sec. 2.2). Its mathematical description is in the form of gauge groups (Sec. 2.3). The particles of the Standard Model are shown in Fig. 2.1.

2.1. Foundation of the Standard Model

2.1.1. Symmetries

<center>*Physicists love symmetries.*</center>

Why do physicists love symmetries? Well, there is no relationship with aesthetics as in time of baroque for example. Rather with sympathy for simpleness. But what is a symmetry at all?

> *A thing is symmetrical if there is something you can do to it so that after you have finished doing it it looks the same as before* [Fey87].

A symmetry describes the invariance of entities against changes. If objects do not change under a certain operation, they are called invariant against this transformation.
A symmetry is described mathematically by a symmetry transformation (i.e. a continuous coordinate transformation like a displacement, but also a discrete transformation like mirroring). A symmetry of a basic theory is given if the physical laws describing the system do not change under a symmetry transformation [Hal84]. For examples see Tab. 2.1.

symmetry	transformation	conservation quantity
homogeneity of time	displacement in time	energy
homogeneity of space	displacement in space	momentum
isotropy of space	rotation in space	angular momentum
phase invariance	phase of charge wave function	electric charge

<center>**Table 2.1.:** *Example of symmetries and corresponding conserved quantities.*</center>

A simple example is as follows: The result of an experiment is independent of the time when it has been performed. From this follows the conservation of energy.

2.1.2. Lorentz Transformations

Lorentz transformations are transformations between inertial systems corresponding to special relativity. In special relativity time and space depend on the relative velocity between two inertial systems. Its foundation are two postulates by Albert Einstein (1878-1955) (and some work before by Henri Poincaré (1854-1912)):

1. In all inertial reference frames physical laws are identical.

2. There is a maximum speed c which is identical in all inertial systems.

The consequences of these postulates are the Lorentz transformation between two inertial reference frames moving to each other with the velocity v and the relativistic energy theorem:

Lorenz transformations for transformation in z-direction [Schm95]

$$\begin{pmatrix} t' \\ x' \\ y' \\ z' \end{pmatrix} = \begin{pmatrix} \gamma(t - \frac{\beta}{c}z) & 0 & 0 & 0 \\ 0 & x & 0 & 0 \\ 0 & 0 & y & 0 \\ 0 & 0 & 0 & \gamma(z - c\beta t) \end{pmatrix} \begin{pmatrix} t' \\ x' \\ y' \\ z' \end{pmatrix} \tag{2.1}$$

$$\beta = \frac{v}{c}, \qquad \gamma = \frac{1}{\sqrt{1 - \frac{v^2}{c^2}}}$$

<u>relativistic energy theorem</u>

$$E^2 = c^2 \vec{p}^2 + c^4 m^2 \tag{2.2}$$

2.1.3. Relativistic Quantum Mechanics

Schrödinger's equation cannot describe relativistic particles, since it is asymmetric in space and time coordinates and it does not fulfill the relativistic energy theorem (2.2).

Substituting time and space coordinates of the relativistic energy theorem (2.2) by operators leads to the *Klein-Gordon equation*[1] for a particle of mass m:

$$\left[\frac{1}{c^2} \cdot \frac{\partial^2}{\partial t^2} - \nabla^2 + \left(\frac{mc}{\hbar} \right)^2 \right] \phi = 0. \tag{2.3}$$

This equation only describes scalar particles.

2.1.4. The Dirac Equation

Paul Dirac (1902-1984) developed a basic approach for a relativistic wave equation:

$$i\hbar \frac{\partial \psi}{\partial t} = H\psi = -i\hbar \left(\alpha_1 \frac{\partial \psi}{\partial x_1} + \alpha_2 \frac{\partial \psi}{\partial x_2} + \alpha_3 \frac{\partial \psi}{\partial x_3} \right) + \beta mc^2 \psi \tag{2.4}$$

with free parameters x_1, x_2, x_3, β .

By iteration of this equation one gets:

$$\frac{\partial^2 \psi}{\partial t^2} = c^2 \sum_{j=1}^{3} \alpha_j^2 \frac{\partial^2 \psi}{\partial x_j^2} - \left(\frac{mc^2}{\hbar} \right)^2 \beta^2 \psi + c^2 \sum_{j \neq k} \frac{1}{2} (\alpha_j \alpha_k + \alpha_k \alpha_j) \frac{\partial^2 \psi}{\partial x_j \partial x_k}$$

$$+ \frac{imc^3}{\hbar} \sum_{j=1}^{3} (\alpha_j \beta + \beta \alpha_j) \frac{\partial \psi}{\partial x_j}. \tag{2.5}$$

For

$$\alpha_1^2 = \alpha_2^2 = \alpha_3^2 = \beta^2, \qquad \alpha_j \alpha_k + \alpha_k \alpha_j = 0 \text{ for } j \neq k, \qquad \alpha_j \beta + \beta \alpha_j = 0 \tag{2.6}$$

this results in the relativistic energy theorem using operators.

The α_i and β can not be scalar quantities, but must be matrices, since they have to fulfill the following conditions:

1. The coefficients α_i of the Hamilton operator should also be self-adjoint.

2. $\alpha_i = \beta^2 = \underline{\underline{1}}^2 \Rightarrow$ eigenvalues: ± 1

3. $trace(\alpha_j) = -trace(\alpha_j) \Rightarrow$ dimension of matrices must be even and greater than 2.

---

[1] Also called *Klein-Gordon-Schrödinger equation* because Schrödinger derived this equation before Klein and Gordon, but he did not publish it.

[2] a matrix

Using the γ-*matrices* (or Gell-Mann matrices)

$$\gamma^0 = \beta, \ \gamma^1 = \beta\alpha_1, \ \gamma^2 = \beta\alpha_2, \gamma^3 = \beta\alpha_3, \tag{2.7}$$

the Dirac equation (2.4) can be written as[3] :

$$(\mathbf{i}\hbar\gamma^\mu\partial_\mu - \mathbf{mc^2})\psi(\mathbf{x}) = \mathbf{0}^4. \tag{2.8}$$

2.2. The Gauge Principle

A transformation f of a scalar potential ϕ and a vector potential A, which does not change the corresponding field, is called *gauge transformation* [Kul06]:

$$A' = A + \nabla f, \qquad \phi' = \phi - const \cdot \frac{\partial f}{\partial t} \tag{2.9}$$

There are two types of gauge transformations:

global and *local gauge transformations.*

A global gauge transformation ϕ does not depend on space, thus e.g. the Schrödinger equation is invariant under a global phase transformation $e^{i\phi}$.
On the other hand a local gauge transformation $\phi(x_i, t)$ is depending on space x_i and time. For example the. Schrödinger equation is not invariant under a local gauge transformation [Schm95].

2.3. Gauge Groups

At the beginning of this section (Sec. 2.2) one has seen a basic concept of particle physics. The Standard Model is based on the following formalism:

- Chose a gauge group[5]: U(1), SU(2) and SU(3).

- Postulate the principle of local gauge invariance.

- Include the behavior of the theory under parity and charge transformations.

This way all interactions of the Standard Model can be derived, because the combination of U(1), SU(2) and SU(3) is the simplest combination which describes all observed particles and interactions [Reb04].
For a gauge group G a unitary gauge transformation U of the field $\psi(x)$ can be written as

$$\psi(x) \ \rightarrow \ \psi'(x) = U\psi(x) \qquad \text{here } x = x(t, \vec{x}). \tag{2.10}$$

Gauge transformations are generated by *generators* which have the dimension of the group.
All this will be described by the example of the electromagnetic interaction [Schm95]:
The gauge group $U(1)$ with a generator q is chosen. By applying a phase transformation

$$\psi'(x) = \exp\left(iq\xi(x)\right)\psi(x) \tag{2.11}$$

---

[3]as it is written down on P. Dirac's tombstone (with $c = 1$)
[5]Mathematically a gauge group is the ensemble of gauge transformations.

with the free Dirac equation[6]

$$(i\gamma^\mu \partial_\mu - m)\psi(x) = 0 \tag{2.12}$$

follows

$$(i\gamma^\mu \partial_\mu - m)\,\psi'(x) = -q\gamma^\mu \left(\partial_\mu \xi(x)\right)\psi'(x). \tag{2.13}$$

With the definition $A'_\mu = -\partial_\mu \xi(x)$ one gets:

$$(i\gamma^\mu \partial_\mu - m)\,\psi'(x) = q\gamma^\mu A'_\mu \psi'(x). \tag{2.14}$$

Now the new phase transformed wave function fulfills the Dirac equation with an electromagnetic field A'_μ.

If one postulates the existence of an electromagnetic field A_μ and inserts a covariant derivative D_μ with

$$D_\mu = \partial_\mu + iqA_\mu \tag{2.15}$$

into the Dirac equation, the Dirac equation remains invariant under a local phase transformation U.

In summary: If local phase invariance of the Dirac equation is postulated and the gauge group $U(1)$ is chosen, the electromagnetic field with its corresponding properties follows naturally.

2.4. The Electroweak Interaction

The electroweak interaction is the unification of the electromagnetic and the weak interaction. Choosing the combination of gauge groups $U(1) \times SU(2)$ with the principle of local gauge invariance, and the experimentally confirmed parity violation, the interaction in the form of the Lagrangian, divided in a left (L) and a right R part, follows [Hal84]:

$$
\mathcal{L} \;=\; -\frac{1}{4}W_{\mu\nu}\cdot W^{\mu\nu} - \frac{1}{4}B_{\mu\nu}\cdot B\mu\nu
\quad
\begin{cases}
W^\pm,\; Z,\; \gamma \text{ kinetic terms} \\
\text{and} \\
\text{self-interactions}
\end{cases}
$$

$$
\begin{aligned}
&+\overline{L}\gamma^\mu \left(i\partial_\mu - g\tfrac{1}{2}\tau\cdot W_\mu - g'\tfrac{Y}{2}B_\mu\right)L \\
&+\overline{R}\gamma^\mu \left(i\partial_\mu - g'\tfrac{Y}{2}B_\mu\right)R
\end{aligned}
\quad
\begin{cases}
\text{lepton and quark} \\
\text{kinetic energies} \\
\text{and their} \\
\text{interactions with} \\
W^\pm,\; Z,\; \gamma
\end{cases}
$$

$$
+\; \left|\left(i\partial_\mu - g\tfrac{1}{2}\tau\cdot W_\mu - g'\tfrac{Y}{2}B_\mu\right)\phi\right|^2
\quad
\begin{cases}
W^\pm,\; Z,\; \gamma \\
\text{coupling to Higgs potential } \phi
\end{cases}
\tag{2.16}
$$

with the corresponding covariant derivative [Schm95]:

$$D^\mu = \partial^\mu + i\frac{g}{\sqrt{2}}\left(\tau_+ W^{(-)\mu} + \tau_- W^{(+)\mu}\right) + i\frac{g}{2}\tau_3 W_3^\mu - i\frac{g'}{2}B^\mu. \tag{2.17}$$

g, g': parameters of the electro weak interaction
$W^\pm$, B, γ: bosons
Y, τ: generators of the group: weak hypercharge, weak isospin

---

[6]For the remaining part of this chapter $c = \hbar = \mu_0 = 1$ is set.

2.5. The Higgs Boson

The electroweak interaction is carried by photons and by the massive gauge bosons $W^\pm$ and Z^0 discovered by experiments, but with massive gauge bosons there is no local gauge invariance. With an additional scalar particle, gauge bosons and fermions acquire masses by the interaction with this field. The particle creating this gauge field is called the *Higgs* boson. It is the last to be discovered particle of the Standard Model.

Direct searches at LEP[7] have excluded a Higgs boson with mass below 114,4 GeV/c^2 [PDG06, PTB04].

2.6. Quantum Chromo Dynamics (QCD)

Similar to the electroweak interaction, the strong interaction between quarks and gluons can be described by a gauge group, in this case $SU(3)$. The corresponding theory is called **Q**uantum **C**hromo **D**ynamics.

The wave function Ψ of a strongly interacting particle can be split into two spinors for the time and space depending part $\psi(t,\ \vec{x})$ and the color part χ_{color}

$$\Psi = \psi(t,\ \vec{x}) \cdot \chi_{color}. \tag{2.18}$$

Color is an additive quantum number of the quarks and the gluons. There are three colors: red, green and blue with the color spinors

$$\chi_{red} = \begin{pmatrix} 1 \\ 0 \\ 0 \end{pmatrix}, \qquad \chi_{green} = \begin{pmatrix} 0 \\ 1 \\ 0 \end{pmatrix}, \qquad \chi_{blue} = \begin{pmatrix} 0 \\ 0 \\ 1 \end{pmatrix}. \tag{2.19}$$

A local SU(3)-gauge transformation is given by

$$\Psi' = \exp\left(i\frac{\alpha_S}{2}\lambda_j \beta_j(x) \right) \Psi, \tag{2.20}$$

with the strong coupling constant α_S and eight coefficients β_i of the transformation.

Using the corresponding covariant derivation D the Lagrangian $\mathcal{L}$ for one quark can be written as

$$\mathcal{L} = \overline{\Psi}\left(i\hbar\gamma_\mu D^\mu - m \right)\Psi - \frac{1}{4}F_{i,\ \mu\nu}F_j^{\mu\nu}. \tag{2.21}$$

$F_j^{\mu\nu}$ is the field tensor with

$$F_j^{\mu\nu} = \partial^\mu G_j^\nu - \partial^\nu G_j^\mu - \alpha_S f_{jkl} G_k^\mu G_l^\nu. \tag{2.22}$$

f_{jkl} = structure constants.

The G_j^μ are the eight gluon fields. The gluons are the gauge bosons of the strong interaction. The gluon interacts with itself because the gluon has also color. The self-interaction leads to a running coupling constant α_S, i.e. the value of the coupling constant depends on the relevant energy scale.

For high energies α_S decreases with $\alpha_S(M_{Z^0}) \simeq 0,11$. At low energies α_S is large (< 1).

The form of the QCD-potential $V(r)$ is

$$V \sim \frac{\alpha_S}{r} + k\,r, \tag{2.23}$$

---

[7]**L**arge **E**lectron positron **C**ollider at CERN

$k \approx 0{,}9\,\mathrm{GeV/fm}$ [Schm95].

The second term in Equ. 2.23 leads to the so called *confinement*: Quarks cannot be observed as free particles. If there is enough energy one will not separate two quarks. The energy will be converted to create a quark-antiquark pair.

2.7. Open Questions - Physics beyond the Standard Model

The SM is a very successful theory based on the particles shown in Fig. 2.1.

Until now there is no experiment with results that are in contradiction with the predictions of the SM, if neutrino oscillations[8] are treated as a minimal extension of the standard model.

But there are a lot of hints to physics beyond the SM. The two most significant ones come from astrophysics [Scha04]:

The SM does not explain the *Dark Matter* (DM) and the *Dark Energy* (DE), which are necessary to describe the evolution of the universe and the movements of stars and galaxies at large scales.

A theory beyond the SM should also explain (some of) the $17 + 1$ independent constants of the SM [Berg02]:

- Nine masses of fermions

- the mass of the Z-boson

- Four parameters of the mixing matrix for quarks

- Three coupling parameters: α, Θ_W, α_S

- mass of the hypothetical Higgs boson

Additionally the following parameters are needed:

- the gravitational constant G

- 3 masses of neutrinos (because of neutrino oscillations)

- 4 parameters of the mixing matrix for leptons (because of neutrino oscillations)

2.7.1. Supersymmetry

The most popular extension of the SM at the moment is supersymmetry. This theory predicts a symmetry between spin-1 particles (bosons) and spin 1/2 particles (fermions).

Supersymmetry could give answers to some questions of the SM like dark matter, unification of couplings and some problems with the Higgs formalism at high energies.

2.7.2. Substructure

In this theory leptons and quarks are not fundamental, they have a substructure. Their mass can be explained as *binding energy*. In this case there must be a new interaction between the new fundamental particles. The interpretation of quarks and leptons as composite particles could explain the observation of three generations.

---

[8]the transformation from a neutrino to a neutrino of another family

2.7.3. Strategies for Searches New Physics

According to Sec. 1.2 there are several ways to search for new physics. There are some high precision experiments (BaBar/Belle) which are measuring B-meson decays.
Also some astrophysical experiments which are searching in direct and indirect ways for DM particles could find new physics.

The LHC and within the CMS detector will be at the frontier of collider physics and thus will have a great chance to find new physics.

3. The CMS Detector

3.1. The CMS Environment at LHC

The last particle of the SM not yet discovered is the Higgs boson. The new collider ring **L**arge **H**adron **C**ollider is primarily designed to find or exclude the Higgs boson and to find physics behind the Standard Model. There is a great hope for finding new physics at the weak scale[1], and supersymmetry (Sec. 2.7.1) is the most favored theory. But also measurements of standard model parameters are planned, like the W-boson and top quark masses or B-physics[2] parameters.

For covering the whole mass range up to $1\,\text{TeV}/c^2$ for the Higgs boson and for producing enough statistics the collider reach center of mass energies up to $2 \cdot 7$ TeV and a design luminosity of $10^{38}\,\text{m}^{-2}\,\text{s}^{-1}(= 10^{34}\,\text{cm}^{-2}\text{s}^{-1})$. Two proton beams are accelerated in two pipes with a circumference of $27\,\text{km}$ and a magnetic field of more than $8\,\text{T}$ (Fig. 3.1) [PTD06].
To reach this high luminosity two proton beams have been chosen because antiprotons (instead of protons) cannot be produced so easily and cheaply in large quantities. The proton beams in two beam pipes consist of 2808 packages, called *bunches* each containing $1{,}15 \cdot 10^{11}$ protons. At four interaction points the beam pipes are crossed to produce collisions of protons. The time distance between two bunch crossings is $25\,\text{ns}$.
The ring consists of 1232 superconducting magnets which are cooled down to 1,9 K and can create a magnetic field of up to 8,4 T.

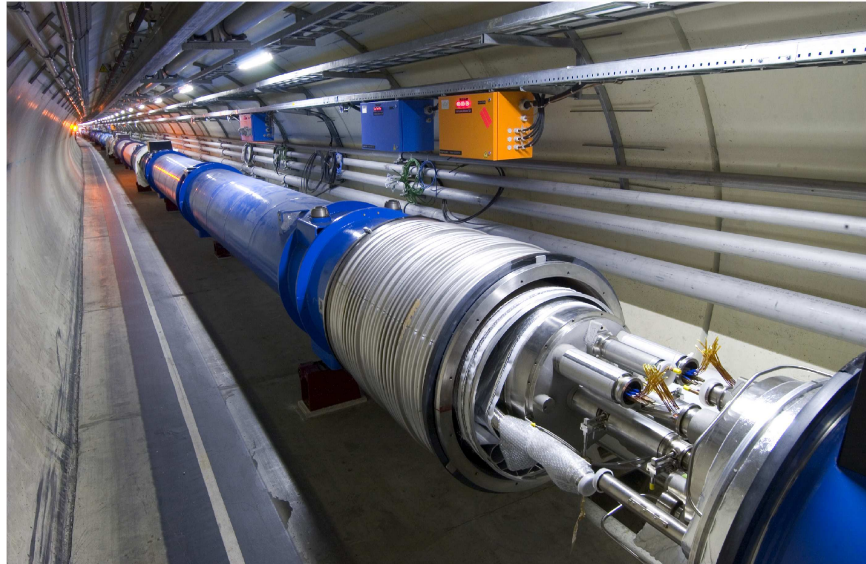**Figure 3.1.:** *The LHC tunnel with superconducting dipole magnets, which keep the two proton beams inside the beam pipes on track [CER07].*

---

[1] $246\,\text{GeV} = 1/\sqrt{G_F/\sqrt{2}}$
[2] physics with B-mesons

There are four large experiments (Fig. 3.2) at the LHC. Two general purpose detectors, CMS and ATLAS[3], and two specialized detectors, ALICE[4] and LHCb.

The two specialized experiments are designed to look into special physics issues. While LHCb is looking at B-physics, the purpose of ALICE is the analysis of heavy ion collisions for which the LHC will run with Pb ions instead of protons for a while.
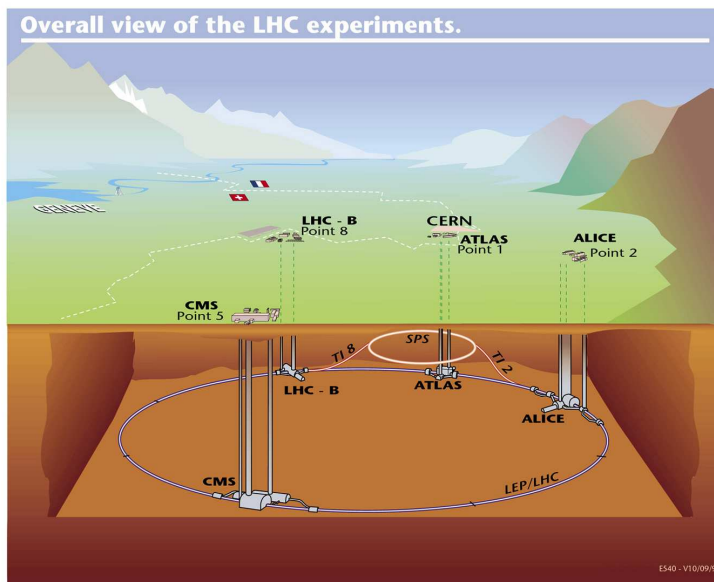

Figure 3.2.: *The LHC accelerator ring and the locations of the four experiments [CER07]*

ATLAS is a multi purpose detector like CMS. Its magnetic field is formed by toroids which allows a construction with less absorption in the outer part of the detector. In the inner region inside the calorimeters an additional solenoid magnet forming a magnetic field of 2 T is located. The strength of the ATLAS spectrometer is its outer muon detector with a design single cell resolution of 60 μm [Altas94].

3.2. Components of the CMS Detector

CMS is a classical beam collider experiment consisting of a series of concentric cylinders with increasing diameter around the interaction point.

The Compact Muon Solenoid contains a very large solenoid magnet with a diameter of 4,9 m. Tracker, electromagnetic calorimeter and hadronic calorimeter are situated inside the magnet coil, so that there is less absorbing material before the calorimeters. The strength of the CMS detector is its tracker (Sec. 3.2.2) in combination with the muon system (Sec. 3.2.6) and the very good electromagnetic calorimeter (Sec. 3.2.3). With the muon system it is easy to identify muons because the muon chambers are integrated in return yokes made of iron and so the flux of other particles remaining after the hadron calorimeter (Sec. 3.2.4) will be reduced significantly. As a classical 4π-experiment, that means nearly the whole surface around the interaction point

---

[3]**A T**oroidal **L**HC **A**paratu**S**
[4]**A L**arge **I**on **C**ollider **E**xperiment

is covered by detector components each specialized for some kind of particles (Fig. 3.4). The central region is called *barrel* region. To reach approximately the 4π-geometry at the front faces, called *endcaps*, there are additional detector parts.

CMS is constructed on the surface before being lowered into the cavern part by part so that parts of the detector could be tested with the higher flux of cosmic muons on the surface.
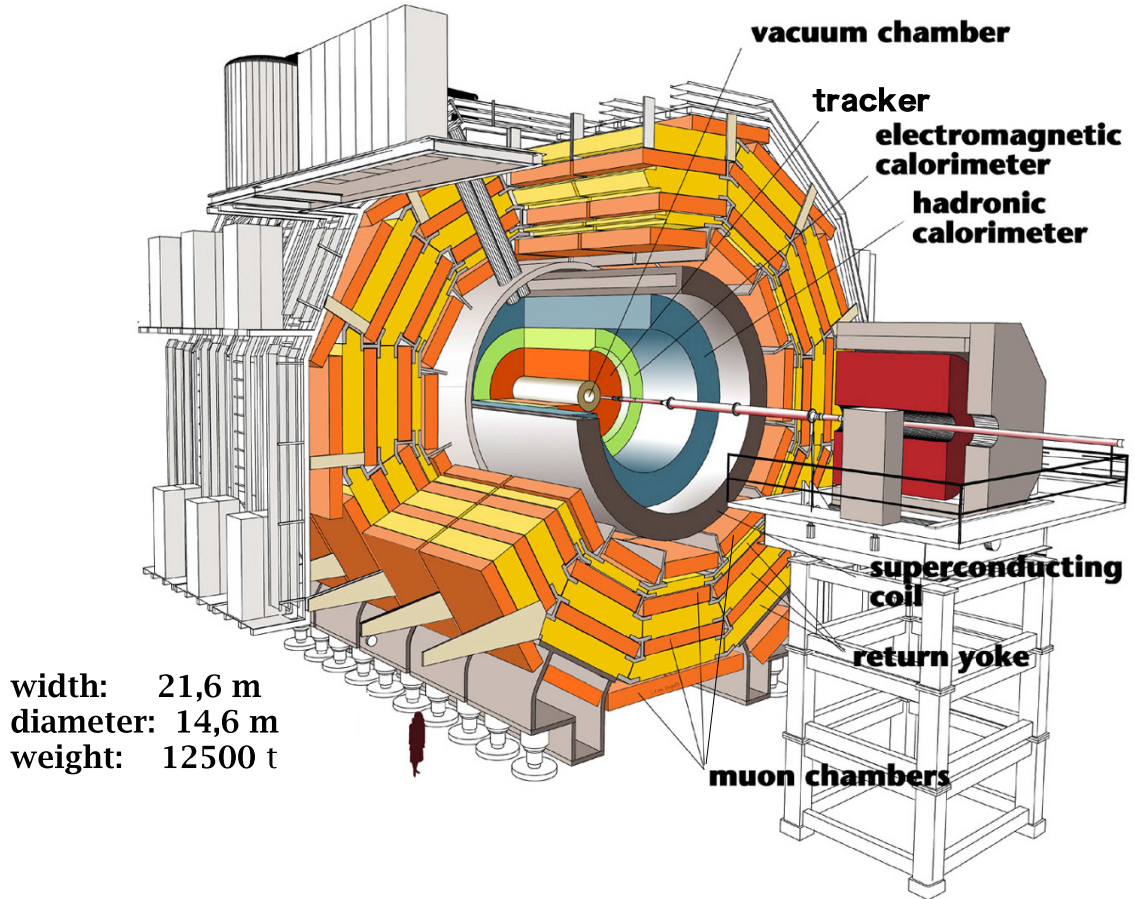
Figure 3.3.: *Sketch of the CMS-detector [CER07].*

3.2.1. The CMS Coordinate System

The center of the coordinate system is the interaction point in the center of the detector. The y-axis points vertically upwards, the x-axis towards the center of the LHC and the z-axis along the beam pipe.

The azimuthal angle ϕ is measured with respect to the x-axis in the x-y-plane. The polar angle θ is measured with respect to the z-axis. The pseudorapidity η is defined as:

$$\eta = -\ln \tan \left(\frac{\theta}{2} \right). \tag{3.1}$$

3.2.2. The Silicon Tracker

The first part of the detector seen from the beam pipe is the tracker. The tracking volume is given by a cylinder of length $5,8$ m and diameter $2,6$ m. It consists of 66 Million pixels and 9,6 Million silicon strips. There are three main parts [PTD06]:

- Pixel detector: At the closest distance to the interaction point, given by the diameter of the beam pipe, a detector part with highest resolution is needed because of the small lever arm and because the track of different particles are very close to each other so that a small granularity is needed. Therefore in CMS a semiconductor detector based on small pixels is used. The total active surface is $1\,m^2$.
  It is built of three layers at 44 mm, 73 mm and 102 mm from the vertex and two endcaps disks at each side at $|z| = 345$ mm and $|z| = 465$ mm with inner diameters of 60 mm and 150 mm based on pixels with a size of $100\,\mu m \times 150\,\mu m$. By using pixels two coordinates can be measured simultaneously with a precision of about $10\,\mu m$ for the $r-\phi$-measurement and about $20\,\mu m$ for the z-measurement.

- Tracker Inner Barrel (TIB): The rest of the tracker (inner and outer tracker) is built of silicon strips,i.e. the sensitive region of the silicon is made in form of strips. By placing modules[5] in an angle to each other, two coordinates can be measured with high precision. The TIB contains four layers reaching to $|z| < 650$ mm with a strip pitch of $80\,\mu m$ to $120\,\mu m$. The first two layers are *stereo modules*, i.e. there are actually two modules glued together with an angle of 100 mrad. The single point resolution is $23\,\mu m$ to $34\,\mu m$ in $r-\phi$-direction and $230\,\mu m$ in z-direction.

- Tracker Outer Barrel (TOB): The TOB consists of six layers covering the region $|z| < 1,1$ m built of modules with strip pitches of $120\,\mu m$ to $180\,\mu m$. Again the first two layers are stereo modules. The single point resolution is $35\,\mu m$ to $52\,\mu m$ in $r-\phi$-direction and $530\,\mu m$ in z-direction.

- Tracker EndCap (TEC): It consists of 9 disks at each side covering the region $1,2$ m $< |z| < 2,8$ m. The angular range up to $|\eta| < 2,5$ is covered.

The total active surface of TIB, TOB and EC is $200\,m^2$. Using the whole tracker a resolution for 100 GeV muons of $10\,\mu m$ with $|\eta| < 2$ in $r-\phi$-direction and $20\,\mu m$ to $40\,\mu m$ with $|\eta| < 2$ in z-direction is reached (Fig. 1.11 of [PTD06]). The resolution of the transverse momentum p_T for muons is shown in Fig. 3.6.

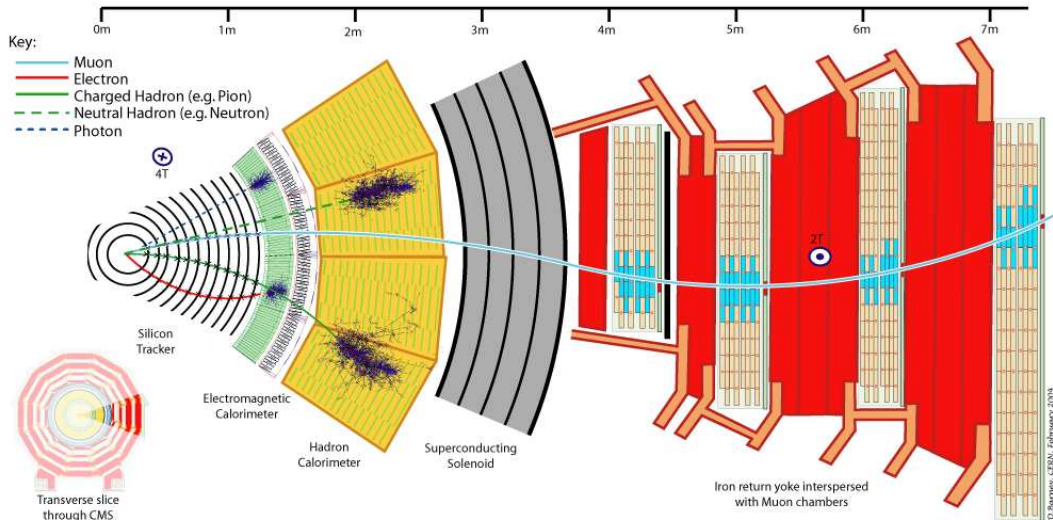[5]the basic unit of the silicon detector

Figure 3.4.: *Detection of different particle in the CMS sub detectors [CER07].*

3.2.3. The Electromagnetic Calorimeter

In the CMS detector the electromagnetic (ECAL) and the hadronic calorimeter (HCAL) are inside the magnet to minimize the absorbing material the particles have to pass before reaching the calorimeters. Thus, the energy of the particles can be measured more precisely.

In an electromagnetic calorimeter particles are stopped to measure their energy by the creation of electromagnetic radiation. In an electromagnetic calorimeter electrons, positrons and photons are stopped.

The electromagnetic calorimeter of CMS is made of inorganic, scintillating crystals of $PbWO_4$ which consists of around 70 % metal, but is transparent. $PbWO_4$ has got a *radiation length*[6] of 8,9 mm and a *Moliere radius R_M*[7] of 22 mm. This allows a compact ECAL which can be placed inside the magnet coil. Given the fact that $PbWO_4$ is an anorganic scintillator, it has a short decay time (= 10 ns, 80 % of the light is emitted in 25 ns).

In the barrel there are 61200 crystal modules with a face cross section of $(22 \times 22)\,\text{mm}^2$ and a length of 230 mm $(25,8\,X_0)$. The inner radius of the ECAL in r-direction is 1,29 m covering up to $\eta < 1,479$.

In each endcap ECAL there are 7324 crystals with a face cross section of $(28,6 \times 28,6)\,\text{mm}^2$ and a length of 220 mm corresponding to a radiation length of 24,7 X_0. The endcaps cover a range $|\eta| < 3,0$.

Due to the low output of light in $PbWO_4$ (photons / absorbed energy = 30 /MeV) photo detectors with a high efficiency have to be used. In addition the photo detectors have to be able to work in the high magnetic field. Thus, avalanche photodiodes (APD) in the barrel region and vacuum phototriodes (VPTs) in the endcap are used because they are able to work in high magnetic fields and have a high photon detection efficiency (up to 70 %) for the corresponding scintillation light. Both, the APDs and the crystals, need a constant temperature for operating at constant efficiency and gain, thus the whole ECAL is temperature controlled with a precision of $< 1\,\text{K}$.

The ECAL is read out by Analog Digital Converters (ADCs) with a frequency of 40 MHz, the

---

[6] the characteristic amount of matter traversed for the generation of bremsstrahlung and pair production

[7] $R_M = \frac{21\,\text{MeV}}{E_c} \cdot X_0$, defined as the radius of a cylinder, where 90 % of the shower is located [PDG06]

17

pulse spectra samples are weighted and summed to get the amplitudes of the pulses. The measured noise per channel is < 40 MeV.

The energy resolution $\delta(E)/E$ can be parameterized by

$$\frac{\delta(E)}{E} = \frac{S}{\sqrt{E/\text{GeV}}} \oplus \frac{N}{E/\text{GeV}} \oplus C, \tag{3.2}$$

with $a \oplus b = \sqrt{a^2 + b^2}$

S: statistical term

N: noise term

C: constant term

The measured energy resolution $\delta(E)/E$ is 1,4 % at 10 GeV and 0,4 % at 250 GeV.

3.2.4. The Hadronic Calorimeter

In the hadronic calorimeter (HCAL) the strong interacting particles are stopped. By interacting with nucleons of the (passive) absorber material charged (and neutral) particles are produced. Those particles can generate light in scintillators.

Brass is used as absorber and the scintillators are plastic scintillator plates with a thickness of 3,7 mm. Brass has a short interaction length and is non magnetic. The read out is done by embedded wave length shifting fibers (WLS) in the scintillator tiles. The light is guided by clear fibers with high attenuation length to the outside of the HCAL where it is processes by multi channel hybrid photodiodes (HPDs).

The resolution for the missing transverse energy is $\sigma(E_T^{miss}) = 1,0\sqrt{\sum E_T}$.

There are four parts of the HCAL:

- Hadron Barrel (HB): It consists of 15 plates of brass with a thickness of 50 mm and covers the region up to $\eta = 1,4$. The segments have a granularity of $\Delta\eta \times \Delta\phi = 0,087 \times 0,087$.

- Hadron Outer (HO): It is physically located in the barrel muon system (Sec. 3.3, Fig. 3.7) at the outside of the vacuum tank of the magnet coil. Thus, the magnet acts as an extra layer of absorber leading to a total thickness of ten interaction lengths[8]. The tiles and scintillators with a thickness of 10 mm are grouped in 30° sectors. The HO covers the region up to $\eta < 1,26$.

- Hadron Endcap (HE): It covers the region at $1,3 < \eta < 3,0$.

- Hadron Forward (HF): It is a complement of the HE (see Fig. 3.5) for $3,0 < \eta < 5,0$. Although the front face is located 11,2 m from the interaction point, the high radiation level in this η-region is very high. Thus, detectors with very high radiation hardness have to be used here. Quartz fibers instead of "normal" scintillators with a diameter of 0,6 mm inside an absorber of steel of 1,65 m thickness are used. Cerenkov light is created inside the quartz fibers and detected by photomultipliers.

3.2.5. The Magnet

To generate a high magnetic field of 4 T for a high momentum resolution and to have enough space inside for calorimeters with sufficient radiation/interaction lengths a super conducting

---

[8]corresponding value of the radiation length for hadronic calorimeters

magnet with an inner diameter of 4,9 m was constructed (see Tab. 3.2.5). It is the largest superconducting solenoid magnet of the world.

magnetic field	4 T
inner bore	5,9 m
length	12,9 m
number of layers	4
number of turns	2168
current	19,5 kA
stored energy	2,7 GJ
hope stress	6,46 MPa
conductor cross section	$(64 \times 22)\,\text{mm}^2$

Table 3.1.: *Data of the CMS-solenoid [PTD06].*

3.2.6. The Muon System

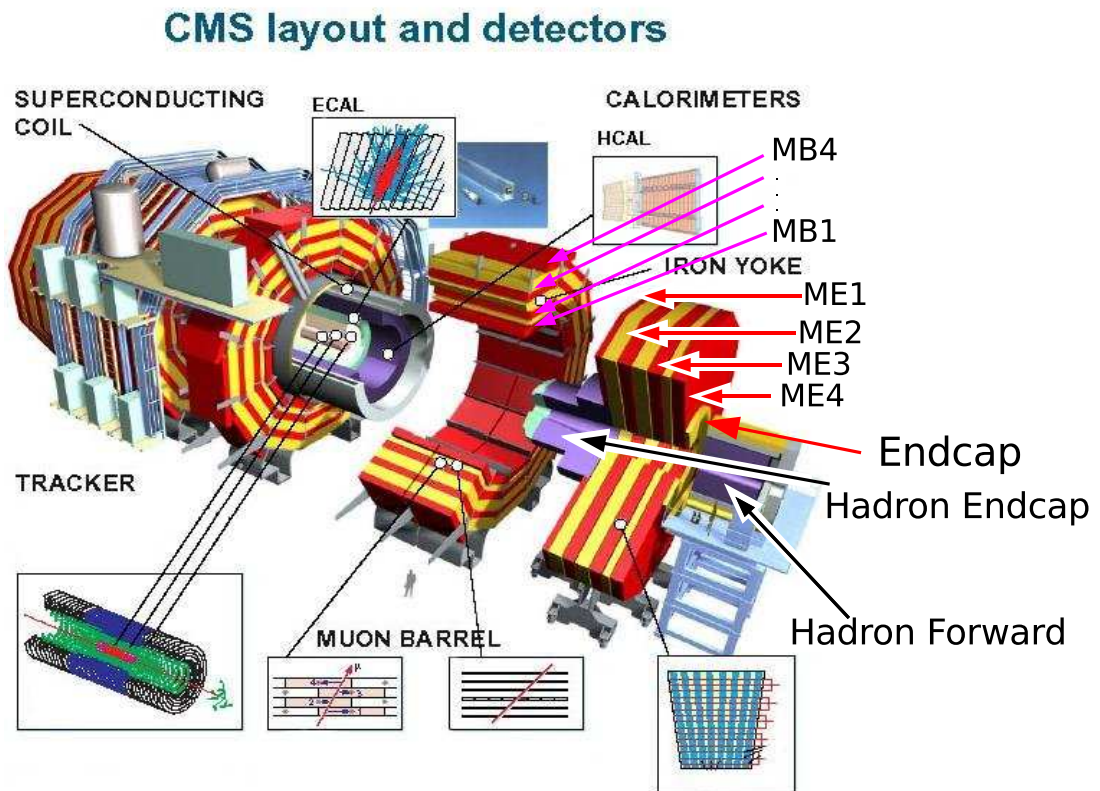**Figure 3.5.:** *The CMS detector and the structure of its muon system [CER07].*

The CMS muon system consists of two main parts: the barrel muon system for $|\eta| < 1,2$ and the endcap muon system for $1,2 < |\eta| < 2,4$. The whole muon system has a surface of $2500\,\text{m}^2$ and contains nearly one million readout channels.

In the two Muon Endcap (ME) regions with higher magnetic field and higher rates than in the

19

barrel region, 468 cathode strip chambers (CSCs), oriented vertically to the beam pipe, are used. There are four stations called ME1, ME2, ME3 and ME4 (see Fig. 3.5).

Each CSC consists of six gas gaps, each having a plane of radial cathode strips and a plane of anode wires running almost perpendicularly to the strips. Charge separated by a traversing particle is amplified near an anode wire. The avalanche developed on a wire induces a charge distribution of well known shape on the cathode plane. By measuring the center of gravity of the induced charge on the cathode strips, precise position measurements can be made. Each CSC measures up to six space coordinates (r, ϕ, z). The spatial resolution of a single CSC chamber is about $200\,\mu m$ and the angular resolution in ϕ is in the order of $10\,mrad$.

In both, the endcap muon system and the barrel muon system (Sec. 3.3), additional special gas detectors, so called resistive plate chambers (RPCs, Sec. 3.3.1), for triggering are mounted.
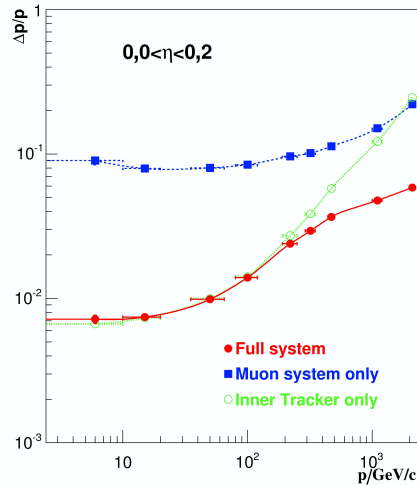

Figure 3.6.: *The p_T-resolution in CMS, depending on the muon momentum [PTD06].*

3.3. The Barrel Muon System

The magnet is enclosed by *return yokes* made of iron which contain the magnetic field. The return yokes are separated into five wheels called **Y**oke **B**arrels: YB-2, YB-1, YB0, YB+1, YB+2 (see Sec. 3.5). Each wheel consists of three rings of iron.

Within (and on) this structure the barrel muon drift tube chambers (DTs) are placed. Their purpose is to determine the position and the momentum of high energy muons. Additional resistive plates chambers (RPCs, Sec. 3.3.1) for trigger purpose are placed between the barrel muon chambers.

Each of the five wheels can be divided into twelve sectors of DT chambers covering approximately $30°$ in ϕ. For each sector there are four so called stations of DT-chambers with increasing distance from the beam pipe of DT-chambers (see Fig. 3.7): MB1, MB2, MB3 and MB4 (MB = Muon Barrel, see 3.7). The MB1 to MB4 are located at $4,0\,m$, $4,9\,m$, $5,9\,m$ and $7,0\,m$ from the beam axis. All DT chambers are located inside the corresponding return yoke part. In each sector there is one DT chamber per station.
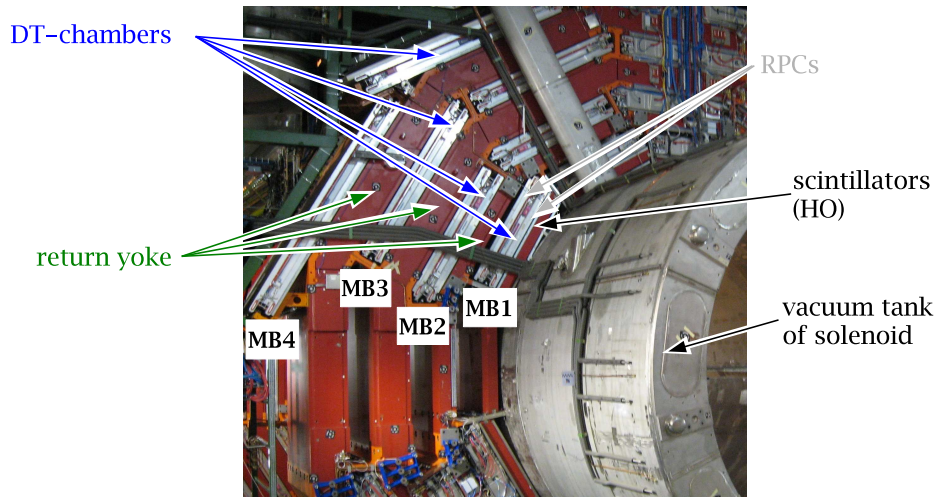
Figure 3.7.: *DT chambers and RPCs embedded in the iron return yoke of YB0.*

The DT chambers in MB1 and MB2 are surrounded by two RPC chambers. The DT chambers in MB3 and MB4 have one RPC chamber at the innermost side. Two MB4 stations in the horizontal sectors are segmented into two separate DT chambers. Thus, there are 50 DT chambers per wheel. Each station except MB4 contains twelve DT layers.

A muon vector in space can be measured with a ϕ resolution better than $100\,\mu$m per station in position and approximately $1\,$mrad in angle.

The MB4 DT-chambers have only 2 $r - \phi$-superlayers (see Fig. 3.8 and Sec. 3.3.2). A high$-p_T$ muon can cross up to 6 RPCs and 4 DT chambers with 44 hits in DT chambers from which a muon track can be built.

Figure 3.8.: *The structure of a DT chamber [Sowa06].*

3.3.1. The Resistive Plate Chambers

RPCs have a double gap of $2\,$mm with a gas and operate in avalanche mode. The inner bakelites (=material of inner surface) are coated with linseed oil to reduce the noise. If a charged particle traverses the RPC, near the point of ionization of atoms limited discharges are generated that can be measured. The advantage of RPCs is their good time resolution of better than $2\,$ns [MUO97]. The RPC can identify unambiguously the correct bunch crossing for a given muon and give the trigger for the DT chambers of the corresponding station.

3.3.2. The Drift Tube Chambers (DTs)

The basic unit of a drift tube chamber is a *drift cell* (Fig. 3.9) with a width of 42 mm and a height of 13 mm. An electric field is generated by two cathodes at the end plates and the anode wire in the middle of the cell. The E-field is formed by field shaping strips at the top and bottom side. Thus, a drift field of around 100 V/mm to 250 V/mm is generated. A traversing particle ionizes the gas. The created free electrons at the shortest distance ("fastest distance") to the anode wire will reach it first. Near the anode drifting electrons cause an avalanche in the gas and a electrical signal is created. By measuring the time difference to an external trigger, e.g. by the RPCs, the distance of the track to the anode wire can be determined. By combination of many cells the track of a particle can be reconstructed. A measured point of a particle track in one cell is called *hit*. The single hit resolution is around 200 μm [PTD06]. The total number of cells in the barrel DT chambers is 172000.

Four layers of drift cells are called a *superlayer*. In the MB 1 to MB 3 chambers there are two superlayers with the anode wire parallel to the beam line measuring the $r - \phi$-coordinate and the third superlayer is measuring the z-coordinate. Seen from the beam pipe, first there is a $r - \phi$-superlayer, than a z-superlayer (or called θ-superlayer) followed by a honeycomb structure made of aluminium and the second $r - \phi$-superlayer so that there is a lever arm of 280 mm inside a DT-chamber.
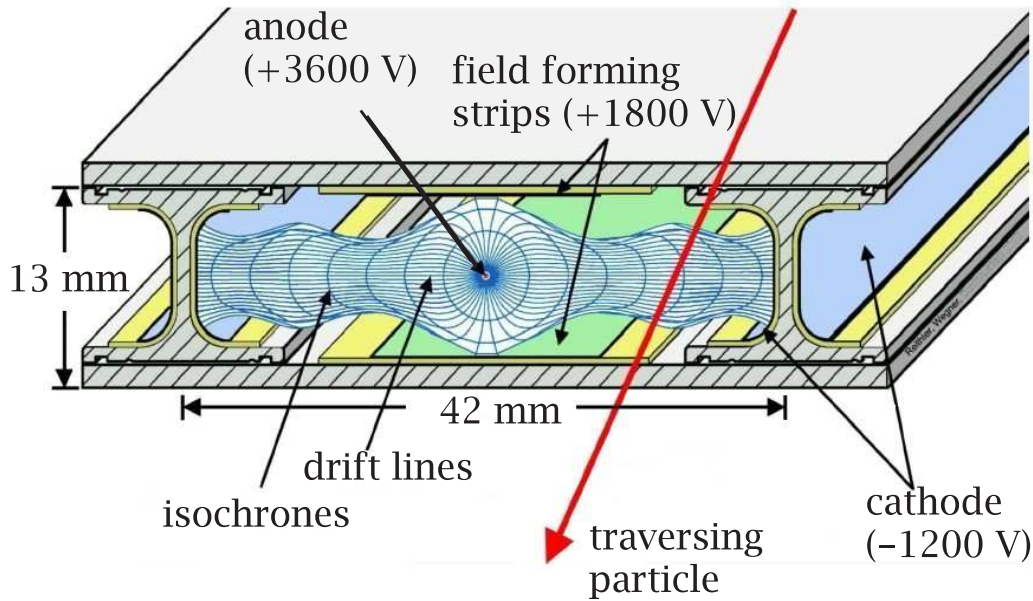
Figure 3.9.: *Sketch of a drift cell from a barrel muon chamber [Rei07].*

The readout electronic in form of a so called *Mini-Crate* is mounted on the chambers. There the discriminated signals from the anodes are digitized by *Time to Digital Converters* (TDC). At the inlet and the outlet of each DT there is a gas distributor (*manifold*) to and from the three superlayers containing two relative pressure sensors with different ranges (10 kPa and 50 kPa). In all barrel muon chambers a mixture of argon and carbon dioxide in a ratio of 85 % to 15 % is used, with a flux of 50 L/h corresponding to a few gas exchanges a day (volume of DT chamber $\approx 1\,\mathrm{m}^3$), so that there is always clean gas inside the chamber.

3.3.3. The Gas System

Figure 3.10.: *The gas system of the barrel muon DT chambers (Fig. 3.6.4 from [MUO97]).*

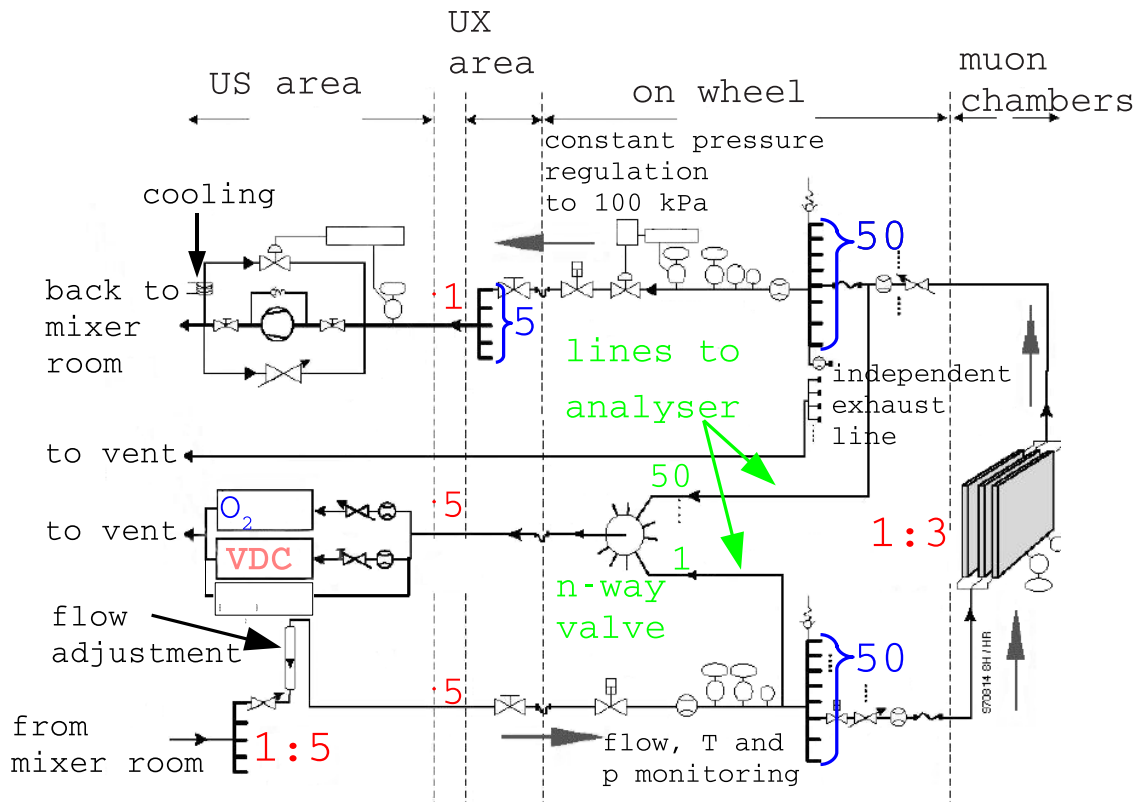The gas for the DT chambers is circulated in a closed circuit with some adding of fresh gas. On each wheel there is a distribution panel for the 50 supply and 50 exhaust lines which can regulate the absolute pressure in the gas system of the wheel. The maximum pressure differences should be 270 Pa caused by 15 m height difference at the wheels. A flexible section allows the wheel to be moved while the gas system is connected. There is only one in- and output line per wheel.

A sketch of the whole gas system is shown in Fig. 3.10. The mixer room located at the surface is the source of the gas. Here the gas is directed to the underground, to the USC[9] gas room. From here it is distributed to five lines to the wheel in UXC[10] including a flow control. From each line gas can be branched off to analyze it. The gas in the five lines from the wheel gets back to the USC gas room after a constant pressure regulation to 100 kPa. Here it is bundled to one line and water cooled before it goes back to the mixer room.

The gas monitoring:

There is one line from each wheel that can be connected to the outlet of each DT chamber. Using an n-way valve this gas or the gas branched off from the inlet to a wheel can be directed to the

---

[9]**U**derground **S**ervice **C**avern
[10]**U**derground e**X**perimental **C**avern

USC gas room. Here for each of the five lines there is in parallel an oxygen analyzer, a humidity analyzer and a drift velocity monitoring (**VDC**). The output of the analyzed gas goes to the vent.

The mixer room:

Here gas storage, mixer, purifiers and further analyzers are located.

The gas cleaning:

The most relevant impurities which may harm the detector are air, water vapor, halogens and silicates which can effect aging in the DT chambers. To reduce impurities in the gas, several mechanisms have been chosen to clean the gas. A micro sieve removes small particles like dust. A OxisorbTM[11] gets out oxygen and other gases except nitrogen. Thus, in case of contamination by air nitrogen will be concentrated and it is not possible (except by very expensive mass spectrometers) to measure the nitrogen concentration. Nitrogen will change the drift velocity significantly, even in small concentrations. Therefore, this change of the drift velocity has to be detected directly by the **VDCs**. And even if the exact gas mixture was known, it would not be possible to calculate the drift velocity with the same precision that the VDCs can measure it.

---

[11]by Nesser Griesheim GmbH

4. Drift Chambers

4.1. Passage of Charged Particles through Matter

When a charged particle passes through matter following interactions between the particle and the matter can occur:

- ionization
- bremsstrahlung
- nuclear interaction
- multiple scattering

For particles with energies below $10\,\mathrm{MeV}$ and material with smaller Z than lead only ionization and multiple scattering is important.

4.1.1. Energy Loss of Heavy Particles

The energy loss $\mathrm{d}E$ per path length $\mathrm{d}x$ for massive charged particles (all charged particles except the electron and positron) in matter is described by the formula of *Bethe and Bloch* [PDG06]:

$$\left(\frac{\mathrm{d}E}{\mathrm{d}x}\right)_{ion.} = -F \cdot \frac{Z}{A} \cdot \rho \cdot \frac{1}{\beta^2} \cdot \left(\ln\left(\beta^2\gamma^2\right) + C\right) \tag{4.1}$$

$A =$ atomic mass of the matter
$Z =$ atomic number of the matter
$\rho =$ density of the matter (in $\mathrm{kg/m^3}$)
$\beta = v/c =$ velocity of the particle
$\gamma = \frac{1}{\sqrt{1-\beta^2}} =$ relativistic Lorentz factor
$C = \ln\frac{2m_e c^2}{I_{eff}}$
$m_e =$ mass of electron (in eV/c^2)
$I_{eff} =$ effective ionization energy (in eV)
$F = \frac{4\pi N \alpha^2 \hbar^2}{m_e} = 30\,\mathrm{keV m^2\,kg^{-1}}$
$\alpha =$ electromagnetic coupling constant ($\approx 1/137$)
$N =$ Avogadro constant ($= 6{,}022 \cdot 10^{23}\,\mathrm{mol^{-1}}$)

The formula of Bethe-Bloch is valid for $\beta > Z \cdot \alpha$.

4.1.2. Energy Loss of Electrons

For electrons the Bethe-Bloch formula is not valid because electrons cannot be assumed to be heavy particles (electron mass = 1/2000 of the mass of a proton).
There are three additional effects:

- elastic scattering off shell electrons (Möller-Scattering)

- elastic scattering off nuclei (Mott-Scattering)

- emission of bremsstrahlung in the electric field of nuclei.

For relativistic electrons the following formula is a good approximation for the energy loss by ionization [Kle05]:

$$\left(\frac{\mathrm{d}E}{\mathrm{d}x}\right)_{ion.} = -F \cdot \frac{Z}{A} \cdot \rho \cdot \frac{1}{\beta^2} \cdot \left(\frac{1}{2}\ln\left(\beta^2\gamma^2\right) + G\right). \tag{4.2}$$

In general the energy loss by ionization is given by [Seg90]:

$$\frac{\mathrm{d}E}{\mathrm{d}x} = -\frac{F}{2} \cdot Z\rho\beta^2 \cdot \left(\ln\frac{m_e c^2 E_e}{I_{eff}^2} + \ln\frac{\beta^2}{D} - \left(2D + \beta^2\right)\cdot\ln 2 + D + \frac{1}{8}\left(1 - D\right)^2\right), \tag{4.3}$$

$D = 1 - \beta^2 = 1/\gamma^2$
$E_{kin} = $ kinetic energy of the electron (in eV).

Bremsstrahlung is dominating at high energies. The relation to the energy loss by ionization is

$$\frac{\left(\frac{dE}{dx}\right)_{brems.}}{\left(\frac{dE}{dx}\right)_{ion.}} = \frac{E_{kin} \cdot Z}{800\,\mathrm{MeV}}. \tag{4.4}$$

For lead with $Z = 82$ the energy loss by bremsstrahlung becomes larger than the energy loss by ionization for electron energies larger than $10\,\mathrm{MeV}$.

4.1.3. Multiple scattering

A charged particle traversing a medium is deflected by many small-angle scatters. Most of this deflection is due to Coulomb scattering from nuclei. This can be approximated statistically. The angle Θ_0 is defined as the angle relative to the plane of the incoming particle with

$$\Theta_0 = \Theta_{plane}^{rms} = \frac{1}{\sqrt{2}}\Theta_{space}^{rms}. \tag{4.5}$$

Θ_0 can be calculated by using [PDG06]:

$$\Theta_0 = \frac{13{,}6\,\mathrm{MeV}}{\beta c p}Z\sqrt{x/X_0}\left[1 + 0{,}038\ln\left(x/X_0\right)\right], \tag{4.6}$$

Z : atomic number of the scattering medium
p : momentum of the particle
c : vacuum speed of light
β : speed of the particle in units of c
x/X_0 : thickness of the scattering medium in radiations length[1].
Using this formula, e.g., a beam of muons with $p = 1\,\mathrm{GeV}/c$ ($\beta \approx 1$) will emerge with an angle of around $5{,}4\,\mathrm{mrad}$ after passing $100\,\mathrm{mm}$ of argon gas with $Z = 18$ and $X_0 = 109{,}7\,\mathrm{m}$.
For slow particles the effect of multiple scattering limits the coordinate resolution of detectors.

---
[1]the length were a particle has lost $1/e$ of its energy

4.2. Drift of electrons

Free electrons in gases have thermal energies as caused by collisions with atoms. They diffuse with an average velocity

$$\langle v \rangle = \sqrt{\frac{3kT}{m_e}} \tag{4.7}$$

corresponding to a thermal energy $\epsilon = \frac{3}{2}kT$ by multiple scattering with other electrons or atoms following a *Maxwell distribution* F for their energy ϵ:

$$\frac{\mathrm{d}N}{\mathrm{d}\epsilon} = F(\epsilon) = C\sqrt{\epsilon}\,\exp\left(\frac{-\epsilon}{kT}\right), \tag{4.8}$$

N : number of electrons
T : temperature
k : Boltzmann constant $(1{,}381 \cdot 10^{-23}\,\mathrm{J/K})$
C : constant.

After a time t the N electrons are dislocated following a Gaussian distribution (here for one space coordinate x):

$$\frac{dN}{N} = \frac{1}{\sqrt{4\pi Dt}}\exp\left(-\frac{x^2}{4Dt}\right)\mathrm{dx}, \tag{4.9}$$

$\sqrt{2Dt} = \sigma$: standard deviation for the space coordinate x after a time t
D : constant of diffusion
The average distance between two adjacent collisions of electrons on their way through matter is called *free path length* λ. The free path length depends on the cross section σ for interaction of the free electrons with atoms and on the density of the matter [Kle05]:

$$\lambda = \frac{1}{N\sigma(\epsilon)} = \frac{A}{N_A \cdot \rho \cdot \sigma(\epsilon)}, \tag{4.10}$$

N : number of particles per volume
A : relative atomic mass of matter
N_A : Avogadro constant $(= 6{,}022 \cdot 10^{23}\,/\mathrm{mol})$
ρ : density of matter.

Drift in electrical fields:
In an electrical field $\vec{E}$ electrons get an acceleration

$$\vec{a} = \frac{q\vec{E}}{m_e}, \tag{4.11}$$

so in the simplest model the macroscopic drift velocity v_{drift} in an electrical field is given by

$$v_{drift} = |<\vec{a}t>| = \frac{e}{m_e}|\vec{E}_{\|}|\,\tau \tag{4.12}$$

with the E-field $\vec{E}_{\|}$ parallel to the direction of v_{drift} and the mean interaction time τ between two collisions with atoms and assuming that the drifting electrons are stopped by the collisions. For an ideal gas

$$p \cdot V = R \cdot N \cdot T \tag{4.13}$$

with

p : gas pressure

V : volume of the gas

R : gas constant $(8{,}314\,\mathrm{JK^{-1}mol^{-1}})$

N : number of gas atoms

T : temperature

follows

$$\frac{1}{N} \propto \frac{T}{p}. \tag{4.14}$$

So using the proportionality between the number density N and the free path length λ (Equ.4.10) and Equ. 4.12 the mean interaction time follows :

$$v_{drift} \propto \frac{ET}{p}. \tag{4.15}$$

This is a good approximation for low E-fields (below $50\,\mathrm{V/mm}$ for an Ar/CO_2-mixture in ratio 85/15).

But τ itself depends on the energy ϵ of the drifting electrons:

$$\tau = \tau\left(\epsilon(|\vec{E}|)\right). \tag{4.16}$$

The mean interaction time $\tau(\epsilon)$ is linked to the cross section of the interaction $\sigma(\epsilon)$.
The collision cross section $\sigma(\epsilon)$ varies strongly with ϵ because the wavelength of the electrons have a similar scale compared to the dimensions of the molecules. So complex quantum mechanical processes like the *Ramsauer-Townsend effect* take place where the cross section for scattering varies very strongly with the drift electron energy. All these effects are important for non thermal electrons [Saul77].
Under general assumptions and for fields such that only a negligible fraction of electrons get enough energy to experience collisions with ionizations, one can deduce the energy distribution

$$F(\epsilon) = C\sqrt{\epsilon}\exp\left(-\int \frac{3\Lambda(\epsilon)\epsilon\,d\epsilon}{[eE\lambda(\epsilon)]^2 + 3\epsilon kT\Lambda(\epsilon)}\right), \tag{4.17}$$

where $\Lambda(\epsilon)$ is the fraction of energy loss at each impact. If $\sigma(\epsilon)$ is known the drift velocity and the diffusion coefficient can be calculated:

$$v_{drift}(E) = -\frac{2}{3}\frac{eE}{m_e}\int \epsilon\,\lambda(\epsilon)\frac{\partial\left[F(\epsilon)u^{-1}\right]}{\partial\epsilon}d\epsilon \tag{4.18}$$

$$D(E) = \int \frac{1}{3}u\,\lambda(\epsilon)F(\epsilon)d\epsilon, \tag{4.19}$$

where $u = \sqrt{2\epsilon/m_e}$ is the instantaneous velocity of electrons of energy ϵ. A detailed derivation of these equations using the *Transport Equations* can be found in [Her91].
For gas mixtures with partial pressure p, $v_{drift}(E)$ and $D(E)$ can be calculated by using

$$\sigma(\epsilon) = \sum p_i\,\sigma_i(\epsilon) \qquad \text{and} \qquad \sigma(\epsilon)\Lambda(\epsilon) = \sum p_i\,\sigma_i(\epsilon)\,\Lambda_i(\epsilon). \tag{4.20}$$

The simulation program Magboltz [Mag02] can calculate the drift velocity v_{drift} and the diffusion coefficient $D(E)$ using a database for $\sigma(\epsilon)$ and numerical integration of (4.18) and (4.19).

For non thermal electrons the drift velocity does not increase linearly with T and $1/p$ but it becomes a function of E/p (see Sec.8.2).

Drift in electric and magnetic fields:
Particles with charge q and a velocity $\vec{v}$ in a magnetic field $\vec{B}$ move on a helix with radius r because of the *Lorentz force* $q\vec{v} \times \vec{B}$. The angular velocity, called *Cyclotron frequency*, for electrons with mass m_e is

$$\vec{\omega} = -\frac{q\vec{B}}{m_e}. \tag{4.21}$$

The components of the velocity $\vec{v}_{drift}$ in an electric field $\vec{E}$ and a magnetic field $\vec{B}$ can be parsed into the translational drift velocity $\vec{v}_D$ and a circular motion with the angular frequency $\vec{\omega}$:

$$\begin{aligned} \vec{v} &= \vec{v}_D + \vec{\omega} \times \vec{r}_b \tag{4.22} \\ &= \vec{E} \times \vec{B}/B^2 + \frac{q}{m}\vec{E}_\| + \vec{\omega} \times \vec{r}_b \tag{4.23} \end{aligned}$$

$\vec{E}_\|$ is parallel to $\vec{B}$ and $\vec{r}_b$ is the position vector perpendicular to $\vec{v}_D$. Additionally there is a stochastic force $m\,\vec{a}_s(t)$ (a_s = acceleration) caused by collisions of the drifting electrons with atoms. Thus, the equation of motion is:

$$m\,\vec{a} = q\left(\vec{E} + \vec{v} \times \vec{B}\right) + m\,\vec{a}_s(t) \tag{4.24}$$

After averaging over time and assuming a constant $\vec{v}_{drift}$ for a constant $\vec{E}$ one gets this expression for $\vec{v}_{drift}$ (for details see page 32 of [Kle05]) :

$$\vec{v}_{drift} = \frac{q\tau}{m\left(1 + \omega^2\tau^2\right)}\left(\vec{E} + \frac{\vec{E} \times \vec{B}}{B}\omega\tau + \frac{(\vec{E} \cdot \vec{B}) \cdot \vec{B}}{B^2}\omega^2\tau^2\right). \tag{4.25}$$

For $\vec{E} = (E_x, 0, E_z)$ and $\vec{B} = (0,0,B_z)$ and small angles between $\vec{E}$ and $\vec{B}$ ($E_x << E_z$) one deduces:

$$\begin{aligned} v_x &= \frac{q\tau}{m_e}E_x\frac{1}{1 + \omega^2\tau^2}, \tag{4.26} \\ v_y &= -\frac{q\tau}{m_e}E_x\frac{\omega\tau}{1 + \omega^2\tau^2}, \tag{4.27} \\ v_z &= \frac{q\tau}{m_e}E_z. \tag{4.28} \end{aligned}$$

For orthogonal E- and B-fields ($\vec{E} = (E_x,0,0)$, $\vec{B} = (0,0,B_z)$) one obtains:

$$\begin{aligned} v_x &= \frac{q\tau}{m_e}E_x\frac{1}{1 + \omega^2\tau^2}, \tag{4.29} \\ v_y &= -\frac{q\tau}{m_e}E_x\frac{\omega\tau}{1 + \omega^2\tau^2}, \tag{4.30} \\ v_z &= 0 \tag{4.31} \end{aligned}$$

and

$$|\vec{v_{drift}}| = \frac{q\tau}{m_e}E_x\sqrt{\frac{1}{1 + \omega^2\tau^2}}. \tag{4.32}$$

The angle between $\vec{v}_{drift}$ and $\vec{E}$ is called *Lorentz angle*:

$$\tan \alpha_L = \omega\,\tau = \frac{2\,B\,v_{drift}}{E}. \tag{4.33}$$

With the Lorentz angle one can calculate the additional path length (Fig. 4.1) electrons have to travel if an additional B-field is applied to an E-field. So one can define an effective drift velocity

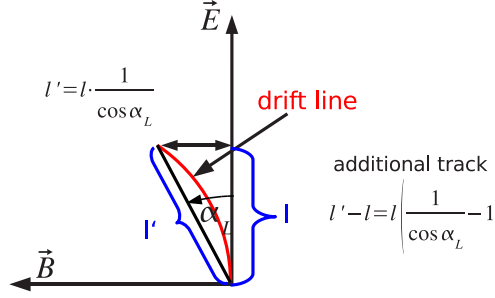$$v_{drift,eff.} = v_{drift} \cdot \cos \alpha_L. \tag{4.34}$$

Figure 4.1.: *Definition of the Lorentz angle.*

For non-thermal electrons (high electric fields) these relations are not valid anymore and one has to calculate v_{drift} and α_L numerically by using equations like Equ. 4.18.

4.3. Avalanche in Gas

In very high electric fields (above $\approx 1\,\text{kV/mm}$) electrons are accelerated so strongly that they ionize atoms and the produced free electrons can ionize further atoms. A cascade is created and the number of incoming drift electrons is amplified by a factor

$$G = \frac{N_{out}}{N_{in}}. \tag{4.35}$$

With an avalanche factor G of up to 10^6 a single drifting electron can produce a signal up to $1\,\text{mV}$ on a wire read out by a coupling capacitor of $1\,\text{pF}$. For example the electric field around a single wire with diameter r_1 and inside a grounded cylinder with radius r_2 as a function of the distance from the wire r is

$$E(r) = \frac{V_0}{r \ln\left(\frac{r_2}{r_1}\right)}. \tag{4.36}$$

Using this equation the region for the avalanche in the gas around the anode wire can be estimated.

In case of a gas mixture of Ar/CO_2 85/15 the avalanche region (here $450\,\text{V/mm}$ [Saul77]) begins approximately in a distance of $1\,\text{mm}$ to the wire connected to a voltage of $2\,\text{kV}$ with a diameter of $25\,\mu\text{m}$ and a cylinder with a radius of $2\,\text{mm}$.

4.4. Gas Ionization Detectors

If a charged particle traverses a gaseous volume of a detector, atoms of the gas are ionized producing ions and free electrons. The ions and/or electrons cause electrical signals that can be measured. This is done by attracting them by an electric field inside the detector.
Advantages of gas ionization detectors are:

- Large areas can be covered.

- cheap

- medium rates for traversing particles (up to 10 events /mm^2) are possible

- radiation resistance (in the majority of cases)

Limitations of gas detectors are:

- medium spatial resolution, $(50 \ to \ 300)\,\mu m$

- special versions for high magnetic fields needed

- in the majority of cases amplifiers needed.
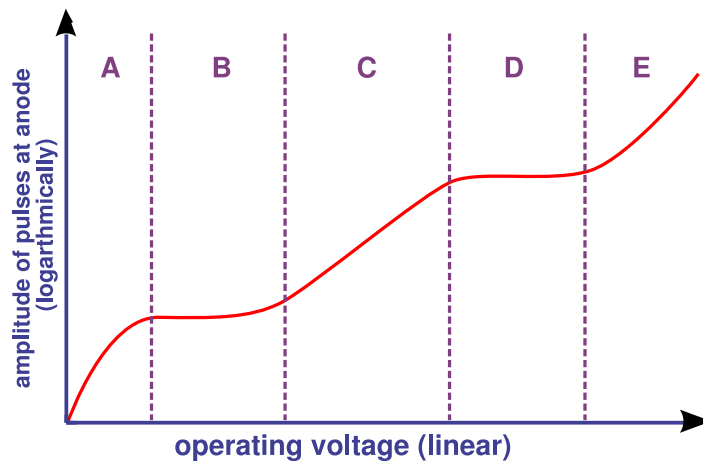
4.4.1. Proportional Chambers

Figure 4.2.: *Operating regions of gas ionization detectors: (figure from [Wik07])*
A) recombination region: In this region free electrons and ions recombine before they can be detected.
B) ionization chamber: Free electrons drift to the anode.
C) proportional region: Electrons freed by ionization are accelerated so that they can induce avalanches in the gas. The avalanche factor causing the amplitude of the pulses is a linear function of the operating voltage. For a fixed voltage the number of electrons in the avalanches is proportional to the number of free electrons created by ionization.
D) plateau: Here Geiger-Müller counters operate. The amplification is so large that the pulse amplitude is independent from the number of traversing particles. This is also called saturation mode.
E) gas discharge: Continuous discharges occur in the gas volume.

In a proportional chamber the strength of the electric field is chosen so that the output signal is proportional to the operating voltage (compare to Fig. 4.2).

In a simple proportional chamber the produced electrons are detected by one anode wire. Special types of proportional chambers are multiwire (Sec. 4.4.2) and drift chambers (Sec. 4.4.3).
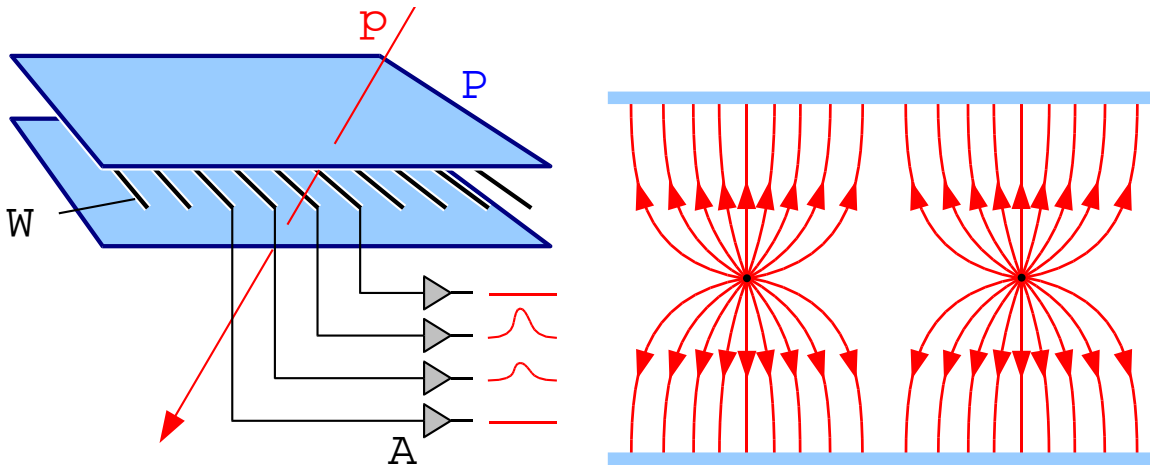
4.4.2. Multiwire Proportional Chambers

Figure 4.3.: *Left) sketch of a multiwire chamber (figure from [Wik07]): Between two plates (P) acting as cathodes multiple wires (W) are placed as anodes (A). If a particle (p) traverses the volume the gas is ionized, a signal can be measured by the anode wires nearby. By interpolating the measured strip charge [MUO97], the accurate distance to the wire can be reconstructed. Right) modeled shape of the electric field inside a multi wire proportional chamber (figure from [Wik07]).*

Multiwire proportional[2] chambers are proportional chambers with many anode wires. The field is formed by these wires and often by additional field shaping wires, which are not to be read out.

By using additional anode wires the position of the particle track can be determined more precisely because here more wires can be placed in a smaller volume and so more points can be measured. Additionally the form of the signal (Fig. 4.3) can be used to achieve a higher precision.

---

[2]Nobel prize to Georges Charpak (*1924) in 1992
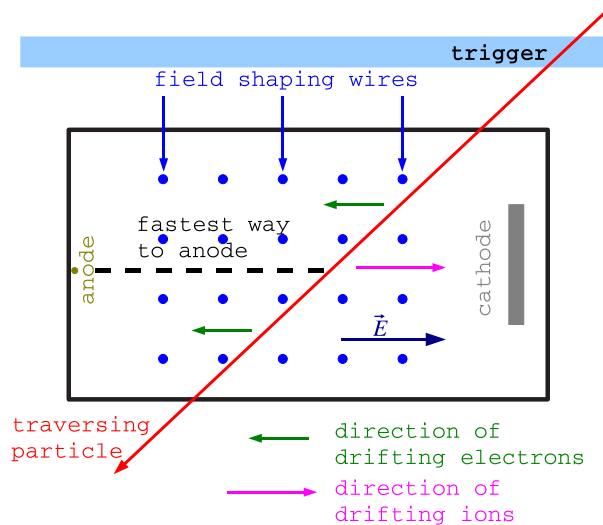
4.4.3. Drift Chambers

Figure 4.4.: *Drift chamber: principle of operation.*

A drift chamber is a proportional gas chamber where the drift time of electrons towards the anode is measured (see Fig. 4.3). Therefore an external trigger is needed which determines the time of the particle's passage. The trigger signal is taken from another detector (usually scintillators), from the time when the particle was created (bunch crossing including time of flight calculations) or it can be reconstructed from the track measurement using several drift cells. The difference in time between trigger and measured signal can be translated into a spatial distance from the wire.

If a particle traverses a drift chamber it will produce free electrons by ionization along its track. Usually the electrons from the point with the shortest distance to the anode wire will reach it first. By combining several wire measurements a track can be reconstructed. For calculating the length of the drift path s using the drift time t_{drift} the *drift velocity* v_{drift} is needed:

$$s = v_{drift} \cdot t_{drift}. \tag{4.37}$$

In the presence of magnetic fields and inhomogeneous electric fields a straight line between the particle's track and the anode wire is not always the realized drift path.
Also, in general for a minimal ionizing particle the region where drift electrons are created is different for each event. This is due to the fact that the distance between two ionizations along a particle track is Poisson distributed. In addition to this, the ionized electrons can gain energy to ionize other atoms themselves. This process is also known as creation of *δ-electrons* where secondary ionizations in addition to those from the original track are created. If the δ-electrons pass closer to the anode wire than the original track the original hits can be masked and thus the precision of the track measurement is affected.
In general the present electric and magnetic fields have a huge impact on the drift velocity (Sec. 4.2), which is an important parameter for precise track reconstruction.

4. Drift Chambers

5. Design and Construction of the VDC

The basic principle of operation (Fig. 5.1) of the CMS VDC is a measurement of time differences. The time difference between the arrival at a signal wire of drifting electrons created by two β-particle beams at certain positions is measured. The drift times are measured relative to a trigger signal caused by the β-beam particles after traversing the chamber. Knowing the distance between the β-beams the drift velocity can be calculated.

There is one prototype. With the prototype nearly all measurements have been made. For the installation at CMS six series production chambers have been produced and a seventh series production chamber is foreseen to stay in Aachen for reference measurements.

5.1. Design of the Chamber

At the L3 experiment at LEP, an e^+e^-−machine, there was also a small special drift chamber for controlling the drift velocity [Böh89], called "gas test chamber". It was used to monitor a special kind of drift chamber, a **T**ime **E**xpansion **C**hamber, for the inner part of the L3 detector working with CO_2/CH_4 in ratio 80/20 as drift gas. The L3 VDC had a HV robustness of up to around $-5\,kV$ corresponding to an electric field of $80\,V/mm$.

The CMS VDC is based on the L3 VDC. Improvements were needed because for CMS much higher E-fields are needed and the electric strength of the L3 VDC was not adequate. So some changes in the cathode region had to be done to start with. Subsequently, also the homogeneity of the electric field was improved [Alt06].

5.2. Requirements

A VDC system for the barrel muon system of the CMS detector should fulfill the following requirements:

1. very homogeneous E-field

2. same region for the maximum reachable E-field as the maximum E-field in the muon chambers.

3. The time for a measurement of the drift velocity should be as short as possible

4. The chamber volume should be small so that a fast gas exchange is possible to test the gas from different muon chambers in short time intervals.

5. The chamber should be usable for the whole period of the CMS experiment.

6. The running system should produce no high service costs.

7. The complete system should be controllable from outside.

Comments:

1.) A very precise theoretical calculation of $v_{drift}(E)$ is not possible. Thus, one cannot calculate the drift velocity for a certain E-field from the measured value in an inhomogeneous E-field (with known local values of the E-field). A homogeneous E-field will cause a macroscopic constant drift velocity. So the drift velocity can be measured for these E-field values.

2.) The E-field in the DT muon chambers is inhomogeneous (variation of up to 50 % around the average). Thus, for a path of a drifting electron the drift velocity is generated by all the different E-fields. The drift velocities for all E-field values inside the muon chambers have to be known to calculate the drift velocties for all drift paths inside a muon chamber. Therefore the VDC should be able to run at a large fraction of all the E-fields inside the muon chamber and especially at the E-field that is mostly present inside a muon chamber. Given by the dimension of the VDC and the desired field strength the design value for the maximum cathode voltage is $-15\,\mathrm{kV}$ corresponding to an E-field of $227\,\mathrm{V/mm}$. The VDC should also run stably with a cathode voltage of $-16\,\mathrm{kV}$, as safety margin.

3.) A goal for the performance of the VDC is to measure the relative v_{drift} (variation with time) with a precision better than 10 ‰. Therefore the statistical error should be below 1 ‰ (see Chap. D of the appendix). This precision should be reached in around $10\,\mathrm{min}$, which is in the same order of magnitude as the time a VDC is connected to the outlet of a certain muon chamber.

4.) The flow per DT chamber is around $50\,\mathrm{L/h}$. Only a small amount of the outlet flow is conducted through the VDC for analysis. And there a VDC, an oxygen analyzer and a humidity analyzer are connected in parallel. A flow of around $5\,\mathrm{L/h}$ will flow through one VDC. Assuming a sufficient time for exchanging the gas in a VDC after changing the input muon chamber the chamber volume should not be larger than $1\,\mathrm{L}$.

5.) Six VDCs will be installed at CERN. Thus, e.g. in case of aging, replacing each chamber after some time will be too expensive. The LHC is supposed to run about ten years and because the functionality of the VDCs is independent from the accelerator parameters, the VDCs can also be used for the SLHC[1]. Thus, including an assumed additional runtime of five years for the SLHC its lifetime should be larger than 15 years.

6.) In order to stay within the budget all expensive components like the trigger system or the radioactive sources should have a lifetime larger than 15 years. Only some cheap services like cleaning or replacing the anode wires should be necessary.

7.) Although the room where the VDCs will be placed is accessible at any time, there will not always be an operator. The system should be remote controllable and some small electronic adjustments should also be possible from outside.

---

[1] **S**uper **L**arge **H**adron **C**ollider, the LHC with higher luminosity
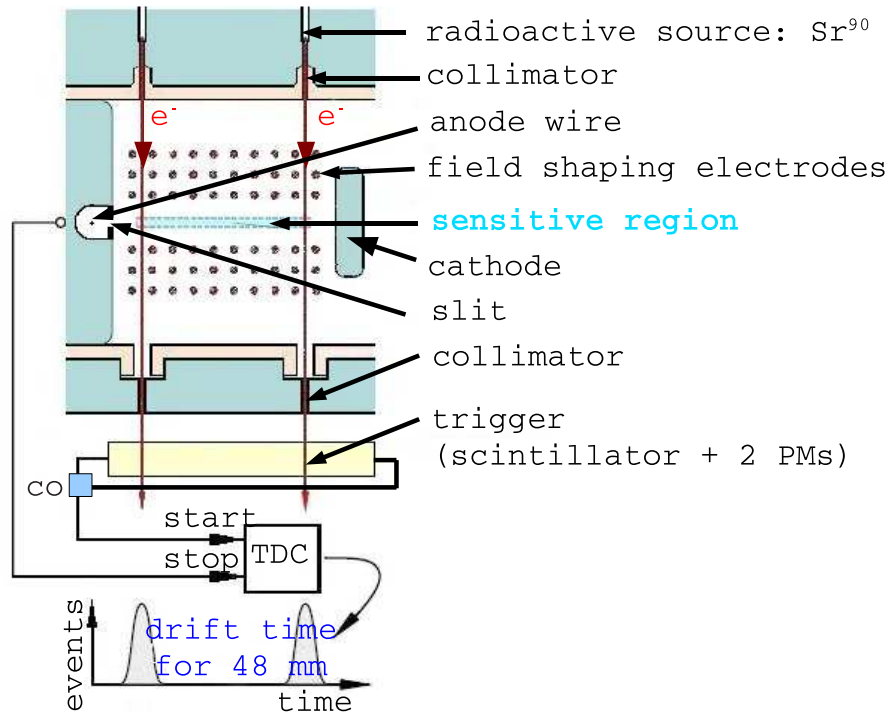
5.3. Principle of Operation

Figure 5.1.: *The principle of operation of a CMS VDC: The time between a trigger signal caused by a coincidence (co) of two light detectors (**P**hoto**M**ultipliers) and the arrival of the generated drifting electron at the anode is measured [Rei07].*

To generate drift electrons two β-sources (^{90}Sr, half-life period: 28,5 years [PDG06]) with an activity of 10 MBq (5 MBq for the prototype) for each source[2] are placed outside the chamber. $^{90}_{38}$Sr decays per β-radiation into $^{90}_{39}$Y in a half-life period of 28,5 years and a maximum kinetic energy of the β-particles of 546 keV. $^{90}_{39}$Y decays into $^{90}_{40}$Zr in a half-life period of 64,10 h and a maximum kinetic energy of the β-particles of 2283 keV [PDG06]. Because the mean kinetic energy for a β-spectrum can be approximated by 1/3 of the maximum kinetic energy, most of the particles from the first part of the decay chain do not cause a trigger signal. They are stopped inside the VDC or they have not enough energy to create enough light inside the scintillator (Chap. 6.

The chamber has outer dimensions of around 200 mm $\times$ 120 mm $\times$ 100 mm and an inner volume of around 1 L (Fig. 5.4). In front of the sources there is a round collimator with a diameter of 1 mm and a length of 17 mm leading into the chamber. At the opposite side of the VDC, at a distance of 109 mm from the source, there is a rectangular second collimator of 2 mm $\times$ 10 mm. Because of the first collimator the β-beams are "focused" to a circle with a diameter of 6,42 mm on the second collimator. For two 10 MBq sources a β-particle rate of 430 Hz is expected behind the second collimator [Alt06]. The inlet and outlet of the β-beams is covered by very thin polyethylene terephthalate polyester films (Mylar). The outgoing β-electrons pass a scintillator and create light in it. The light is detected by two light detectors at the ends of the scintillator.

---

[2]10 MBq is the maximum activity of each source which is allowed for the level of radiation control foreseen for this room at CERN

The logical AND of both light detectors is the trigger signal (Chap. 6), which defines the time $t = 0$.

In the gas filled volume of the VDC between the two β-beams there is a very homogeneous electrical field around the middle of the chamber (Sec. 5.4.2). Along the track of the β-particles the gas is ionized. Because of the electrical field the created free electrons drift toward the anode (see Sec. 4.2). The ions drift towards the cathode where they are neutralized. In the homogeneous E-field the electrons have in average a constant macroscopic drift velocity. The anode is separated from the drift room by a wall with a 2,5 mm wide slit, so that only drifting electrons from the regions in the middle of the drift room can reach the anode. Near the anode (1 mm distance) a gas avalanche (Sec. 4.3) occurs and an analog electrical signal can be read out at the anode wire. Because of the slit only drifting electrons created by the β-beams from two small regions along the central path of the chamber can reach the anode wire. Two different travel times, corresponding to the two β-beams arriving at the anode, are measured. The measured drift times are filled into a histogram, the drift time spectrum (Fig. 5.2). From gaussian fits to the peaks the times of the arriving drift electrons are obtained (see Sec. B of the appendix for details.)
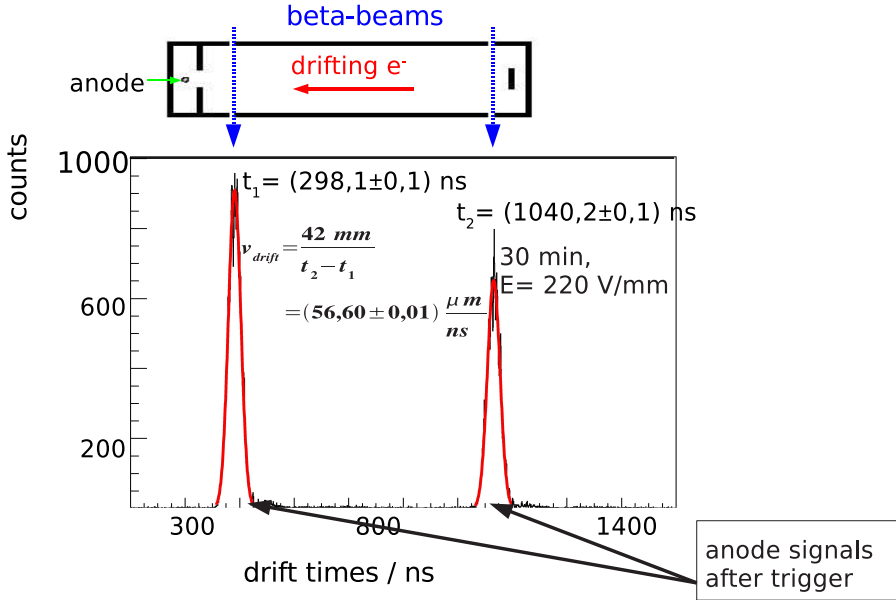

Figure 5.2.: *Example of a measurement in form of the corresponding drift time spectrum.*

The measurement of the time difference between the signals created by two sources leads to two major advantages:

1. Only the homogeneous part of the electrical field influences the drift time measurement.

2. Nearly all electronic timing effects at the trigger system and especially at the anode cancel when calculating the time difference.

Given the dimensions of the VDC, the E-field E between the two β-beams can be calculated by

$$E = \frac{U_{cathode}}{66{,}0\,\mathrm{mm}}, \tag{5.1}$$

where $U_{cathode}$ is the voltage at the HV power supply (compare to Sec. 5.4.3).

5.4. Structure of the VDC

5.4.1. The Mechanical Setup

The electrically charged parts of the VDC are made of aluminum because of shielding against outside electrical fields and mechanical precision and stability. All plastic parts are made of Polyamid (PA6) because it does not carbonize after high voltage discharges[3]. The aluminum and plastic parts are produced on a CNC[4] milling machine with a precision of around $10\,\mu m$.
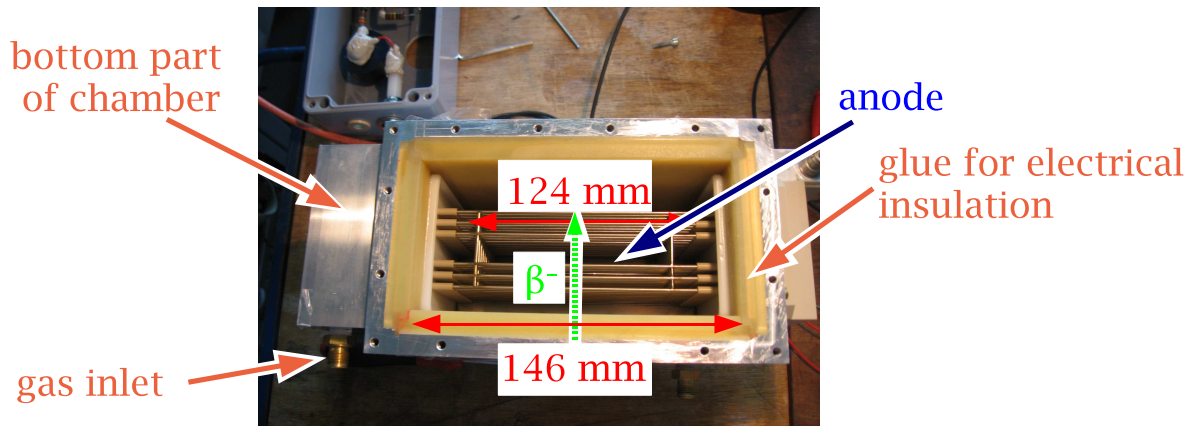

Figure 5.3.: *The inside of a CMS VDC with field shaping tubes of $2\,mm$ diameter.*
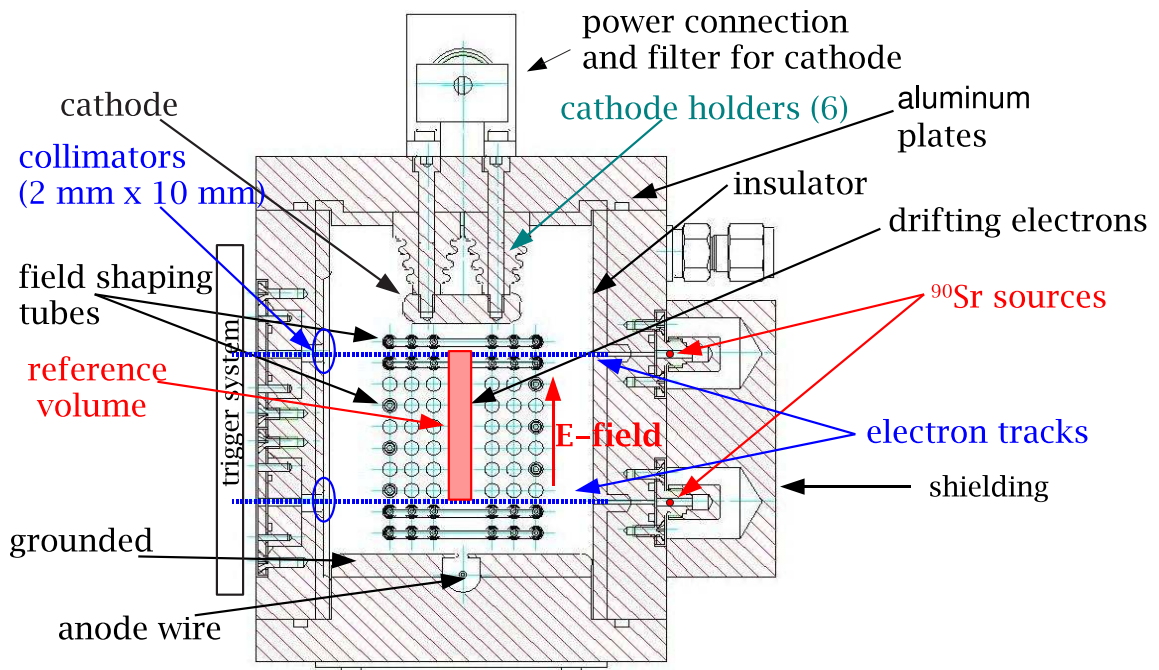
Figure 5.4.: *Structure of a CMS VDC.*

---

[3]with some constructional disadvantages when gluing to aluminum [Gro06]

[4]**C**omputerized **N**umerical **C**ontrol

All six plates framing the drift volume are removable for maintenance. Especially the front side including the anode region and the back side including the cathode can easily be removed. Thus, the chamber can be cleaned.

Below the drift volume "box" at the bottom part of the chamber there is a gas volume which distributes the gas coming from an inlet flowing through many small holes into the drift volume. Also some electronics is located here (Sec. 5.4.3).

Behind the backplate there is a box including high voltage filters (Sec. 5.4.3) for the cathode and the field shaping elements.

The field generating and shaping elements:
The electric field inside the VDC is generated by a cathode (an about $100\,\text{mm} \times 20$ mm thin block of aluminum) and an anode wire with a diameter of $25\,\mu\text{m}$ (Fig. 5.3).

Between them there are ten grids of field shaping tubes with a diameter of 2 mm. Each grid (Fig. 5.5) consists of six tubes which are connected by two tubes vertical to them. The geometry of the field shaping tubes, the cathode and anode have been optimized by simulations (Sec. 5.4.2, [Alt06]). The grids have been laser welded for a maximum precision.

Figure 5.5.: *One grid of field shaping tubes. On the upper left one can see the connector for the high voltage.*

Above the drift room there is a block of plastic including holes for the HV connector to the field shaping tubes and a plastic box including the voltage divider (Sec. 5.4.3).

Shielding of radioactive sources:
For shielding purpose the radioactive sources are covered by a block of lead which is let in the corresponding plate of the drift volume as a "chicane" for the β-radiation. The measured dose directly at the shielding with two 5 MBq ^{90}Sr-sources is below $1\,\mu\text{Sv/h}$. Even using 10 MBq ^{90}Sr-sources, which is the highest activity for one source allowed in the gas room at CERN, a limit of $3\,\mu\text{Sv/h}$ [Poo06] is respected. This limit is set by the regulations for radiation protecting in the FRG[5] for the VDC laboratory in Aachen[6].

---

[5]**F**ederal **R**epublic of **G**ermany
[6]called "Überwachungsbereich"

Improvements for HV robustness:
The prototype in its final status runs stably with a cathode voltage up to $-14{,}5\,\text{kV}$ (Sec. 7.2). The backplate region behind the cathode was identified as the main problematic region. To reach the design value ($-16\,\text{kV}$) some improvements were needed. Thus, four precautions have been realized (Fig. 5.6) [Rei07, Gro06] :

1. Enlarging the distance between cathode and backplate (and with it the VDC) by $10\,\text{mm}$ to around $15\,\text{mm}$: Following an empiric value of needed $2\,\text{mm/kV}$ [Hil07] with this improvement the designed HV-robustness should be reached if there are no HV-flashovers along the holders or other effects.

2. Coating the backside and half of the side of the cathode with an insulating glue: Then HV-flashovers cannot go the direct way to the cathode.

3. Using holders for the cathode which are embedded into the backplate [Rei07]: HV-flashovers cannot go to the backplate passing possible small slits between the glue and the holders.

4. Using a HV-supply connector for the cathode which is coated completely by plastic. It reaches several millimeters from the cathode to the outside of the backplate [Gro06]: The insulation around the cathode voltage supply connector is thicker than the previous insulation consisting of a heat shrink tube. Additionally there is a longer way from the cathode to the backside of the backplate resp. the wall of the HV-filter box compared to using two parts for insulating the cathode voltage supply connector.
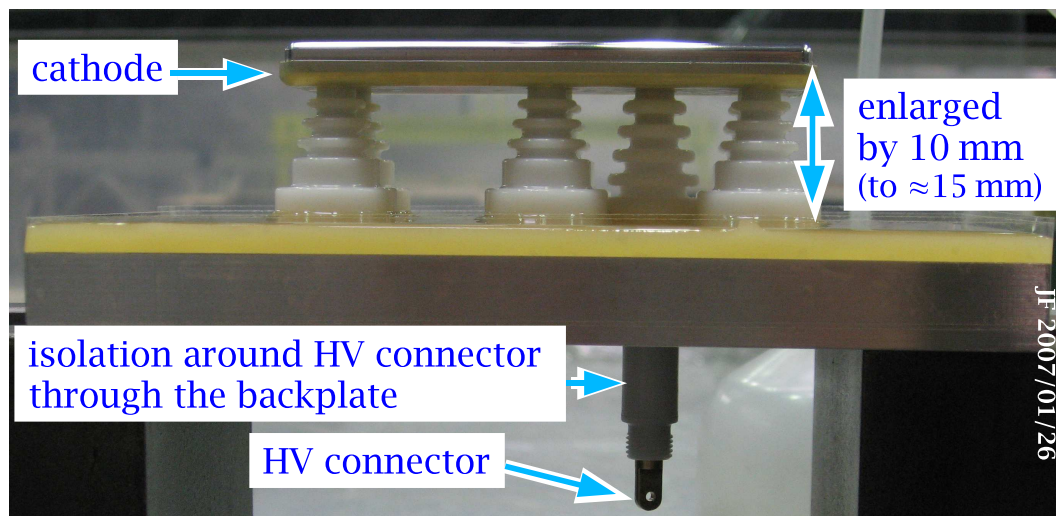

Figure 5.6.: *The backplate of the VDC including the cathode after all improvements.*

5.4.2. Simulations of the Field

The simulation of the electric field was done to optimize the geometry of the field shaping elements. This was done with Garfield [Gar05] and COMSOL Multiphysics [COS06]. Running these simulations it was found out that with small tubes a more homogeneous field could be generated than with wires. Moreover they are mechanically more robust [Alt06].
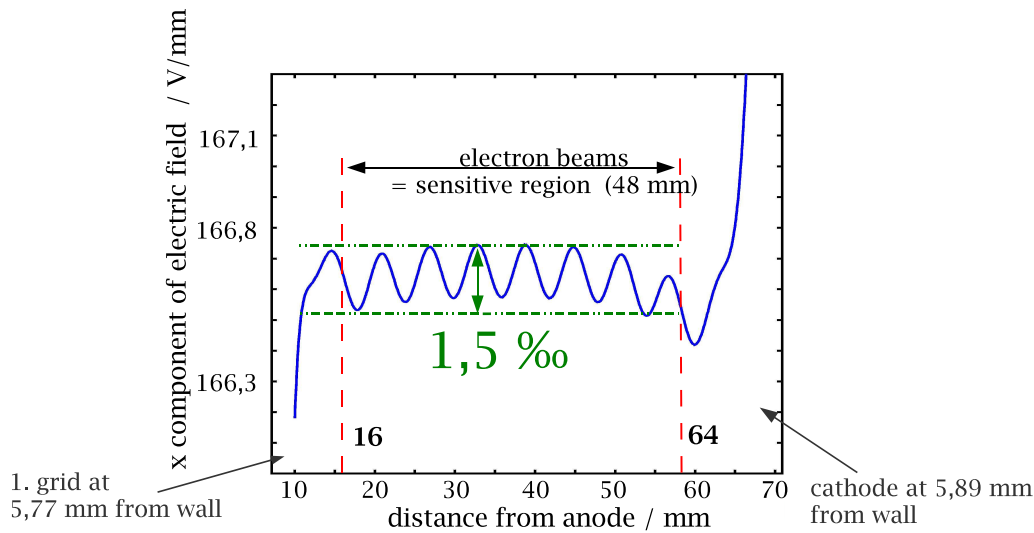

Figure 5.7.: *Simulation of the x-component of the electric field inside the VDC with Garfield [Gar05, Alt07].*

5.4.3. Chamber Electronics

The electronics inside the bottom part of the chamber:

- The signals from the anode wire are decoupled from the HV by a capacitor. A preamplifier (which has been used in the UA1-experiment[7]) amplifies those signals. It is necessary to place the preamplifier close to the anode because the anode signals are smaller than $1\,\text{mV}$ and therefore, they are very sensitive to noise [Hil07].

- One (prototype) or two (final version of VDC) temperature sensors [Dal07]: They have to be placed in the gas flow at a certain distance to heat sources (like the preamplifier) to measure the temperature of the gas. Because there were some failures of temperature sensors in the prototype VDC it was decided that two of them should be used.

- A connector (D-sub 15) is glued (for gas tightness) into a wall for the connections of the electronics to the outside. For the final version of the VDC two additional Lemo connectors are used.

The anode HV connection:

It is located at the top of the VDC, containing three capacitors to filter out the AC-components of the voltage, see Fig. 5.8. At the anode voltages between $1,4\,\text{kV}$ and $2,8\,\text{kV}$ are applied.

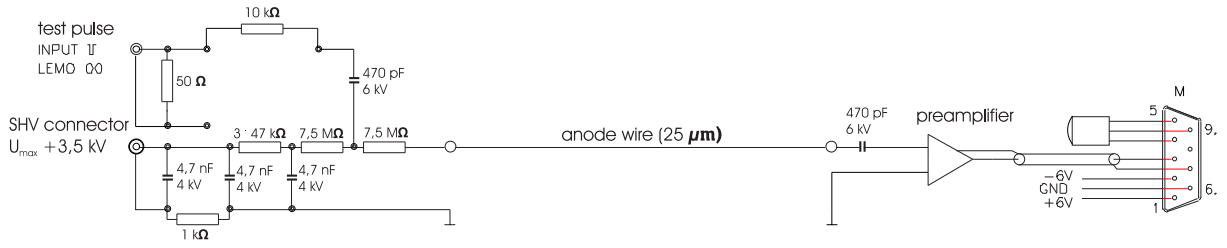[7]a detector at the **S**uper **P**roton **S**ynchrotron experiment at CERN

Figure 5.8.: *The electronics at the HV-side of the anode. At the lower left three capacitors for filtering can be seen. The resistor of $1\,\mathrm{k\Omega}$ between the first and the second capacitor is used to reduce effects of noise from the ground [Hil07].*

The cathode power connection:

Because here the voltage of up to $-15\,\mathrm{kV}$ for the cathode is applied, the inside of the box is covered with glue. To filter the supply voltage four capacitors are used here.
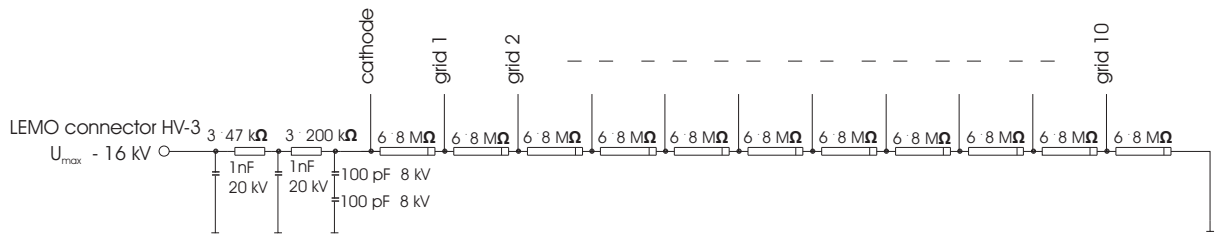

Figure 5.9.: *The electronics inside the box for filtering the voltage for the cathode and distributing the voltage to the field shaping tubes [Hil07].*

The voltage divider:

To form the electric field (Sec. 5.4.2) a voltage is connected to the grids of field forming tubes. The voltage is reduced step by step from one grid to the next as seen from the cathode side.

This is done by placing resistors between the power connections to each grid. The resistors are located inside a plastic box at the top of the VDC. To ensure HV robustness they are embedded in glue. To minimize the current, six resistors of $8\,\mathrm{M\Omega}$ have been chosen to be used between each grid. So the current to the cathode and the field shaping types (Fig. 5.9) is around $28\,\mathrm{\mu A}$ for the maximum cathode voltage of $-15\,\mathrm{kV}$.

To ensure the E-field homogeneity of 1,5 ‰ (Fig. 5.7) the deviations between the sum of the six resistors between the grid to each other has to be below $20\,\mathrm{k\Omega}$. Thus, after all resistors are glued additional resistors are added to compensate the resistance between each grid. The resistance between each grid is measured by a precise multimeter [Flu07] which can measure the resistance in the region up to $100\,\mathrm{M\Omega}$ with a precision of 0,1 ‰. The maximum difference in resistance between any pair of grids can amount up to $20\,\mathrm{k\Omega}$ [Lam07].

Because of the resistors inside the cathode power connection box of total $R_{pre} = 720\,\mathrm{k\Omega}$, the voltage at the cathode and the field forming tubes is slightly different. The corrected voltage U_{cor} to calculate the E-field between the two β-beams (Equ. 5.1) is given by:

$$U_{cor} = U_{cathode} \cdot \frac{R}{R + R_{pre}} \approx 0{,}9987, \tag{5.2}$$

$U_{cathode} =$ voltage at HV power supply
$R =$ total electrical resistance of voltage divider $(= 11 \cdot 49\,\mathrm{M\Omega})$.

5.4.4. Gas Tightness

For testing the current gas in the CMS gas system the gas should not be contaminated inside the VDC. Thus, the gas tightness of the VDC should ensure that effects of contaminations are so small that they cannot be measured. The actual amount of contamination is very difficult to measure (and calculate). Therefore the loss of pressure as a function of time was checked (Sec. 7.1). Because the chamber should be dismountable (Sec. 5.2), it is not possible to glue all parts to each other which would result in the best gas tightness.

Instead, the plates of the drift room are sealed with a tightening liquid. The tightening liquid does not outgas anything influencing the drift velocity or damaging the muon chambers or the gas system in general. To tighten the front plate, the backplate and the bottom part of the chamber rubber seals (in an "O" shape, called *O-rings*) are used. All electrical connections are glued into the aluminum and plastic parts. A time constant of around 2 h for pressure loss, see Sec. 7.1, can be achieved.

5.5. Readout and Trigger Electronics

5.5.1. The Electronics Setup in Aachen

A considerable part of the electronics used for measurements (Fig. C.1 of the appendix) with the VDC prototype and the first tests of series production VDCs is not identical to the electronics foreseen at CERN. The basic functions of the current electronics are comparable to the foreseen future electronics. Thus, the operation and the precision of the VDC system should be kept unchanged.

The anode readout:
In a box mounted on the anode side of the chamber there is a discriminator used for pulse forming which is creating a digital NIM[8]-pulse if the (absolute) pulse amplitude exceeds a predefined threshold. These NIM-pulses from the anode are converted to ECL[9]-pulses by a digital to digital converter. These data are taken by a TDC[10] [Caen05] in a VME[11]-crate. The TDC measures the time difference between the trigger pulse (Chap. 6) and the anode signal. For the used TDC mode ("start gating mode") the trigger signal was enlarged in time to define a window for the anode signals starting with the trigger signal [Zil07].

Photomultiplier HV supply:
The HV supply for each of the two photomultipliers is delivered by a CAEN N126 NIM-module which cannot be read out electronically.

HV supply for anode and cathode:
To monitor the current and voltages and to set the voltages by a computer program a CAEN SY-127 system with HV-modules for anode and cathode voltage supply were used. A second PC with software based on [SUR02] was connected to the SY-127 crate via a CAEN-Bus controller

---

[8]Nuclear Instrument Module, amplitude normed to $-0,8$ V
[9]emitter coupled logic, standard pulse
[10]Time To digital Converter
[11]VERSA module Eurocard

inside a CAMAC[12]-Crate.

The maximum readout frequency for data (voltages and currents) is around $1\,\mathrm{Hz}$.

5.5.2. Electronics Foreseen for the System at CERN

There will be a completely new setup of electronics for the final system at CERN based on VME-electronic including HV-supplies which can be remotely controlled by the VME-bus. There will be newly developed discriminators and coincidences (Fig. C.3 of the appendix) [I3A07] with built in counters. Using these counters the rates of anode and trigger signals can be monitored independently from the TDC.

5.6. The Gas System in Aachen
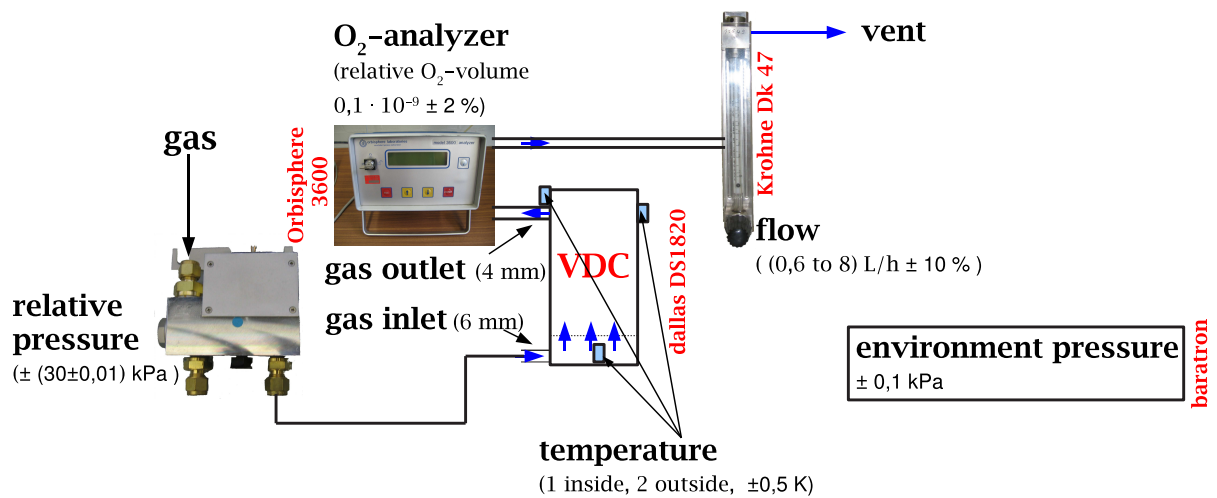
Figure 5.10.: *The gas system used for measurements in Aachen with all components.*

For testing the gas tightness, measuring the pressure in the VDC, the temperature of the gas, the oxygen content of the gas and the gas flow a gas system was built step by step.

The temperature is measured by one temperature sensor [Dal07] in bottom part of the chamber, one at the left side of the VDC and one on the right side. These temperature sensors have a direct digital output so that they can be read out directly by a RS-232[13] interface.

The fresh gas from a gas bottle can be directed to an oxygen analyzer [Orb97] without passing the VDC to measure the oxygen content in the gas from the bottle. Also the gas coming out of the VDC can be analyzed so that the oxygen content, which enters the VDC from outside, can be measured. The oxygen analyzer can measure a relative oxygen volume down to 10^{-10} with a precision of $2\,\%$.

A pressure device is placed between the gas bottle and the VDC. It includes two sensors with a range of $10\,\mathrm{kPa}$ and $50\,\mathrm{kPa}$ measuring the relative pressure between the inside and the environment. The readout is done by a 14-bit ADC[14] [SZC04]. To determine the absolute pressure, a pressure device (Baratron) measures the pressure in the room. To test the gas tightness the gas tubes at the inlet of the pressure sensor and the outlet of the VDC can be closed.

---

[12]Computer Automated Measurement And Control
[13]RS=Radio Sector
[14]**A**nalog-to-**D**igital **C**onverter

The gas flow is measured by a mechanical flow meter from Krohne [Krohne07], which can not be read out electronically, at the output of the VDC.

5.7. Outlook: Measurement Program

With this setup for the electronic environment and the gas system and the CMS VDC prototype several tests and measurements have been done. There were four types of measurement with the VDCs which will be discussed in the following chapters:

1. **Development and test of the trigger system (Chap. 6)**

2. **Commissioning (Chap. 7)**: Tests of the prototype to determine its quality and preparing the automation of commissioning for the mass production of seven VDCs to get the characteristics of it and to determine optimal operating values:

   - tests of the high voltage robustness and the behavior of cathode and anode voltage and current
   - tests of the stability of pressure and temperature readout
   - tests of the gas tightness.

3. **Alignment of chamber parameters (Sec. 7.3):**

   - varying the threshold for the anode signals to determine its optimal value
   - taking data by varying the anode voltages to set an optimal anode voltage and to determine changes of the drift velocity.

4. **General measurements of the drift velocity under different conditions (Chap. 8):** This includes measurements at conditions expected at CERN. Those are measurements of the drift velocity in dependence of:

   - the electric field
   - the gas mixture
   - the gas pressure
   - the temperature
   - the anode voltage.

6. The Trigger System

Three types of trigger systems have been tested: One with two scintillators, one with a single scintillator and one with a scintillating fiber.

Requirements for the trigger system of the VDC:

- high efficiency for detection of the outcoming β-electrons

- fit into the rack for the VDC equipment at CERN

- same processing and transfer time for detection of electrons from both exit collimators

- low cost for detector and ancillary equipment

- long life time

- no requirement for maintains or easy maintainability

- match the small size of the VDC.

After a test with a setup with two scintillators (Sec. 6.2.3), each read out by one photomultiplier [Böh89], a new test with one scintillator read out by two photomultipliers (Sec. 6.2.4) followed. Trigger systems with photomultipliers require expensive photomultiplier tubes and high voltage supplies. There is a good reason to look for alternatives.

Silicon **P**hotoMultipliers are a new kind of photodiodes with interesting properties (Sec. 6.3.1). After tests of various configurations (Sec. 6.3), a setup with a scintillating fiber connected to two photodiodes (Sec. 6.3.3) was tested.

6.1. Scintillators for Triggering

An electron from a ^{90}Sr source comes through an exit collimator. This electron is used as a trigger (a start signal for a measurement). The time between the anode signal and the trigger is registered. Therefore an accurate timing is needed.

For fast and stable time measurements in the nanosecond region scintillators are best suited.

While traversing a scintillator a particle will deposit energy in the material. Some of this energy is emitted in form of light (wavelength $300\,\mathrm{nm}$ to $800\,\mathrm{nm}$) by the material (*scintillation light*). The amount of light depends on the energy that the particle deposits in the scintillator and the scintillation material. The scintillation material must be transparent for its own light emission.

Some part of the light is kept inside the scintillator by total internal reflection and reflection at surrounding material. The angle of total refraction is given by Snell's law:

$$\frac{sin\ \alpha}{sin\ \beta} = \frac{n_2}{n_1}. \tag{6.1}$$

$n_1 = c/c_1$ = refractive index of inner medium (scintillation material, light guide)
c_1 = speed of light in inner medium
α = angle in the inner medium
$n_2 = c/c_2$ = refractive index of outer medium (gen. air)
c_2 = speed of light in outer medium
β = angle in the outer medium

The condition for total reflexion is to have an angle α large enough that no β fulfill Equ. 6.1:

$$\sin \alpha > \frac{n_2}{n_1} \cdot max(\sin \beta) = \frac{n_2}{n_1} \tag{6.2}$$

Noise:
Detectors for scintillation light with high photon detection efficiencies ($> 20\,\%$) have high noise rates and hence for a single pulse one cannot distinguish whether it is noise or signal. The noise ("shot noise") is caused by the part of the detector which converts light signals into electrical signals.
Thus, one has to use more than one independent detector that can be hit by the scintillation light from one event simultaneously. Signals from an event reach the detector within a small time window but the noise of each detector is randomly distributed. The method to extract the signal in presence of noise in individual detectors is to require a *coincidence* of their signals within a certain time window.
With a discriminator one can send a digital pulse when the pulse amplitude is greater than a predefined threshold. With this some low amplitude noise or signals can be separated from the signals one is looking for.

Random coincidences:
Because of the finite time resolution of the electronics and the slightly different propagation times of the light to the detectors signals from an event do not arrive exactly at the same time. If two noise pulses in two detectors occur at same time interval this is called a *random coincidence.*

One can calculate the expected rate for a random coincidence for two detectors in the following way:
The probability P for an overlap with length Δt of two pulses with length l_1 and l_2 in the time (window) t is

$$P(signal_2|signal_1) = \frac{1}{t}(l_1 + l_2 - \Delta t). \tag{6.3}$$

So for the rate n_{12} of random coincidences one gets from the two rates n_1 and n_2

$$n_{12} = (n_1 \cdot n_2) \cdot (l_1 + l_2 - \Delta t) \tag{6.4}$$

E.g. for a minimum overlap for the coincidence modules [I3A82] of 0,5 ns [Hil07] and a minimal pulse length (given by the properties of the discriminators) of 5 ns two noise rates of 10 kHz lead to a random coincidence rate of $(10\,\mathrm{kHz})^2 \cdot (5 + 5 + 0{,}5)\,\mathrm{ns} = 1{,}05\,\mathrm{Hz}$.

Functionality of Plastic Scintillators:

One kind of organic scintillators are plastic scintillators. Plastic scintillators are very fast (decay times below 2 ns are possible). They are also unproblematic: not hygroscopic, stable, low cost, easy handling (cutting and milling), but lower light yield than in certain inorganic scintillators. An incoming β-particle loses energy in the detector by ionization (Sec. 4.1.2). The deposited energy of the particle is transformed to smaller values until a part reaches energies in the eV region. Then some electrons are exited into some vibration states of the first exited singlet state. This state decays mostly into excited vibration states by emitting *fluorescence light*. In this case the fluorescence light acts as scintillation light [Kle05] with a spectrum of wavelengths (Fig. 6.1).

A more detailed description can be found in Sec. A of the appendix.
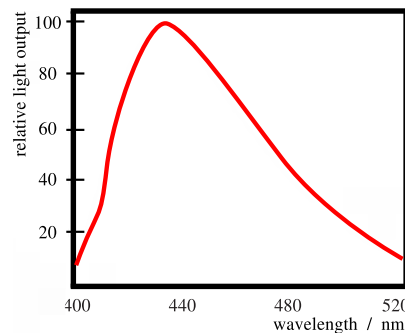
Figure 6.1.: *Emission spectrum of a BC416 scintillator (equal to N114 [Art06]). Peak wavelength: 434 nm, light output: 38 % of anthracene, decay time: 4,0 ns, pulse width (FWHM): 5,3 ns [BC05] .*

6.2. Trigger Systems with Photomultipliers (PMs)

6.2.1. Functionality of Photomultipliers

In photomultipliers incoming photons knock out electrons through the photo effect, and these electrons are multiplied by avalanches between electrodes (Fig. 6.2).

The scintillators or light guides are coupled to the window of the photomultiplier by optical gel or silicon pads. The window of the PM has to be transparent for the light which should be detected. Typical spectral sensitivities are 300 nm to 620 nm with a peak sensitivity of 420 nm. But there are also special devices with sensitivities ranging from 185 nm up to 1700 nm [Ham07]. Behind the window the light creates an electron by photo effect at the *photocathode*. The size of the photocathode defines the active area of a PM. Diameters for round photocathodes from 10 mm to 508 mm can be realized [Ham07].

For usually photomultiplier the probability that an incoming photon creates an electron per photo effect at the cathode, called *quantum efficiency* (QE), is around 20 % (QEs as high as 42 % for a new model from Hamamatsu have been achieved).

The inside of the PM is evacuated to avoid absorption of the created free electrons. The electrons from the cathode, the *photoelectrons*, are attracted by the electric field inside the PM created by the cathode, the anode and the electrodes, called *dynodes*. Between the anode and the first dynode (as seen from the anode) there is a potential difference. At each dynode each incoming electron initiates several new electrons. So the amount of free charge is multiplied at each

dynode. Photomultipliers reach a gain, the ratio between the number of electrons which reached the anode and the number of produced photoelectrons, of 10^4 to $3 \cdot 10^8$ [Ham07].

The electric fields should be designed in a way that the fluctuations of the travel time of the electrons from different regions of the photocathode are minimal. A time jitter between a fraction of a nanosecond and a few nanoseconds are typical [Ham07].

The signal at the anode is read out through a RC-circuit (and an amplifier). So signals with amplitudes of more than $200\,\text{mV}$ are obtained from a photomultiplier tube.

The pulse height spectrum follows a Poisson distribution because one has many events and the probability of a photoelectron is low and constant. The single photon noise rates of PMs are in a region from $20\,\text{kHz}$ down to $10\,\text{Hz}$ (low sensitivity). With a discriminator one can set the threshold for signals with 1, 2, 3, ... photoelectrons.
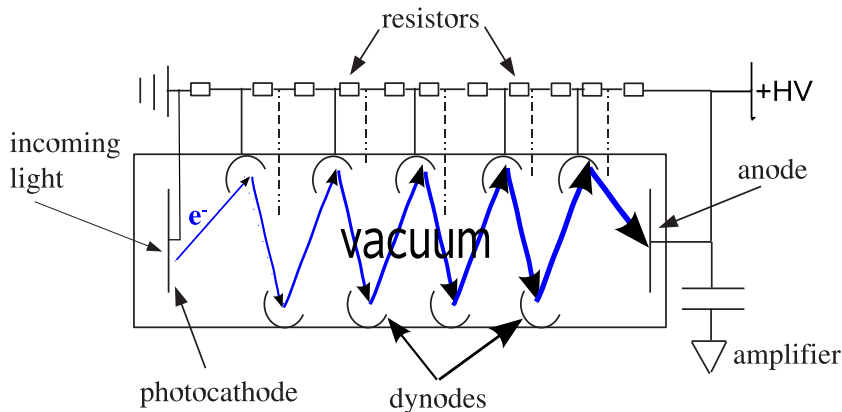
Figure 6.2.: *Functionality of a photomultiplier.*

6.2.2. Adjustment of Photomultipliers

All photomultipliers, even from the same production line, have different properties. Thus, every photomultiplier has to be adjusted individually. For the use as trigger system only the signal rate has to be optimized. The energy spectrum of the incoming particles is not relevant.

For a photomultiplier based trigger system there are three parameters to be adjusted for each PM: supply voltage, discrimination threshold and timing of the signals (to produce a coincidence).

Each photomultiplier has been tested following the procedure which is described below. The adjustment, done empirically, is made to obtain a high trigger rate with a small contribution from accidental coincidences, while ensuring a long life time of the PMs [Alt06].

Adjustment of supply voltage:
Often the value of the voltage given by the manufacturer is not optimal.

Two photomultipliers (PM1 and PM2) are connected to scintillators which are traversed by a beam of β-particles (as done in Sec. 6.2.3 and 6.2.4). The β-particles were generated by a ^{90}Sr-source inside the probeholder (Fig. 6.5) or the VDC. One sets one of the PMs to a fixed estimated optimal voltage (e.g. around $2000\,\text{V}$). Then one can take a high voltage curve by measurements at different supply voltage values. For this, the rates of PM1 and the coincidences of both PMs are measured. One will find out that the rate of the PM1 (and PM2) increases exponentially with the supply voltage. The coincidence rate increases linearly with the voltage

until it reaches a plateau. The begin of this plateau is taken as current value for the operation voltage.

In the following a high voltage curve for PM2 is taken in the same way. So one gets the optimal supply voltage for PM2. Then one can make one iteration step by redoing the first step with the optimized value for PM2.

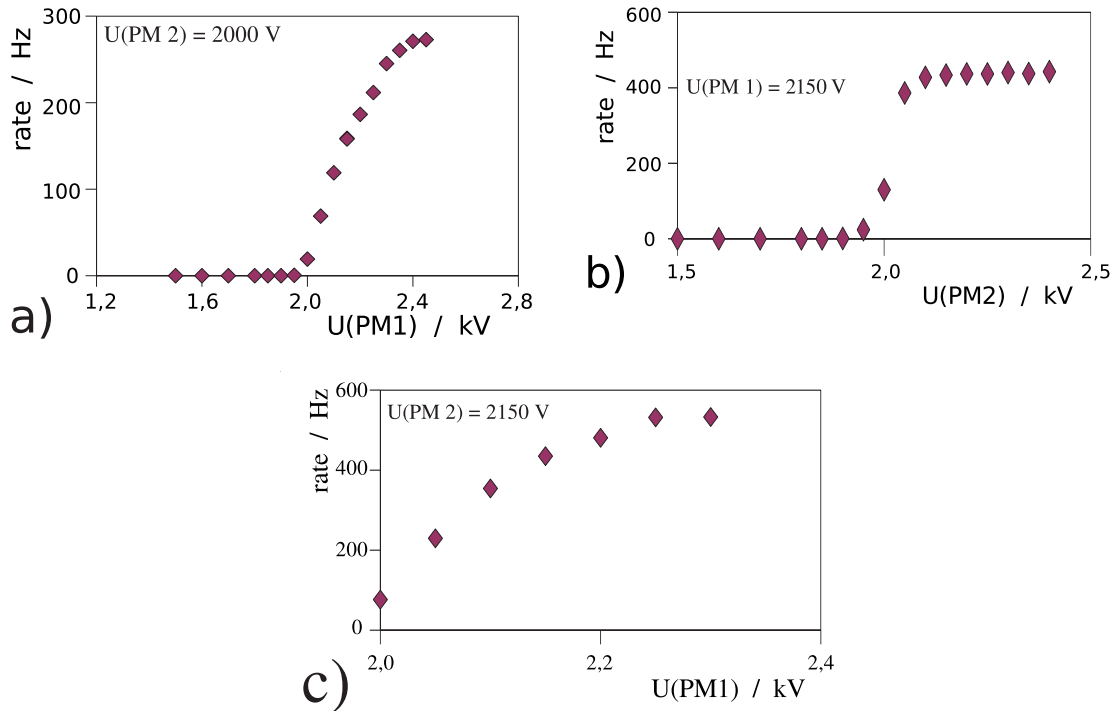For the setup of Sec. 6.2.3 the corresponding HV curves are shown in Fig. 6.3.

Figure 6.3.: *Adjustments of two photomultipliers (PM1 and PM2) connected to two scintillators (Sec. 6.2.3) with β-rays from probeholder (Fig. 6.5) loaded with two radioactive sources:*
a) fixed voltage for PM2, measurement of coincidence rate as a function of the voltage of PM1
b) fixed voltage for PM1 (obtained from a)), measurement of coincidence rate as a function of the voltage of PM2
c) fixed voltage for PM2 (obtained from b)), measurement of coincidence rate as a function of the voltage of PM1.
The found optimal voltages are: PM1: 2,25 kV, PM2: 2,1 kV.

Adjustment of discriminator threshold:

As said in Sec. 6.2.1 the pulse height of the PM signal is proportional to the number of incident photons. In addition there is noise from the electronics, e.g. thermal noise which is usually smaller in amplitude than the signal from one photon.

Since a suitable multi channel analyzer was not available the threshold could not be adjusted by analyzing the spectrum of the PMs. At the oscilloscope one can see huge peaks and a small underground e.g. caused by electronic noise. Setting the threshold between those values all pulses without any pulses caught by electronic noise are captured.

Adjustment of timing for the signals:

To ensure that the signals have enough overlap to make a coincidence, the digital PM signals must be timed both in length and in their delay. The pulse length, set at the discriminator output, should not be shorter than the time fluctuations of the PM signals. One strategy is that one makes one signal (from the more stable PM) long (30 ns) and the second one short (5 ns to 10 ns). The signals of the used photomultipliers have a measured spread smaller than 4 ns. This matches the minimal pulse width required by the coincidence units well. By giving a delay of 10 ns to the second signal it can be placed in the center of the first one.

6.2.3. Configuration with Two Scintillators
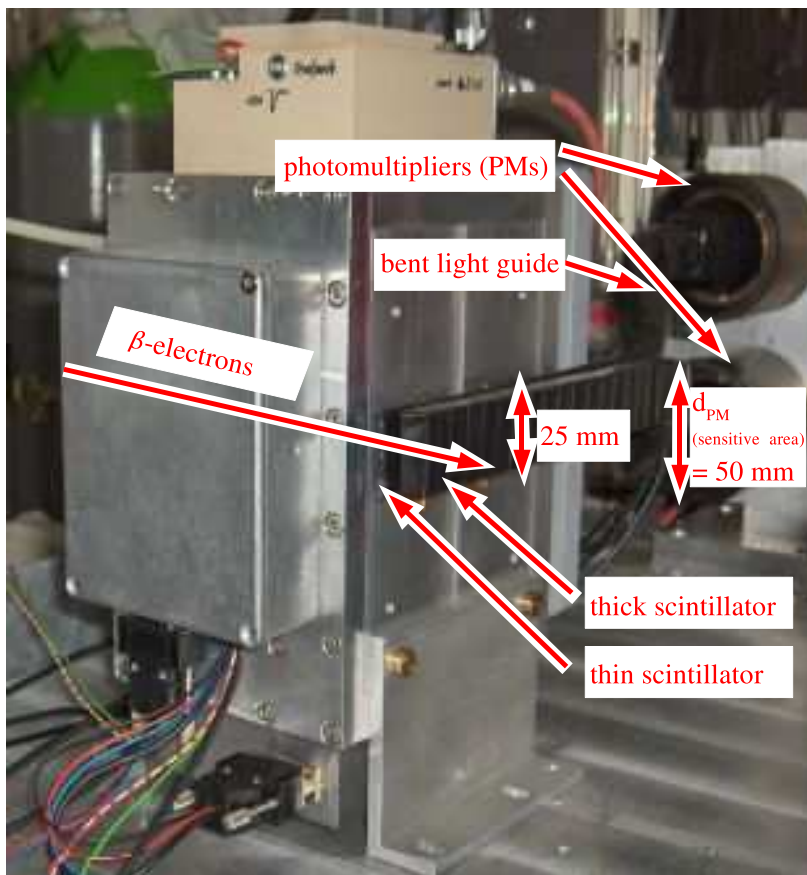
Figure 6.4.: *The VDC with a trigger configuration of a thin (2 mm thickness) and a thick (10 mm thickness) scintillator in one black tape, each read out by one PM.*

Two scintillators (BC416, 150mm long) with a thicknesses of 10 mm and 2 mm and a height of 25 mm are each connected by a light guide to a photomultiplier at the same side. The BC 416 scintillator material emits light with a mean wavelength of 434 nm (Fig. 6.1) [Saint06].

The advantage of this configuration is its modest space requirement. By adding light guides the two large photomultipliers can be placed behind the chamber so that there is more space beside chamber.

The main disadvantage of this configuration is absorption. The electrons have to travel the first scintillator with a thickness of 2 mm and its sheathing (aluminum foil and black adhesive tape). Thus, there is an absorption of the low-E electrons precluding its detection on the second

scintillator.

To minimize this effect both scintillators have been packed in one common sheathing of black adhesive tape, while still being separated by an aluminum foil.

An additional disadvantage is the fragility of the thin scintillator which requires a more complicated mechanical handling.
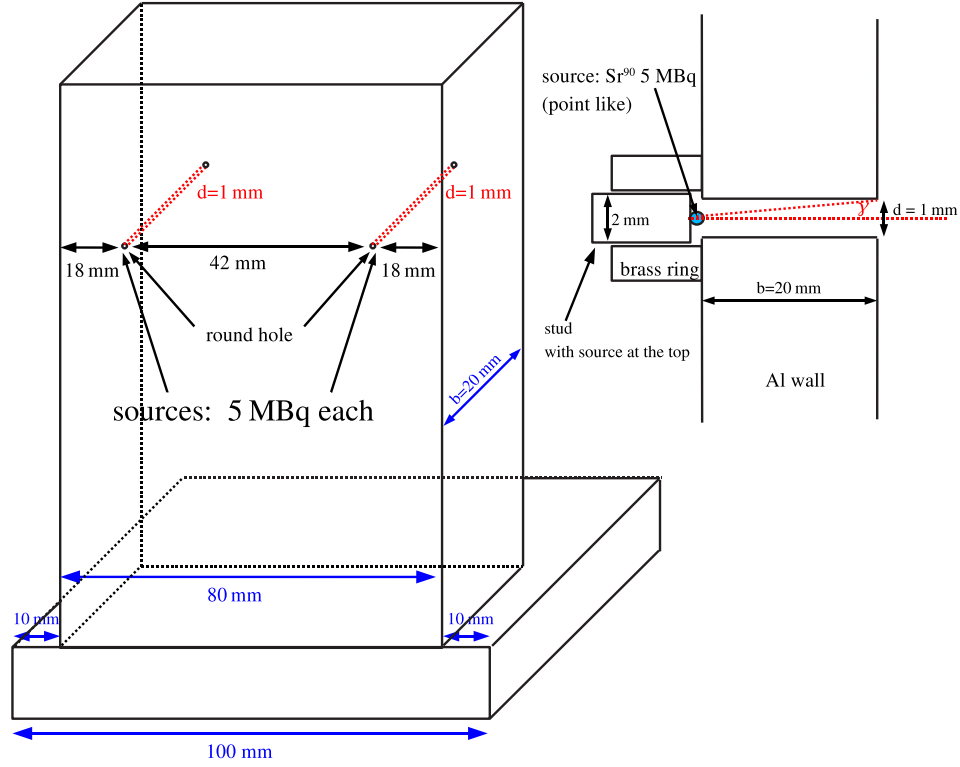

Figure 6.5.: *Holder for sources to test the trigger system: When equipped with one 5 MBq source, the nominal rate of β-particles at the outlet of the 1 mm collimator is about 780 Hz.*

To collect statistics in a shorter time, measurements for testing the trigger system have been made without the chamber. Instead of that a simple aluminum plate with a hole of 1 mm diameter as a collimator was placed directly in front of the scintillator. With the geometry of this collimator the electron beam rate can be calculated: The opening angle γ at the probe is (Fig.6.5) defined as

$$\tan\gamma = \frac{d}{2b}. \tag{6.5}$$

The solid angle element is

$$\Omega_1 = \pi\gamma^2 = \pi\left(\arctan\frac{d}{2b}\right)^2 \tag{6.6}$$

and the fraction of the total solid angle amounts to

$$\frac{\Theta_1}{\Theta_{total}} = \frac{\Omega_1}{4\pi} = \frac{\gamma^2}{4} = \frac{1}{4}\left(\arctan\frac{d}{2b}\right)^2 \approx \frac{d^2}{16\,b^2}. \tag{6.7}$$

At the given geometry: $\gamma = 25$ mrad $(= 1,4°)$ and $\Omega_1 = 2$ msr.

For 5 MBq sources and no absorption in the source encasement and air, electrons with a rate of

781 Hz should reach the scintillator directly behind the Al wall. But a fraction of the electrons travel through the Al wall although their mean range is smaller then the thickness of it. This is possible because the energy loss follows a distribution - the *Landau distribution* - and so some electrons lose less energy than the mean energy loss.

device	optimal voltage / V	threshold / mV	digital pulse length / ns	delay / ns	rate with probe holder / Hz	rate with VDC / Hz	noise / Hz
PM1	2250	300	30	0	2820	NA	NA
PM2	2100	100	10	10	1520	NA	NA
coincidence	-	-	-	-	532	30	0,5

Table 6.1.: *Parameter values for the PMs as obtained from the adjustment procedure and observed rates in a configuration with two scintillators. PM1 is connected to a scintillator with 2 mm mm thickness and PM2 to one with 10 mm thickness.*

After adjusting the photomultipliers and eliminating possible light leaks in the scintillator wrapping, the coincidence rate as a function of the distance between the radioactive source and the photomultipliers has been measured (Tab. 6.2) using the probeholder loaded with one radioactive source. This is done in order to determine the origin of the different amount of statistics within each peak of the drift time spectrum: The second peak in the drift time spectra (taken with this trigger configuration) is always more prominent than the first one. This could be caused by a higher trigger efficiency for the second β-beam. This higher efficiency can be explained by the fact that the distance to the PMs is smaller, which leads to a larger amount of light reaching the PMs.

Following Fig. 6.6 the rate can be approximated as a linear function of the distance between the point where the β-electrons enter the scintillators and the photomultipliers. Thus, the statistic inside the peaks of the drift time spectrum is influenced by the distance of the outlet slits to the PMs. This has no influence to the drift velocity, but the different runtimes of the light to the PMs has. The drift time has to be corrected for the runtime of the light between the outlet slits ($\approx 42\,\text{mm} \cdot n/c = 0{,}22\,\text{ns}$, compare to Equ. 6.8).
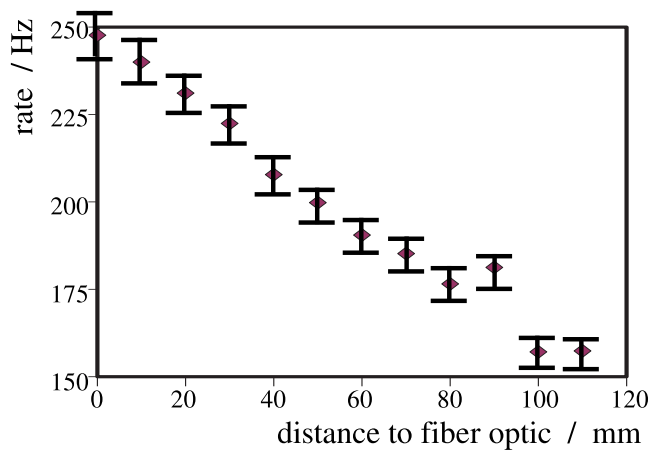

Figure 6.6.: *Rate of coincidences as a function of the distance of the β-electron in the probeholder to the PMs for a configuration with two scintillators. The rate seems to be approximately a linear function of the distance to the PMs. The error bars are statistical errors ($\propto \sqrt{rate}$.)*

distance to light guide / mm	rate PM at scintillator 1 (thin scintillator) / Hz	rate PM at scintillator 2 (thick scintillator) / Hz	rate coincidences / Hz
0	22093	1568	248
10	18784	1430	240
20	17865	1389	231
30	19087	1396	222
40	17916	1348	208
50	19075	1319	200
60	16802	1265	191
70	17979	1240	185
80	17720	1193	177
90	19208	1188	181
100	18133	1092	157
110	19058	1041	157

Table 6.2.: *Coincidence rate as a function of the variation in distance of one radioactive source (inside the probeholder) to the light detectors: Because the outlet of the two β-beams have different distances to the PMs the trigger rate (=coincidence rate) might be influenced by this distance.*

In the assumed center of the scintillator a coincidence rate of 200 Hz is measured which is around 1/4 of the estimated raw particle rate (Equ. 6.7). This discrepancy is caused by absorption in the tapping and mainly by absorption in the first scintillator of low energy β-electrons (Electrons with energies below 1,2 MeV can on average not pass it [Sas90].). Looking at the rates in Tab. 6.2 one sees that the rate for the PM connected to the thin scintillator is more than 10 times larger than the rate for the PM connected to the thick scintillator. Both rates include the noise, for which the value for the PM connected to the thick scintillator can be estimated by subtracting the coincidence rates from the single rates.

The probability distribution for emitting particles of the radioactive source is a Poisson distribution and also the detection probability of the PM is a Poisson distribution. For a large number of events this becomes a Gaussian distribution [Cow98]. Thus, the standard deviation is the square root of the value for the rate. An additional effect influencing the error calculation could be a non constant supply voltage.

This trigger configuration used with the VDC deliverers a coincidence rate of around 30 Hz (with two sources) and a noise rate of 0,5 Hz. The significant further rate reduction is caused by the geometry of the VDC and its collimators. The noise has been determined by measurements without sources.

The measured trigger rate of 30 Hz is very low to the expected 430 Hz [Alt06] of β-electrons leaving the VDC. Because the drift velocity should be measurement in a time as short as possible the trigger rate should be improved.

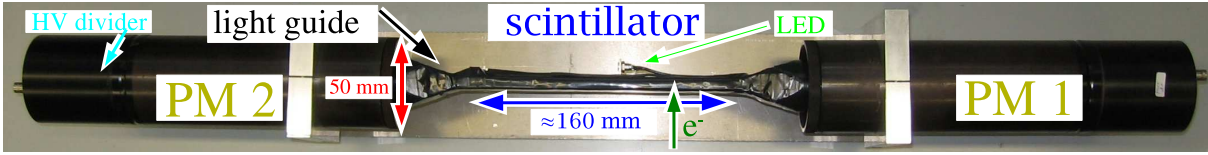## 6.2.4. Configuration with One Scintillator

Figure 6.7.: *Configuration with one scintillator connected to two PMs.*

To reduce absorption losses and to use a simple mechanical construction, a configuration with one 10 mm scintillator connected to two PMs has been created for tests in Aachen. Since here a different geometry for light collection and different PMs have been used, the PM parameters (Sec. 6.2.2) had to be adjusted again (Tab. 6.3). Because the signals from the PMs, which are used for this configuration, are very stable in time, no delay was used and the digital pulse lengths have been set as short as possible to reduce random coincidences. The timing of the signal was checked using an oscilloscope [Tek96]. In the average mode (triggering on PM1) one can see that the amount of signals from PM2 outside the pulses from PM1 is very small (noise pulses).

PM	optimal voltage in V	threshold in mV	digital pulse length in ns	delay in ns	rate with probe holder in Hz	rate with VDC in Hz	noise in Hz
1	2100	300	5	0	7000	NA	NA
2	2250	300	5	0	5000	NA	NA
coincidence	-	-	-	-	3500	60	3.0

Table 6.3.: *Parameter settings and observed rates for the PMs used in the configuration with one common scintillator.*

Assuming that because of the missing absorption effect of the thin scintillator also β-electrons with kinetic energies below 1,2 MeV can cause a coincidence, the coincidence rate should be improved by a factor larger than 2. The exact value is difficult to calculate because for this the minimal energy deposit in the scintillator which can create enough light to cause a signal at the PMs has to be known.

The measured coincidence rates (Tab. 6.3 for measurements with the probeholder are seven times higher (3500 Hz to 500 Hz) than the rates of the previous configuration. The measured coincidence rates with the VDC are two times larger (60 Hz to 30 Hz).

Since the distance from one outlet slit of the VDC to the farthest PM is equal for this constellation there should be no effect for the rate as in the previous constellation. Nevertheless, there are effects which can be seen in the drift time spectrum when moving the trigger system. Thus, the effect of the distance to the PMs to the rate has been measured again. The result of a measurement of the rate for different positions of the sources with respect to the scintillator is shown in Tab. 6.4 and Fig. 6.8 and 6.9.

The sharp drop of the rate at 80 mm (Fig. 6.8) indicates the end of the scintillator.

The rate of each PM decreases with the distance of the source to it, but the maximum of the coincidence rate is not in the center of the scintillator. The reason for it could be a higher

efficiency of PM 1. Placing the VDC in the center of the scintillator will lead to the highest trigger rates.

position relative to center of scintillator / mm	rate PM1 / Hz	PM2 / Hz	rate of coincidence / Hz	rate of expected random coincidences / Hz	meas. delay PM 2 to PM 1 / ns
-80	200,52	316,34	$144,88 \pm 1,20$	0,00	1,52
-70	256,52	351,78	$187,19 \pm 1,39$	0,00	1,48
-60	346,94	476,01	$257,20 \pm 1,60$	0,00	1,48
-60	478,64	637,35	$356,71 \pm 1,89$	0,01	1,28
-40	690,91	903,54	$520,75 \pm 2,28$	0,02	1,40
-30	1068,79	1374,54	$811,69 \pm 2,85$	0,04	1,32
-20	4420,87	4612,94	$2845,63 \pm 5,33$	0,61	1,16
-20	4400,38	4606,97	$2840,54 \pm 5,33$	0,61	1,16
-20	4386,24	1642,57	$2834,69 \pm 5,32$	0,22	1,04
-10	4711,91	4818,00	$3037,54 \pm 5,51$	0,68	1,28
0	4944,34	4928,39	$3157,74 \pm 5,62$	0,73	1,44
10	5162,60	4962,60	$3246,94 \pm 5,70$	0,77	1,56
20	5391,40	5003,24	$3346,02 \pm 5,78$	0,81	1,84
30	5556,69	4957,23	$3380,20 \pm 5,81$	0,83	2,00
30	5556,80	4974,62	$3380,70 \pm 5,81$	0,83	2,04
40	5689,51	4854,14	$3367,42 \pm 5,80$	0,83	2,24
50	5769,39	4678,52	$3304,44 \pm 5,75$	0,81	2,44
60	5733,39	4420,27	$3151,64 \pm 5,61$	0,76	2,68
70	5560,74	3970,40	$2887,48 \pm 5,37$	0,66	3,00
80	1286,68	1115,05	$821,42 \pm 2,87$	0,04	2,88

Table 6.4.: *Counting rates of two PMs connected to one common scintillator as a function the position of a radioactive source using the probeholder loaded with two sources. The expected random coincidence rate has been calculated using Equ. 6.4.*

Figure 6.8.: *Counting rates of two PMs connected to one 160 mm long scintillator as a function of the position relative to the center of the scintillator, for one radioactive source inside the probeholder.*

The time difference between both PMs has been measured with an oscilloscope [Tek96] (Fig. 6.9). The averages values (average over a few 1000 events) varies strongly (see the values for $-20\,\text{mm}$). The light travel time in the whole scintillator approximating an angle of $45°$ to the surface for the light beam should be around

$$t = \sqrt{2} \cdot \frac{s}{c} \cdot n \approx \sqrt{2} \cdot \frac{160\,\text{mm}}{3 \cdot 10^8\,\frac{\text{m}}{\text{s}}} \cdot n \approx \sqrt{2} \cdot 0{,}5\,\text{ns} \approx n \cdot 0{,}8\,\text{ns}. \tag{6.8}$$

The offset of more than $1\,\text{ns}$ could result from a different transit time in the PMs or from the electronics. The asymmetry for the travel time to PM 2 could be caused by asymmetries like a small region with bad scintillator material that produces a longer optical path for the light and by variations of the PM pulse shape for different amounts of light.
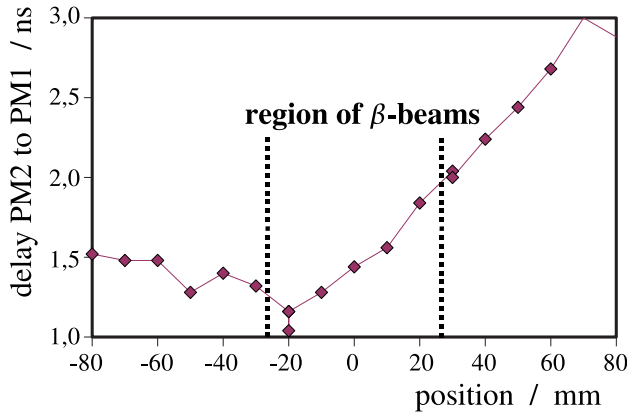
Figure 6.9.: *Time differences between two PMs connected to one scintillator as a function of the position relative to the center of the scintillator, for one radioactive source inside the probeholder.*

This thesis can be reinforced by looking at the rate measured with the VDC:
The value of around $60\,\text{Hz}$ (Tab. 6.3) in the center of the scintillator is very instable because small movements of the scintillator relative to the chamber produce a great variation in the rate. This can not be explained by the measurement shown above because the effect is much bigger. A movement of a few millimeters changes the rate for one source up to a factor 2. A possible explanation could also be local damages in the crystals of the scintillator (the material is quite old.). The value of the runtime fluctuation is used for the estimation of the error of the drift velocity (Sec. 9.4).

Finally the second configurations for the trigger system should be used because it leads to a higher trigger efficiency and because of the symmetry of the constellation systematic error are reduced (see Sec. 9.4).

6.3. Trigger systems with Silicon Photomultipliers (SiPMs)

The first setup was a small piece of scintillator ($17\,\text{mm} \times 10\,\text{mm} \times 70\,\text{mm}$) read out with four **Si**licon **P**hoto **M**ultipliers (type SSPM-050701BE-TO18 from Photonique [Pho06]). Because of mechanical instabilities no useful results about the applicability where obtained from this setup. Probably because only a small fraction of the front face was covered by the detectors, the efficiency would have been too low anyway. Nevertheless some experience with cooling by Peltier elements was obtained. Cooling SiPMs will dramatically (factor 2 every $10\,\text{K}$) reduce the noise rate [Ham07].

Because of the inflexibility another setup could not be used for further useful measurements. A further result was that large holders of plastic around a SiPM will cause a bad long time stability.

6.3.1. Functionality of Photodiodes
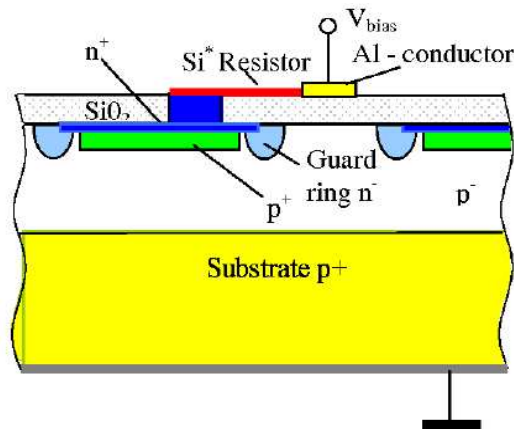
Figure 6.10.: *Principle of operation of Solid State Photomultipliers [Buz01]: Light creates electron hole pairs in the SiO$_2$-layer. The electrons drift in the electric field until they reach the Geiger region of the field where they can travel from the n^--doped region into the p^+-doped region.*

SiPMs are light detectors based on semiconductor technology. They contain many pixels (Fig. 6.10) each working as an avalanche photodiode in Geiger mode. That means that each pixel creates a pulse with an amplitude which is independent from the amount of light hitting it. The output pulse amplitude of the whole SiPM is the sum of the pulse amplitudes of all pixels. The output pulse of a SiPM is electronically emitted in parallel operation of all pixels. The photon detection efficiency of the SiPM depends on several factors:

- the fill factor: Between all the pixels there is some insensitive surface. Using large pixel sizes up to $100\,\mu\text{m} \times 100\,\mu\text{m}$, a fill factor up to $78{,}5\,\%$ for a Hamamatsu S10362-11-100 [Ham07] can be reached.

- quantum efficiency: Photons produce electron-hole pairs with high quantum efficiency (about $85\,\%$) in a reversely biased P-N junction.

- avalanche efficiency: Not all electron-hole pairs leads to a pixel breakdown (producing an enhanced signal).

Multiplying these items the photon detection efficiency can reach 65 % for a Hamamatsu S10362-11-100 [Ham07].

The noise rate depends on the signal amplitude one is looking at, since the probability that a certain number of pixels create pulses simultaneously decreases with their number. The noise rate drops as a Poisson distribution for a rising threshold [Rop07]. A measurement using a FADC[1] and software by [Raab07] (Sec. 6.3.3) determines a factor of to 3 to 7 for the drop of the noise rate when increasing the threshold by a factor 2.

6.3.2. Scintillating Fibers

A typical round multi clad scintillating fiber

total internal reflection
at first/second cladding interface

lost photon

trapping efficiency:

5,6 % · 2π str

72,4°

27,4°

47,4°

scintillating core n = 1,60
second cladding n = 1,42
first cladding n = 1,49
optional extra mural absorber (EMA)

traversing particle
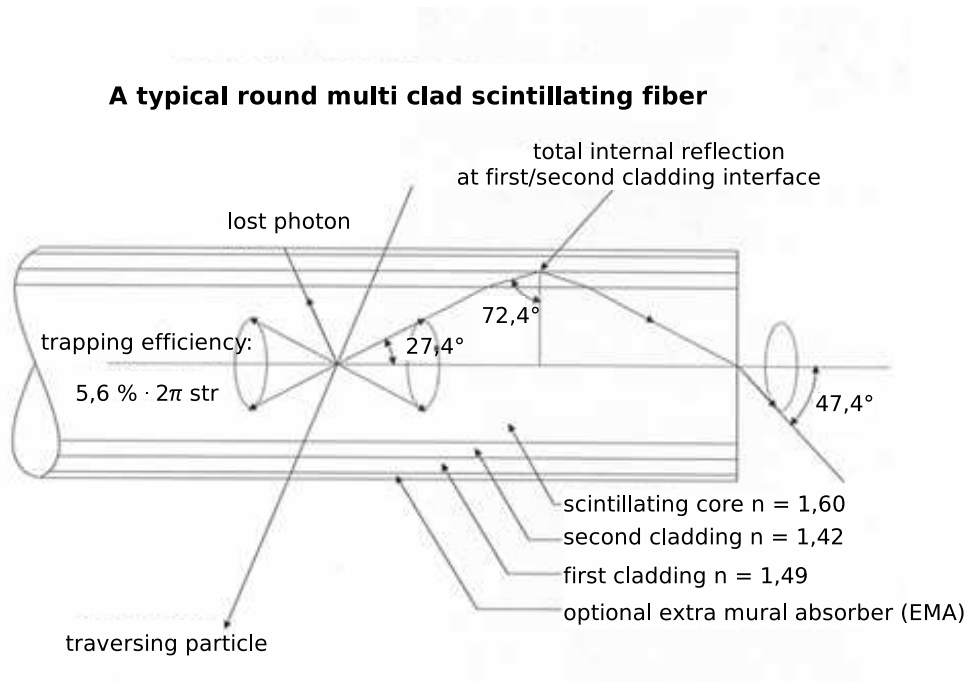
Figure 6.11.: *Light trapping in a scintillating fiber [Saint06].*

A scintillating fiber is a round or rectangular thin scintillator. The scintillator is coated by one or two layers of material with a lower refractive index, the *cladding* (Fig. 6.11). The interface between the scintillating material and the cladding (and between the claddings) is defined very well. It is much more insensitive to effects of dust, diffusion and oxidation. The amount of light which is kept inside the fiber is larger than without cladding [Rop07]. Two layers of cladding will lead to a factor of 1,5 for the amount of light inside the fiber compared to a fiber with a single cladding [Saint06].

---

[1]**F**ast **A**nalog-to-**D**igital **C**onverter

6.3.3. Configuration with an Optical Fiber in "U"-'Form
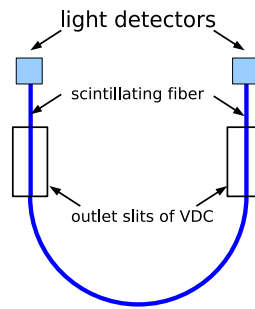
Figure 6.12.: *The principle of a trigger configuration using a scintillating fiber [Rei07].*

For detecting the β-particles from both outlet slits with the same light detectors and to cover a large area of the scintillators with light detectors, (a) scintillating fiber(s) in "U"-form (Fig. 6.12) are the only solution [Rei07].

Since SiPMs with such a high photo detection efficiency above 40 % for blue or green light are avaible, a first test has been done by using Hamamatsu S10362-11-100 [Ham07] MPPCs[2] of $1\,\text{mm} \times 1\,\text{mm}$ active surface matching the scintillating fiber, a $1\,\text{mm} \times 1\,\text{mm}$ BC-12 [Saint06] with multicladding. The setup (Fig. 6.15 and 6.13) was designed to be very flexible. Therefore a modular setup was chosen, i.e. the setup is subdivided into a box and a block. The box contains:

- holders for the SiPMs

- small blocks which can be pressed against the holders. Through a disk it also presses the SiPM against the fixed scintillating fiber.

- a plastic part where the holders are embedded, for a thermal insulation from the box and the remaining content of the box

- a board (Fig. C.2 of the appendix), preamplifiers and filters for the supply voltages

- connectors for supply voltage and signal output.

The block positions the fiber WRT to the outlet slits at the chamber. For the distance between the fibers at the positions of the VDC outlet slits the full precision of the CNC machine is used, because this distance defines the drift velocity. The block and the box are connected by some plastic parts. The fiber is led through some cylinders of plastic in the space between the block and the box. Bending the fiber to an "S" between the position of the slits and the cylinder allows to place the fiber close to the VDC.

Because of the modular design it is possible to replace some parts without a redesign of the whole setup, e.g. for replacing the SiPM by some with other dimensions only the SiPM holder (Fig. 6.15) have to be replaced, and for other fibers the fiber positioning block has to be replaced. The design permits to implement active cooling. Integrating peltier elements into the cover of the box will allow to cool the SiPM holders. The isolator around the holders is a first barrier for heat conduction. The box can also be insulated. Because of the separation between box and block, only the box has to be further insulated. The heat conduction to the VDC is reduced

---

[2]**M**ulti **P**ixel **P**hoton **C**ounter

because of the distance between box and VDC. To prevent creation of ice inside the box, which could affect the electronics, the cover can contain a rubber seal for gas tightness of the box. Incoming humidity can then be absorbed by a drying agent.

First results:

A first test of the system mounted on the VDC gave a signal rate of $(15{,}0 \pm 0{,}5)\,\text{Hz}$ at a noise rate of $(8{,}0 \pm 0{,}5)\,\text{Hz}$. Calibration of the threshold and of the SiPM voltage could improve this value.

A big handicap of this test is the bending of the fiber. Although is was warmed before bending, the cladding has been damaged at some places, which could lead to a large loss of light. For the next test the fiber bending has to be improved and the form of the block has to be modified. The measured rate indicates that a compact trigger system using scintillating fiber and SiPMs can be realized. For the final setup probably a $2\,\text{mm} \times 2\,\text{mm}$ fiber or a pack of $1\,\text{mm} \times 1\,\text{mm}$ fibers, which is more easily to bend, will be used to cover the whole area of the outlet slit of the VDC. Therefore $2\,\text{mm} \times 2\,\text{mm}$ SiPMs from Hamamatsu should be used because at the moment they have the very best properties (low noise rate, high photon detection efficiency) for the use at the VDC.
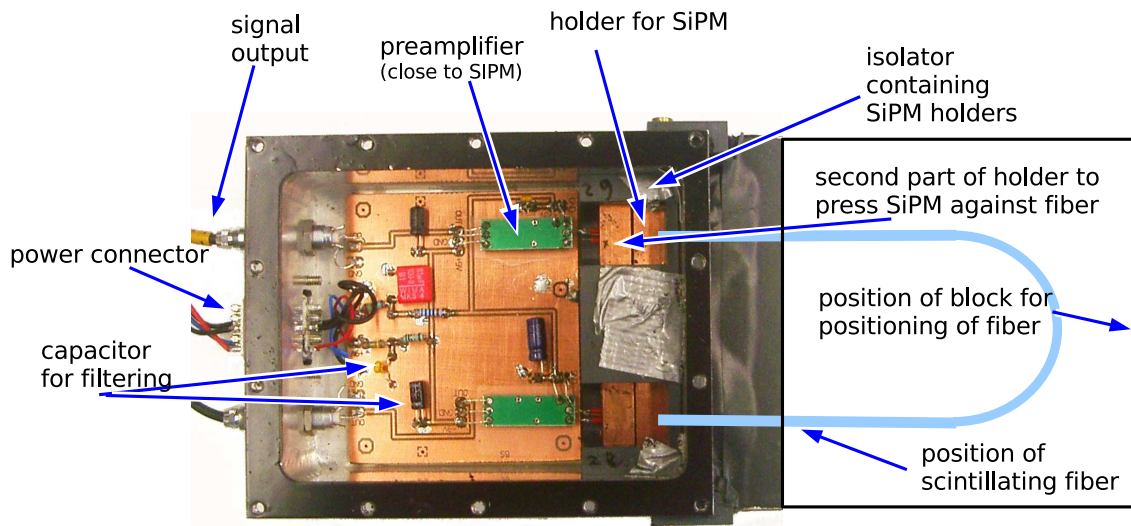
Figure 6.13.: *The setup with a $1\,\text{mm} \times 1\,\text{mm}$ scintillating fiber in "U"-form connected to two SiPMs. (The block for positioning the fiber is missing.)*
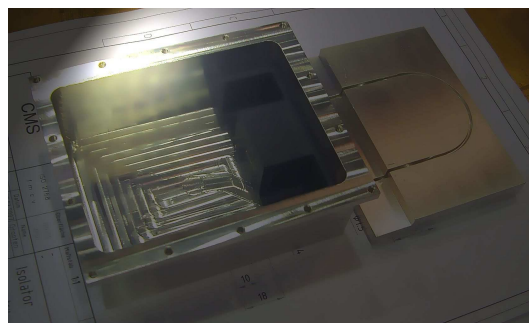
Figure 6.14.: *The bent fiber setup. At the left one sees the (empty) box containing the insulator and on the right the block for positioning the scintillating fiber. The groove which has been milled into a block of aluminum is still visible at this phase of assembly.*
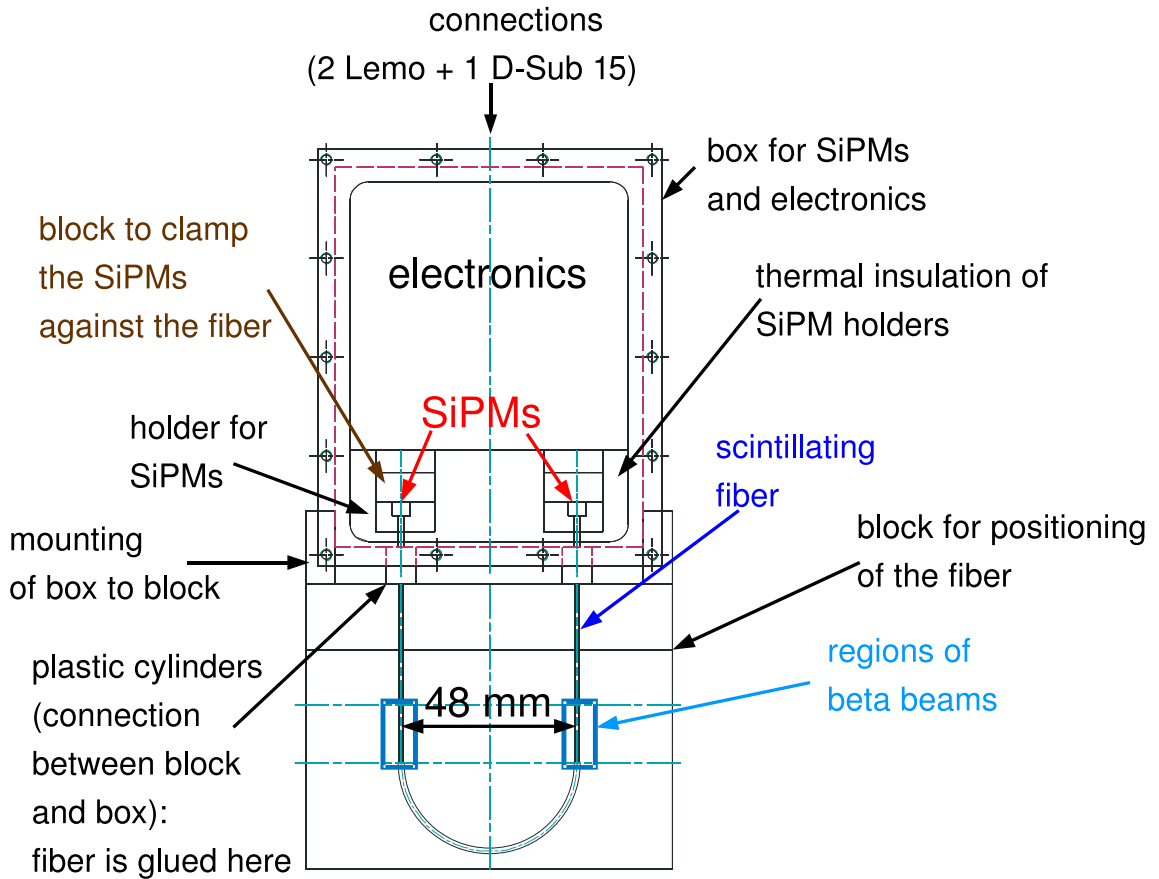
Figure 6.15.: *The mechanical setup of the "U"-form fiber setup [Gro06, Rei07].*

Measurements of the pulse height spectra:

In further measurements the number of photons which have to arrive at the SiPMs so that the threshold can set to a value where the noise rate is small enough has been determined.

Assuming an untriggered VDC anode rate of about $200 \, \text{kHz}$ (Fig. 7.8) and a trigger window of $2 \, \mu\text{s}$, a random trigger of $150 \, \text{Hz}$ would lead to a readout rate of $60 \, \text{Hz}$ for the anode pulses $(200 \, \text{kHz} \cdot 2 \, \mu\text{s} \cdot 120 \, \text{Hz} = 60 \, \text{Hz})$. This is the trigger rate using photomultipliers. The value of $150 \, \text{Hz}$ should be the maximum allowed noise rate of the trigger [Rei07].

A FADC with software from [Raab07] was used to measure the pulse height spectra of the two (number 28 and 29) SIPMs from Hamamatsu. The FADC works with $400 \, \text{MHz}$ and has a resolution of 8 bit for a range of the pulse height of $0 \, \text{V}$ to $-500 \, \text{V}$. To calibrate the zero point of the FADC data was taken without connecting anything to the FADC (left part of Fig. 6.16. The measured offset is $156{,}5 \, \text{mV}$. The characteristic of the electronical noise is shown in the right part of Fig. 6.16. It was measured by connecting the output of SiPM 28 to the FADC with switched on preamplifier but without applying voltage to the SiPMs. The FADC was random trigger with $20 \, \text{Hz}$ and a gate length of $100 \, \text{ns}$. Inside the gate the maximum amplitude has been determined.

The amount of pulses larger than $5 \, \text{mV}$ is very small and will not influence measurements at high thresholds.
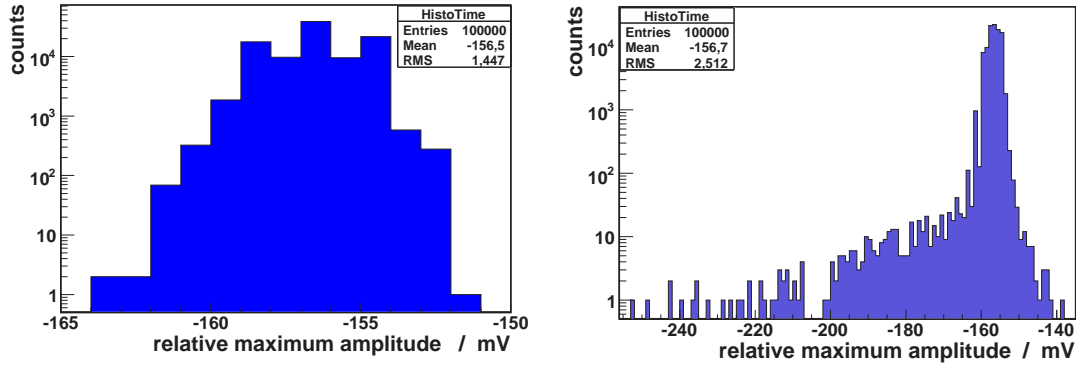
Figure 6.16.: *Measurements of the baseline of the used FADC (left) to calculated the absolute ampli-
tudes. The pulse height spectrum (right) of one SiPM (28) connected to a preamplifier
(gain 50) is shown. The voltage for the SiPM was switched off. For both measurements
the FADC has been random triggered with a frequency of 20 Hz and a gate length of
100 ns.*

To calculate rate from the pulse height spectrum the pulse height spectrum of SIPM 28 has been
measured while the FADC was still random trigger with 20 Hz and a gate of 100 ns (Fig. 6.17).
From the total number of triggers $n_t = 100000$, the window width l_w and the number of signals
inside a certain region of the pulse height spectrum n_s the rate of those signals r_S can be
calculated:

$$r_S = \frac{n_S}{n_t * l_w}. \tag{6.9}$$

Using the measured offset (Fig. 6.16) the absolute pulse amplitude has been calculated.
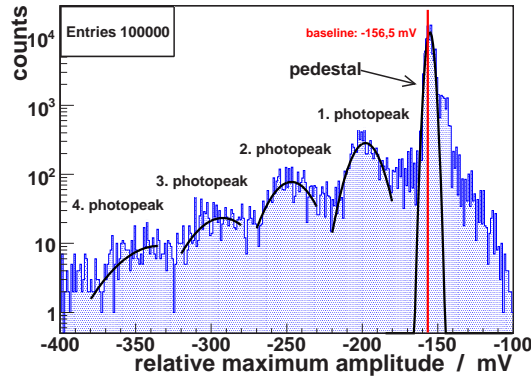
Figure 6.17.: *The pulse height spectrum of a SiPM (28) connected to a voltage of 70,0 V. A preamplifier
with a gain of 50 was used. The FADC was random triggered with 20 Hz. For each trigger
the maximum amplitude inside a trigger window of 100 ns was measured.*

For all measurements of the pulse height spectrum a supply voltage of 70,0 V was applied to the
SIPMs. In Fig. 6.17 one can see a large pedestal on the right corresponding to the electronical
noise (see right part of Fig. 6.16) and four peaks with increasing amplitude. These peaks belong
to the cases when one, two, three or four pixel fired at the same time, called photopeaks (of the
noise). By fitting a gaussian to them their position can be estimated. (Their exact structure
of the pulse height spectrum is more complicate [Rop07].) By summarizing the entries left

number of SiPM	photopeak		peak width	noise rate
	number	position		
		/ mV	/ mV	/ kHz
28	1	-41	9	800
29	1	-34	15	400
28	2	-90	13	300
29	2	-74	22	90
28	3	-136	18	100
29	3	-114	30	20
28	4	-180	24	20
29	4	-164	35	5

Table 6.5.: *The positions of the photopeaks and the noise rates (at room temperature) of the two (number 28 and 29) SiPMs (type S10362-11-100 from Hamamatsu) at a supply voltage of 70,0 V.*

from the peaks the noise rate for a threshold corresponding to the photopeaks can be estimated (Tab. 6.5).
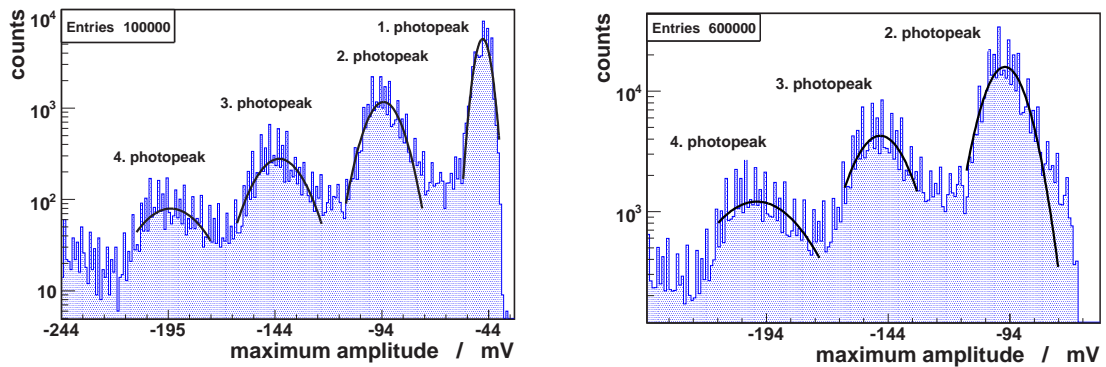
Figure 6.18.: *The pulse height spectrum of a SiPM (28) connected to a voltage of 70,0 V. A preamplifier with a gain of 50 was used. The FADC was triggered by signals from a discriminator connected to the SiPM with a threshold of 45 mV (left) and 75 mV (right). For each trigger the maximum amplitude inside a trigger window of 100 ns was measured.*

By triggering the FADC by a discriminator which is also connected to the SiPM (by a "Fan-In-Fan-Out unit") the pulse height spectrum above a certain threshold has been measured (Fig. 6.18) where the photopeaks can be seen easier because of more statistics.

From Fig. 6.17 and a similar measurements for SiPM 29 the noise rates (Tab. 6.5) has been estimated. Measurements with a counter have confirmed these result with a precision of around 30 %. Using the results for the photopeak number 3 a random coincidence rate of 40 Hz is estimated for 10 ns long pulses. Assuming a photon detection effiency of 60 % five photons have to reach each SiPM to see a coincicdence signal there. Using a fiber with intact multicladding this should be achievable [Rop07].

7. Extended Commissioning

7.1. Testing of Gas Tightness

The gas tightness is an important parameter for the VDC because a contamination will affect the drift velocity. To characterize the gas tightness the behavior of leaks has to be known. The simplest form is approximating leaks as small holes with laminar flow through them. For a laminar stationary flow of an incompressible uniform viscous liquid, as approximated for gases flowing through a cylindrical tube with a constant circular cross section, the law of Hagen Poiseuille can be used [Dem05a]. For a given tube with fixed diameter and length follows:

$$\frac{dm'}{dt} \propto \Delta p. \tag{7.1}$$

m' = mass of flowing gas
t = duration of the gas flow
Δp = difference in pressure between beginning and ends of the tube (inside and outside of a chamber)

The ideal gas law for a gas inside an enclosed volume $V_{chamber}$ is

$$p \cdot V_{chamber} = nR \cdot T, \tag{7.2}$$

with
p = pressure inside the enclosed gas volume
$n = m/M$ amount of substance of the gas inside the enclosed volume
m = mass of the gas inside the chamber
M = molar mass of the gas
R = gas constant
T = temperature of the gas inside enclosed volume.
For a constant temperature and $V_{chamber}$, solving Equ. 7.2 for M and inserting this into Equ. 7.1 leads to

$$-\frac{dp}{dt} \propto \frac{R \cdot T}{V_{chamber} \cdot M} \cdot \Delta p \propto \Delta p, \tag{7.3}$$

because the change $\frac{dp}{dt}$ is equal to the flow in Equ. 7.1 ($dm' = dm$). The negative sign for $\frac{dp}{dt}$ has to be inserted since the pressure inside the chamber decreases. For a constant pressure p_{out} outside the chamber, one has

$$\frac{dp}{dt} = \frac{d(p_{out} + \Delta p)}{dt} = \frac{d\Delta p}{dt}. \tag{7.4}$$

Using this, from Equ. 7.3 follows

$$\frac{d\Delta p}{dt} \propto \Delta p. \tag{7.5}$$

7. Extended Commissioning

Thus, the time dependence of the differential pressure inside a constant volume can be described by

$$p(t) = p(t = 0) \cdot e^{-\frac{1}{\tau} \cdot t}, \tag{7.6}$$

with a time constant τ.

A more general discussion of leak rates can be found in [Sowa03].

The Lab View program "gastightness" (using a 14-bit ADC for readout of the pressure device) measures the differential pressure between the VDC chamber volume and the outside as a function of time. By an exponential χ^2-fit following Equ. 7.6 the time constant is determined.
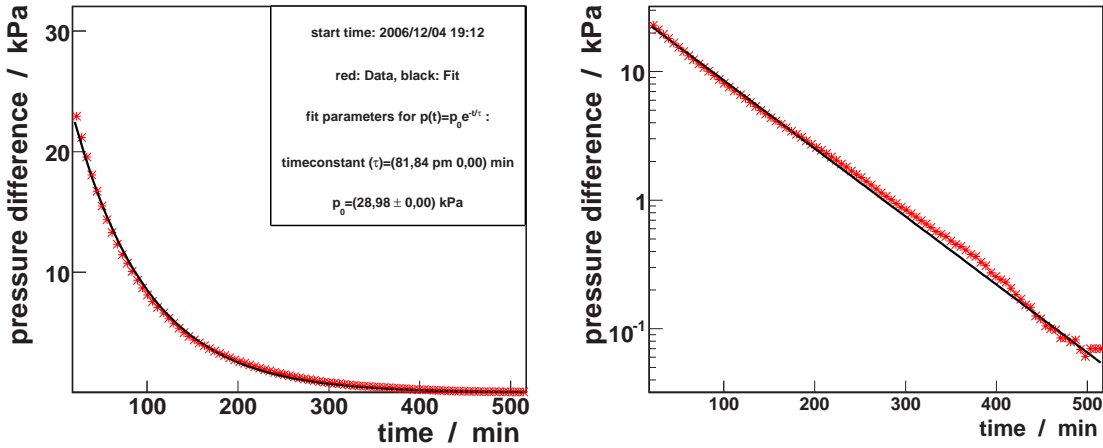
Figure 7.1.: *Pressure in the VDC with respect to the outside as a function of time in linear (left) and logarithmic plot (right) for the VDC prototype. Here the time constant is 82 min.*

The result shown in Fig. 7.1 has been measured after improvements at the bottom part of the chamber volume and gluing some parts like the HV supply connector for the field shaping grids and the anode wire. The determined time constant τ covered a range from 20 min up to 250 min. For lower pressure differences the data points at the right part of Fig. 7.1 are outside the fitted line because here variations of the room pressure affect the pressure difference much more than for higher pressure differences. Also the resolution of the pressure device will cause effects. Each data point value and its statistical error are obtained from averaging of 1000 successive measurements.

7.2. High Voltage Issues

The first tests of the high voltage robustness were done with a simple power supply without any monitoring. By replacing the front part of the VDC with a acrylic glass cover, discharges from the cathode or the grid to grounded parts of the chamber have been localized when So one could see the discharges by sparks and also could hear them. In addition the current was monitored. Using this procedure, HV flashovers from the cathode to one of the cathode holders were detected at the early prototype. They were fixed afterwards by improving the insulation around the cathode holders.

The following tests were done automatically by the "trip"-function of the HV-supplies from

CAEN (N470 NIM-module and the A426 module for the SY-127 system crate [Caen05], Fig. C.1). The "trip"-function will shut off the voltage for the corresponding channel if the current is higher than an adjustable value (I_0) for a certain time, the trip time t_{trip}. The minimal trip time for the CAEN devices is 0,2 s. Using this function, tests indicated that the prototype cannot be run with $I_0 = 90\,\mu A$, $U_{cathode} = -15\,kV$ and $t_{trip} = 0,2\,s$ for 1 h, but by enlarging I_0 to $130\,\mu A$ a run time of more than 1 h could be achieved. The nominal current at the cathode for $U_{cathode} = -15\,kV$ is around $63\,\mu A$ for the used resistors of $20\,M\Omega$ between each grid. Further tests show that the prototype can be run stably with $I_0 = 120\,\mu A$, $U_{cathode} = -14,5\,kV$ and $t_{trip} = 1,0\,s$.

The software "Oo2"[1], based on [SUR02] reads the current and voltage of cathode and anode at regular time intervals and writes them to a data file for each measurement. For the cathode and anode voltage HV curves can be programmed, i.e. a series of increasing or decreasing values of the voltage for each measurement. In addition the program can change from increasing to decreasing or from decreasing to increasing after half of the programmed measurements have been finished.
Additionally the program reads the currents every second without writing them to look for over-currents. Only if an overcurrent is detected this will be marked in the data file.

By recording the voltage and current, the HV stability of the VDCs can be tested. Overcurrents which last longer than the read out interval can be detected (Fig. 7.2 left plot). Furthermore, an overcurrent can cause a breakdown of the cathode voltage (Fig. 7.2 right plot) because of the limited output power of the HV supply.
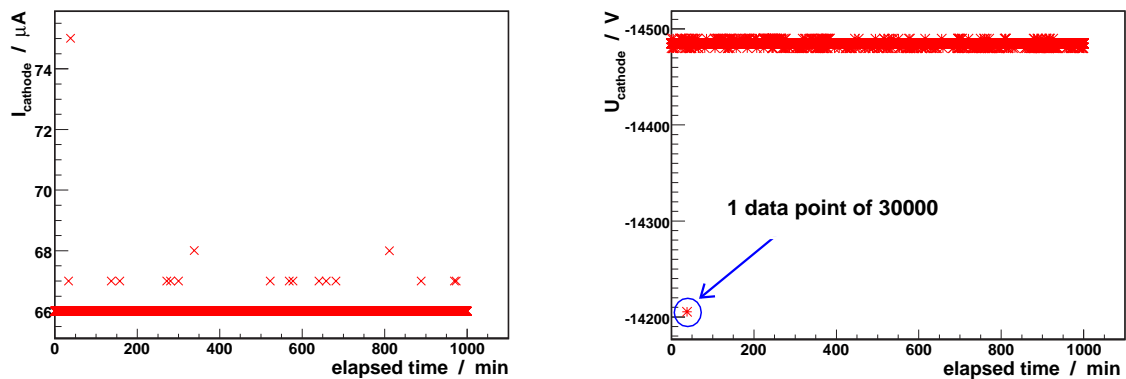
Figure 7.2.: *Current (left) and voltage (right) at the cathode as a function of time. Each measurement comprises 30000 data points. For the current, there are around 20 data points with slightly increased values.*

To test if these breakdowns are caused by external voltage fluctuations, the current at the cathode can be plotted as a function of the cathode voltage. In Fig. 7.3 one can see that the point with $75\,\mu A$ belongs a voltage of around $14,2\,kV$ instead of the applied $14,5\,kV$. Thus, the breakdown of the voltage is caused by an overcurrent and not by fluctuation of the supply voltage.

---

[1]name by [Tsi06]
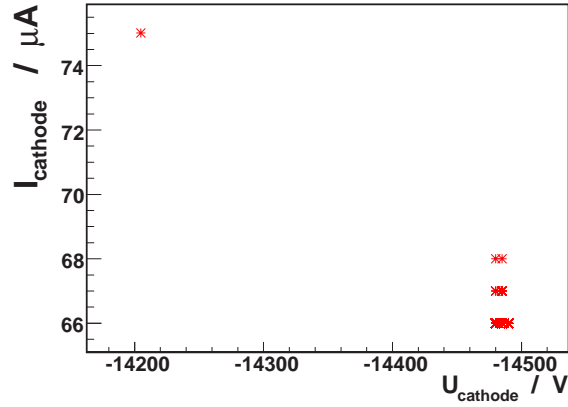
Figure 7.3.: *Current at the cathode as a function of the voltage at the cathode. The single point of lower voltage is indeed related to a higher current.*

For a long time measurement with a high frequency of data taking, a histogram of the voltages and currents is well suited to see the rate at which these effects appear (Fig. 7.4).
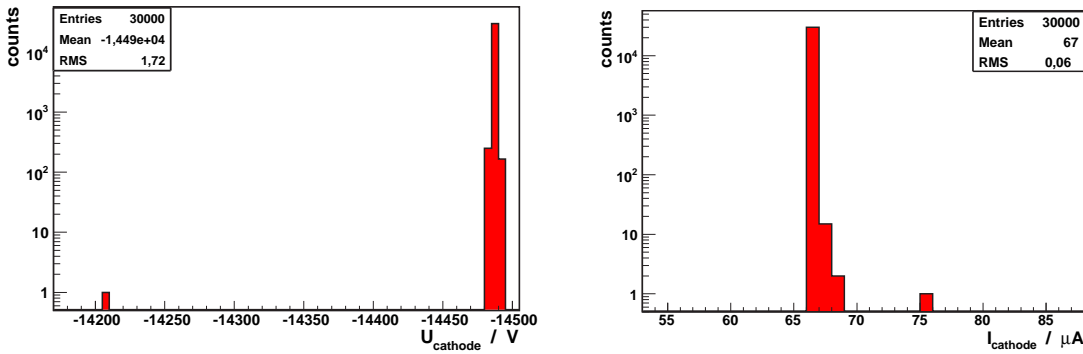
Figure 7.4.: *Histograms of the current (left) and the voltage(right) at the cathode for a measurement of 1000 min and readout interval of 2 s. Same date as in Fig. 7.2 and Fig. 7.3.*

Looking at Fig. 7.4, one can see that the relative rate of overcurrents ($> 70\,\mu A$) is small (1 in 30000). Therefore, the effect on the drift velocity measurements should be small and the long time stability of the VDC should be guaranteed. (Too many overcurrent pulses, which mean small discharges, can damage the electrical insulation causing a lower HV robustness.)

In a perfect HV stable chamber the voltage and current should always remain at the same values except for the effect of "bit-flipping", i.e. fluctuations within the resolution[2]. Thus the RMS of the voltage and current is an indicator for the HV stability. The voltage at the anode is constant (Fig. 7.5).
Up to $-14,4\,kV$ the prototype seems to be very stable except for some small overcurrents of less than $10\,\mu A$ above the nominal current in a time interval of more than 2 h.

---

[2] $1\,\mu A$ for the current, $5\,V$ for the voltage at the cathode and $2\,V$ for the voltage at the anode for the different HV-modules used [Caen05]
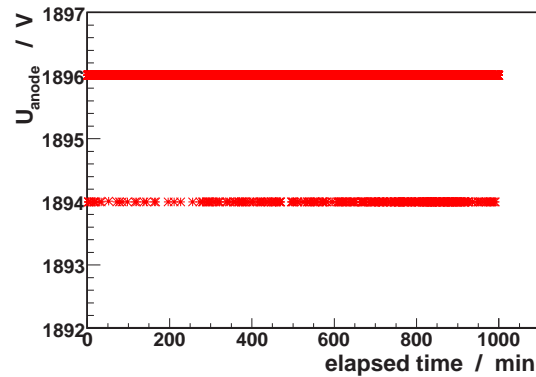
Figure 7.5.: *Voltage at the anode as a function of time (the current is too small to be measurable). There are only two different measured values for the voltage (are within the resolution of the device) and no breakdowns of the voltage.*

The very rare cathode overcurrents can be caused by collecting charges on the glue because of hits of β-electrons there, or ions drifting to the cathode.

The final read out system should remove the data points taken in a time interval during an overcurrent because the E-field inside the VDC is deformed during these discharges and thus the value of the drift velocity is changed.

To detect short overcurrents a faster device has to be used. A device called "CUMO"[3] can measure the current with a time resolution of around $1\,\mu s$, but it is not suitable for the voltages the VDC needs [Hil07, Rei07].

7.3. Configurations

7.3.1. Setting of Anode Voltage

Effects on the drift time spectrum:
The number of particles in the avalanche region of the gas (Sec. 4.3) is an exponential function of the anode voltage. A too low anode voltage will cause a low efficiency for detecting arriving drift electrons. A too high anode voltage will cause too much noise for anode signals because then, small random ionizations on dust particles near the anode will cause avalanches. In addition to this, at high avalanches in the gas such an amount of space charges from ions can be produced that the anode wire is shielded by them. This would limit the avalanche development in the gas. By running *anode curves*, i.e. series of measurements of the rate, current or the drift velocity with different anode voltages, the optimal anode voltage can be found using the following criteria:

- high event rates, nearly independent from small variations of the anode voltage

- small number of events outside the peaks in the drift time spectrum (low noise level)

- small number of after pulses (compare to Sec. 7.3.4)

As seen in Sec. 7.2 the high voltage robustness at the anode is perfect.

By comparing the data for different voltages, the optimal anode voltage was determined to be $1850\,V$ (May 2006). After some months with modifications at the VDC for HV robustness

---

[3]**CU**rrent **MO**nitor

7. Extended Commissioning

(Sec. 7.2) and gas tightness (Sec. 7.1) the behavior of the anode has changed somewhat. In August 2006 an optimal anode voltage $U_{anode} = 1950\,$V was obtained (Fig. 7.6). Because of the multiple changes at the VDC the behavior of the anode is not considered as an effect of aging. Thus, one should revisit this optimization when the series production VDCs are available.
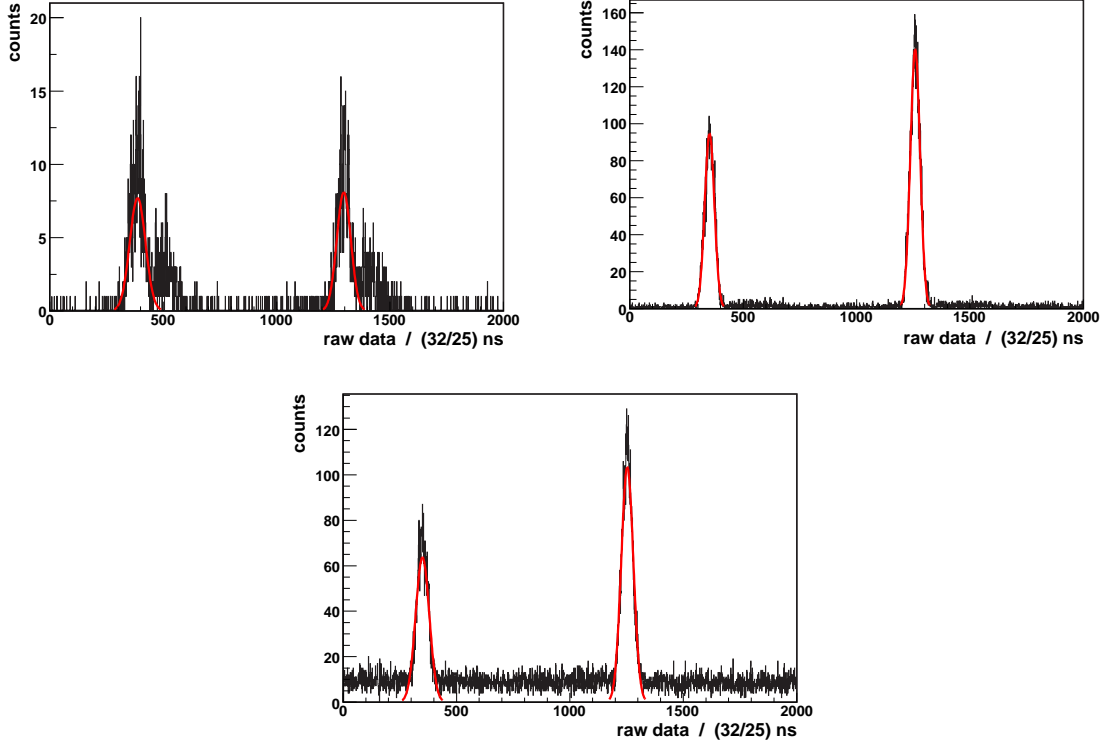
Figure 7.6.: *Determination the optimal anode voltage U_{anode} from runs of similar durations:*
(a): A too small value of $1700\,$V leads to too low statistics.
(b): The determined optimal value of $1950\,$V.
(c): A too large value of $2350\,$V causes too much background.
The digital anode pulses had a pulse length of around $10\,$ns.
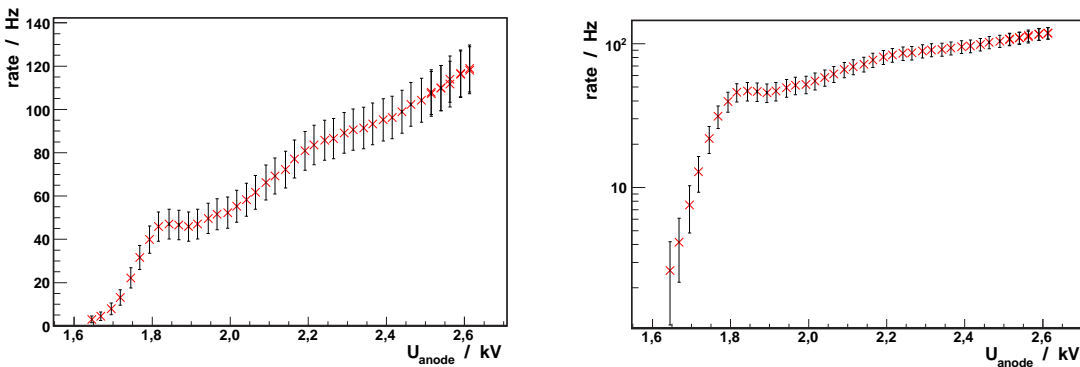
Figure 7.7.: *The VDC signal rate for a read out time window of $2\,\mu$s after the trigger pulse as a function of the anode voltages U_{anode} (linear (left) and logarithmic (right)) at a fixed trigger rate. The readout rate is proportional to the efficiency for detecting drifting electrons at the anode. The error bars are statistical errors ($\propto \sqrt{rate}$). On the linear plot, note the plateau at about $1{,}80\,$kV to $1{,}95\,$kV.*

Effect on the anode rate (only):
Further analysis to set an optimal anode voltage has been done by measuring the anode rate. Assuming a fixed trigger rate depending on the trigger system only, the VDC signal rate depends on the efficiency of the VDC and the noise at the anode. The efficiency is the relative number of events with anode pulse inside the time window of a triggered event. The total rate should converge to a fixed value (see Fig. 7.7), if there are no noise pulses, corresponding to an efficiency of one. The average pulse amplitude increases exponentially with the anode voltage ($A_{signal} \propto e^{U_a}$, [Saul77]). The pulse amplitude is statistically distributed. Thus, for a fixed threshold, by applying a larger anode voltage more signals will exceed the threshold. For high anode voltages the rate can increase to values above an efficiency of one because of more noise. For very high anode voltages a transition to the Geiger region (Fig. 4.2) is possible. This could damage the read out electronics. The increase of the (untriggered) anode rate as a function of the anode voltage is shown in Fig. 7.8. Generally also a too long digital pulse length can mask new pulses arriving during the current pulse. This is not the case here. E.g. even for 400 ns long pulses with a rate of 200 kHz this effect of random coincidences (Sec. 6.1) causes a rate of signals masked with other signals of 16 kHz corresponding to 8 % of the signal rate. At our typical working rate of 50 Hz, this effect would amount to 10^{-2} % and is thus neglible.

Finally the optimal anode voltage determined by looking at the anode rate is between 1,80 kV and 1,95 kV because of the plateau in Fig. 7.7.
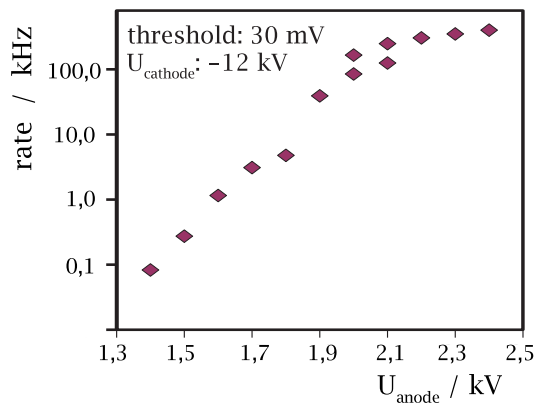
Figure 7.8.: *The pulse rate at the anode (untriggered mode) as a function of the anode voltage U_{anode} taken with a counter. At around 2 kV the efficiency should have reached 1 so that the rate begins to be constant. The pulse length is set to around 10 ns, meaning that after pulses are also counted here.*

Effects on the drift velocity:
Because of other effects, for the final operating mode the parameters of the chamber like the anode voltage should not be changed to avoid unforeseen effects. Nevertheless the anode voltage should not affect the drift velocity (see Sec. 5.3). The VDC signal rate has no influence on the systematic errors of the drift velocity. Around the optimal anode voltage, in the working region, the change of the drift velocity as a function of the anode voltage is found to be around 1,7 μm ns^{-1} kV^{-1} (Fig. 7.9) in the working region of U_{anode} between 1,9 kV and 2,1 kV.

| date | increase of v_{drift} | | χ^2/ndf | errors |
| | value | error from fit | | normalized to $\chi^2/ndf = 1$ |
	/ $\mu m\,ns^{-1}\,kV^{-1}$			/ $\mu m\,ns^{-1}\,kV^{-1}$
2006/07/18	1,062	0,057	25/10	0,091
2006/07/25	1,293	0,026	1413/38	0,159
2006/08/10	1,698	0,078	22/14	0,097
2006/08/10	2,259	0,114	24/14	0,148
2006/08/21	6,287	0,059	1372/22	0,462
2006/11/14	1,675	0,199	3,2/8	0,126
2006/11/29	2,156	0,051	319/29	0,170
2006/11/30	2,159	0,057	77/16	0,126

Table 7.1.: *Variation of the drift velocity as a function of the anode voltage in the region between $1,7\,kV$ and $2,1\,kV$ for some measurements done under same conditions. For some runs the linear fit is not a good approximation as evidenced by large χ^2 values. The weighted mean is $(2,69 \pm 0,05)\,\mu m\,ns^{-1}\,kV^{-1}$.*
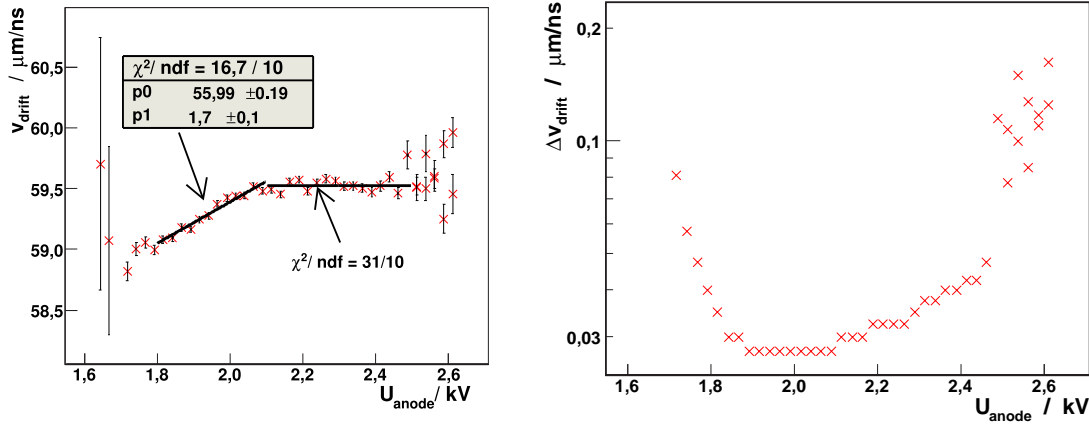
Figure 7.9.: *The drift velocity (left) and its error (right) as a function of the anode voltage U_{anode}: In the working region ($1,9\,kV$ to $2,1\,kV$) a linear fit $v_{drift} = p_0 + p_1 \cdot U_{anode}$ was done. The change of 1% in this region could be an indicator for a systematic error.*

For a relative measurement of the drift velocity this change has no effect for a constant anode voltage with a precision of $2\,V$. For the absolute value of the drift velocity this effect needs further analysis. In Tab. 7.1 the evaluation of several anode curves (like in Fig. 7.9) is shown. One explanation for this effect of changing drift velocity could be a deformation of the anode pulses. This deformation must depend on the anode voltages and on the drift length. Because of the transverse diffusion less drift electrons from the β- beam at larger distance from the anode can reach it. A change of the number of arriving drift electrons changes the behavior of the gas avalanche. Thus, the point of time when the amplitude of the anode pulse is higher than the threshold at the discriminator could change. If it was just an effect of changing the E-field inside the drift volume, the position of both peaks (see Fig. 7.10) should change equally. In general the drift velocity is not affected very much by the anode field because the anode field does not deform the E-field between the two β-beams. In simulations even for a anode voltage of $2,5\,kV$ and no voltage applied to the cathode and field shaping tubes the E-field[Alt07] at the region of the region of the first *beta*-beam the E-field is below $0,4\,V/mm$.
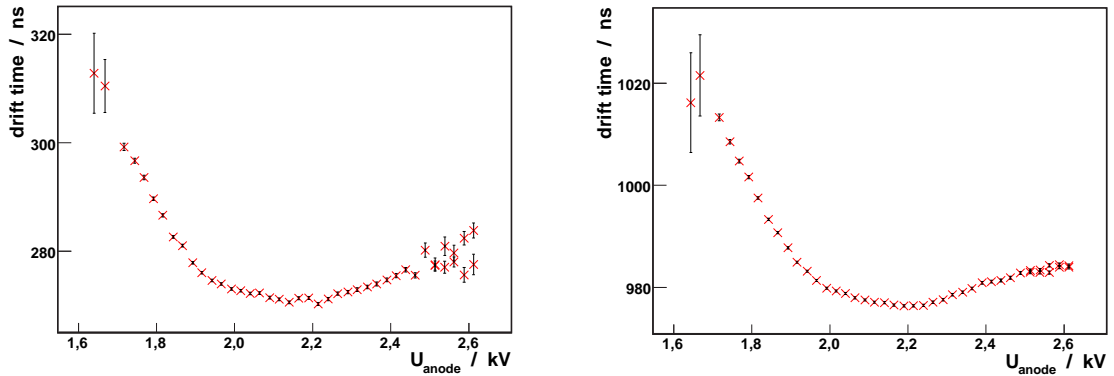
Figure 7.10.: *The drift times of the drift electrons originating from the β-beam closer to the anode (left) and farther from the anode (right) as a function of the anode voltage U_{anode}: A higher anode voltage should cause a higher drift velocity in the region close to the anode only and have no influence beyond the slit. Indeed, the total drift time variation in the region 1,9 kV to 2,1 kV is about 6,5 ns and 10,0 ns for the first and second beam, respectively, while their difference, 3,5 ns is much smaller. The time difference between both curves should not be affected by the anode voltage. Therefore the measured increase of the drift velocity can not be explained by this change in the anode voltage.*

The deformation of the anode pulses can be a deformation of the pulse (rising) edges or of the pulse widths. The difference between the widths of the pulses from the first and second beam is for all U_{anode} between 1,8 kV and 2,2 kV constant with around 0,5 ns (right part of Fig. 7.11) which is inside the statistical error.
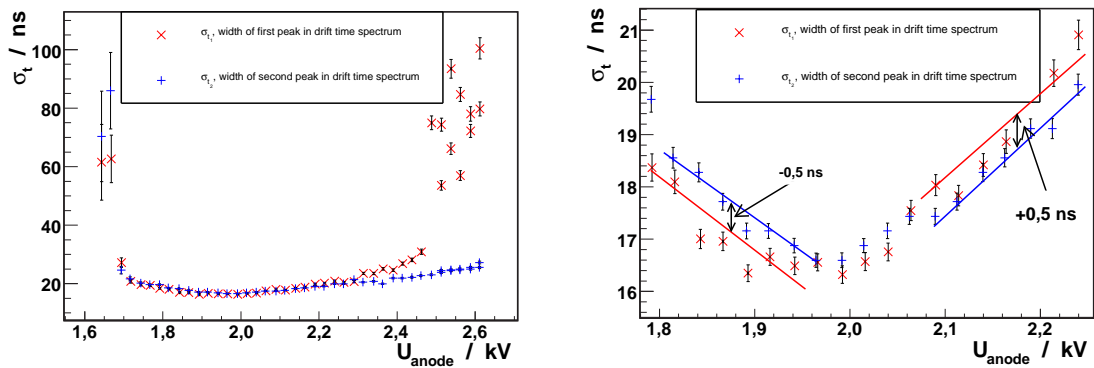
Figure 7.11.: *The width of the peaks in the drift time spectrum corresponding to each radioactive source as a function of the anode voltage U_{anode}.*
Left) It is quite constant (20 %)in the relevant range of 1,7 kV to 2,3 kV.
Right) enlarged view: The change between the widths of the pulses from the first and second beam is around 1 ns for the working region.

As a further analysis of those effects, the shape has been examined by using a digital oscilloscope [Tek96], shown in the next section (Sec. 7.3.2).

7.3.2. Anode Pulse Shape
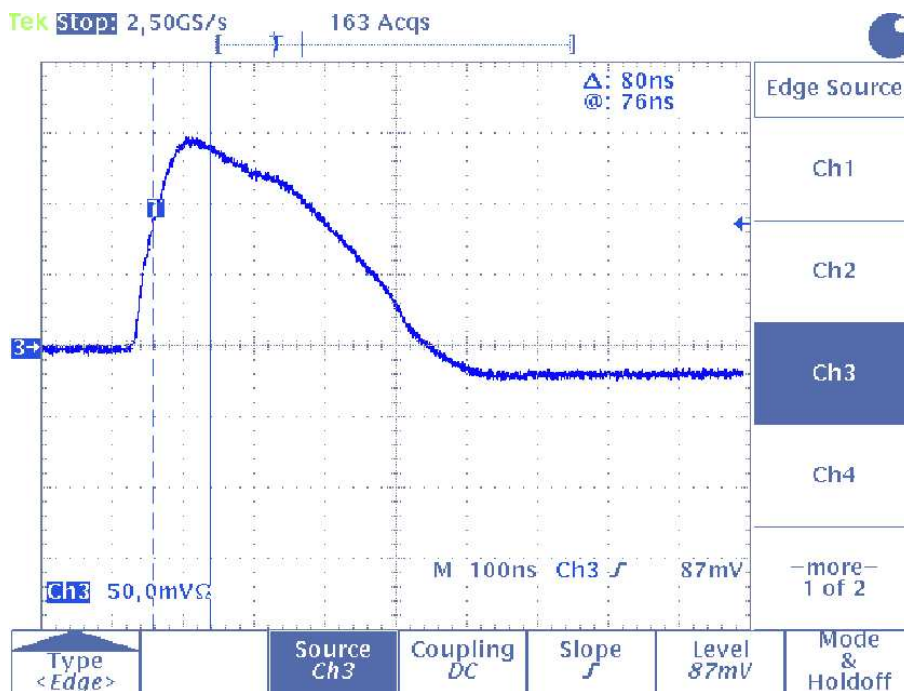
Figure 7.12.: *An analog VDC anode pulse measured with an oscilloscope. The signal rise time, defined as the region between 10 % and 90 % of the maximum, has a duration of around 50 ns. ($U_{cathode} = -14$ kV, $U_{anode} = 1{,}85$kV.*

The anode pulse shape (signals after the preamplifier) has been analyzed with an oscilloscope [Tek96]. Because the pulse shape varies (Fig. 7.12 is just an example for a single pulse) the "average mode" was used which calculates the average of each time position for a maximum of 10000 values.

The shape of the rising edge of the anode signals seems to be independent from the position where the drift electrons have been created (see Fig. 7.13 and Sec. 9).
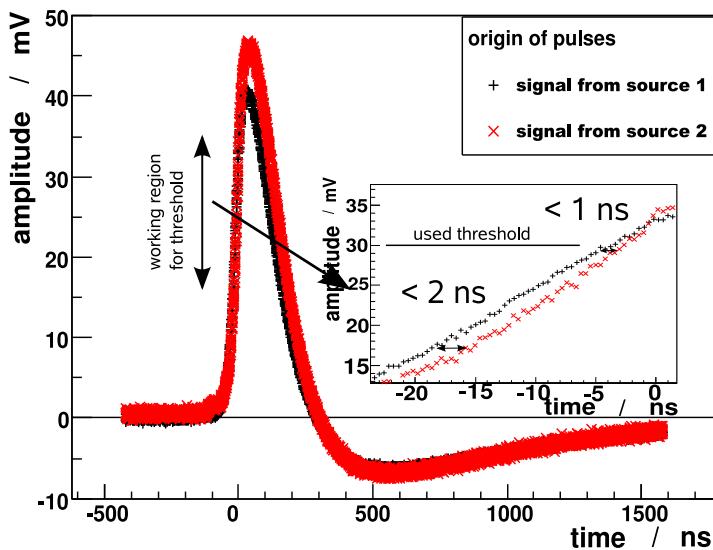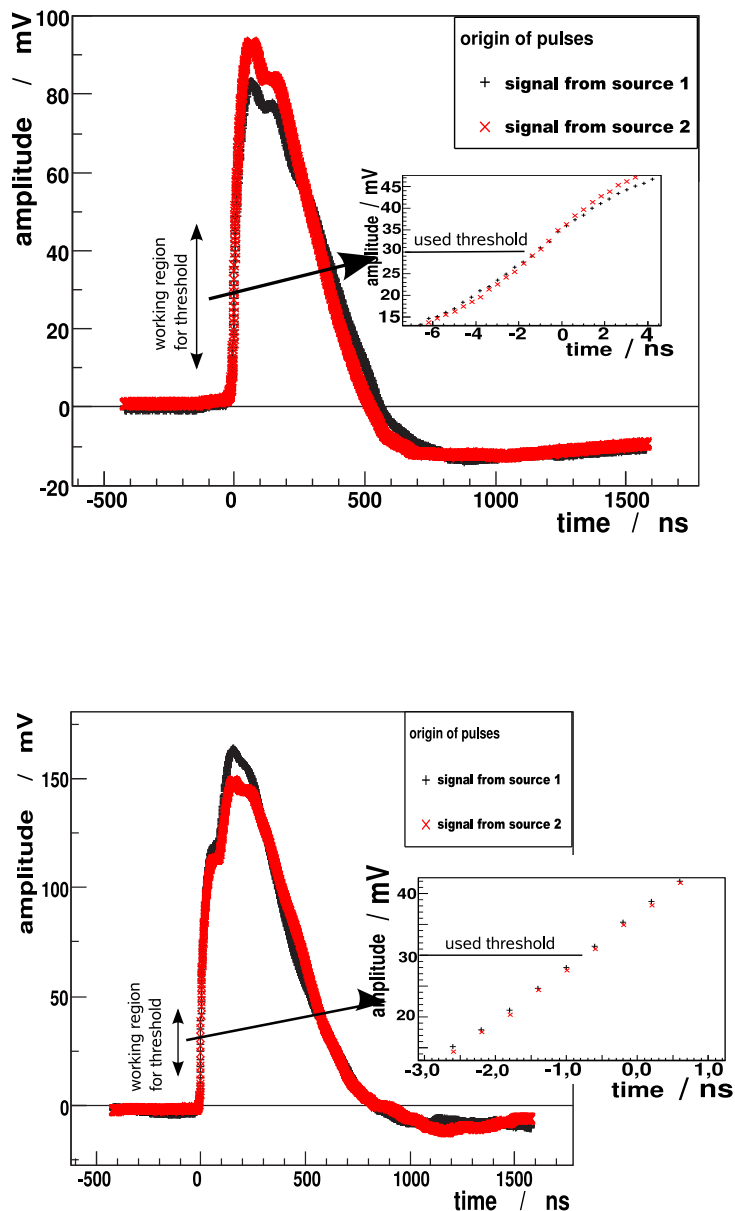
Figure 7.13.: *Anode pulses for three different anode voltages (1,6 kV, 1,9 kV, 2,4 kV) measured by an oscilloscope in the "average mode" (mean over 10000 pulses). The variation of the anode signal times in the region of the rising edge (between around 15 mV and 45 mV) is below 1 ns. The shown pulses has been aligned by setting the first point with an amplitude larger than 30 mV to 0 ns.*

The pulse amplitude (Fig. 7.14) should increase exponentially [Saul77] for a drift chamber working in the proportional region (Sec. 4.4). A deviation from this could indicate transition to the Geiger-mode. The "cut" at around 1,9 kV in Fig. 7.14 could be an effect of the special geometry of the VDC. In a CMS DT chamber particles with a frequency of 0,01 Hz/mm^2 to 0,10 Hz/mm^2 pass the drift cell of approximately 10 mm thickness and 40 mm width. Thus, at the anode wire there is a signal rate of at most 0,1 Hz/mm$^2 \cdot 40$ mm $= 4$ Hz/mm.

In the VDC, the measured signal rate at the anode wire (Fig. 7.8) is around 100 kHz and limited to a region of about 2,5 mm along the anode wire. This is five orders of magnitude more. More

drift electrons in the region around the anode will cause more ions in this region having effects as space charges. They will shield the electric field of the anode and limit the gas avalanche. Thus, the "cut" in Fig. 7.14 could be the normal exponential increase before the gas avalanche is limited by space charges. The non linear behavior is not an electronics effect of the preamplifier [Hil07]. This has also been excluded by measurements with test pulses.
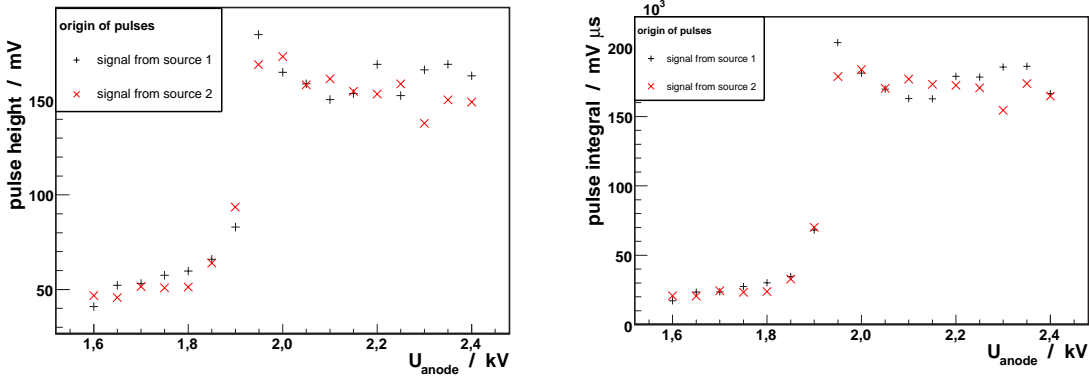
Figure 7.14.: *Pulse height (left) and peak integrals (right) of the anode pulses as a function of the anode voltage. The amplitude is measured downstream the preamplifier. In the first part a sharp increase can be seen.*

The pulse width (picture 7.15) seems to have the same behavior as the pulse amplitude: For increasing anode voltages it increases exponentially before it is limited. A longer analog anode pulse tends to mask after pulses if they are close-by as can bee seen in Fig. 7.13). The "cut" in the right part of Fig. 7.14 can be explain if here pulse and after pulse meld into each other (see Fig. 7.13).
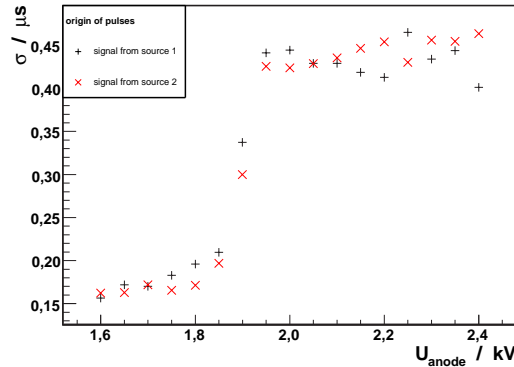
Figure 7.15.: *Width (std. dev.) of the anode pulses as a function of the anode voltage.*

By comparing Fig. 7.14 and 7.15 with Fig. 7.13 one can assume that with a higher anode voltage more after pulses melt with the first pulse. This could explain Fig. 7.14 and Fig. 7.15. Local space charge effects limit this effect, as can be seen at the plateau at $U_{anode} > 1{,}9\,\text{kV}$ in Fig. 7.14 and 7.15.

A satisfiable explanation for the dependence of v_{drift} on the anode voltage is not given by this, since a longer analog pulse does not change the point of time when the pulse amplitude is higher than the threshold at the discriminator.

7.3.3. Setting of the Threshold

The threshold at the discriminator for the readout of the anode signals affects the noise rate, the efficiency and the rate of after pulses (Sec. 7.3.4).
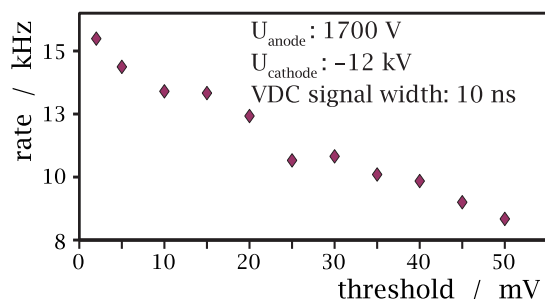
Figure 7.16.: *The anode pulse rate as a function of the threshold (after the preamplifier) at the VDC. Untriggered continuous measurement.*
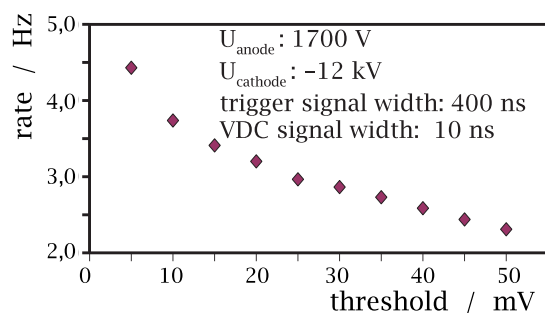
Figure 7.17.: *The anode pulse rate as a function of threshold at the VDC, in coincidence with a $400\,\mathrm{ns}$ long trigger signal. In this way only signals within the region of the first peak are measured. The trigger rate was around $30\,\mathrm{Hz}$.*
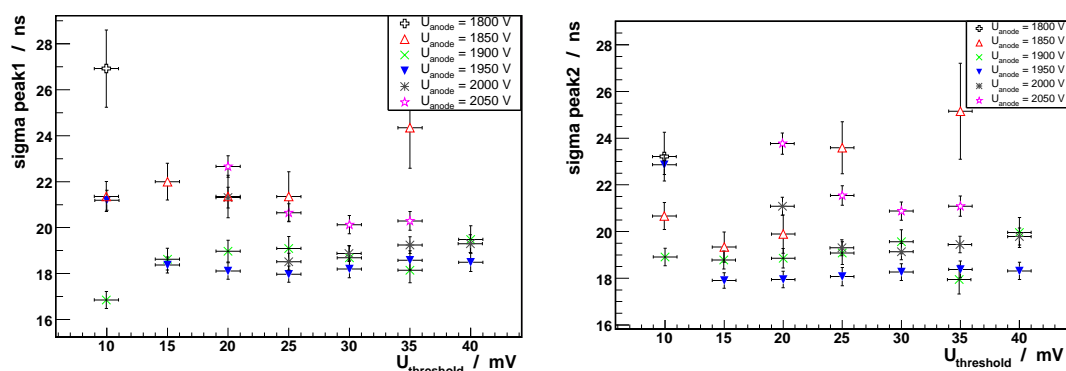
Figure 7.18.: *The peak width of the first (left) and second (right) peak in the drift time spectrum as a function of the threshold for the anode pulses (peak widths from gaussian fits to the peaks). The threshold seems to have no significant effect on the peak width.*

By a simple counting of the anode signal as a function of the anode voltage (Fig. 7.16) noise and after pulses (Sec. 7.3.4) cannot be distinguished from the wanted signal pulses. Here the largest part of the measured 13 kHz is caused by β-particles that have not create a trigger signal. Therefore, the anode signals were measured in coincidence with a 400 ns long trigger signal (Fig. 7.17). Thus, only signals in the region within the first peak of the drift time spectrum are registered because the first peak is (for a cathode voltage of -12 kV) in the region around 300 ns after the trigger signal. Now a rate of around 13 Hz has been measured, which is around 50 % of the VDC signal rate.

Finally a threshold of 30 mV was chosen, which is far away from the "noisy region" at 15 mV but is still resulting in a sufficient rate. The effect of the threshold on the peak width in the drift time spectrum has been examined for several anode voltages (Fig. 7.18). No significant effect could be found (The effect of the anode voltage was examined in Sec. 7.3.1). The drift velocity does not depend on the threshold (Fig. 7.19).
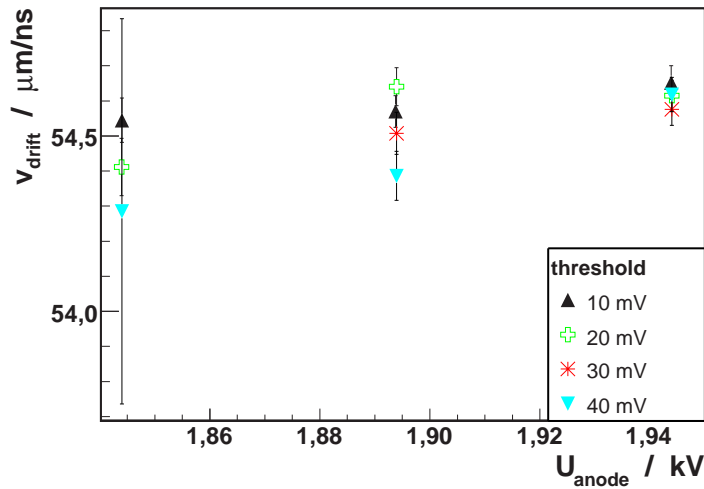
Figure 7.19.: *The drift velocity as a function of the anode voltage. For curves for four thresholds are shown. The is no significant dependence between threshold and v_{drift}.*

7.3.4. Reduction of After Pulse Rate

Because with the presently used DAQ system the anode times can not be associated with a certain trigger signal, after pulses can not be eliminated from the data by taking the first pulse of an event. After pulses can influence the fitted means of the peaks if the fit region includes the after pulse. To eliminate them from the data before the data is registered in the TDC, several methods have been examined.

To measure the after pulse rate (including noise) directly, a 400 ns long trigger signal was delayed by 300 ns. In this way the region starting at the end of the first peak in the drift time spectrum including the first after pulses is measured (Fig. 7.20). The after pulse rate seems to have the same behavior as the raw (untriggered) pulse rate (Fig. 7.8). For anode voltages above 1,8 kV the after pulse rate increases strongly. From Fig. 7.20 only, no optimal value for U_{anode} can be determined.
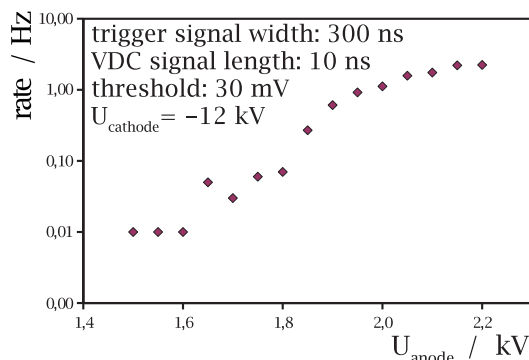
Figure 7.20.: *Anode pulse rate outside the first peak in coincidence with a 400 ns long trigger signal delayed by 300 ns. In this way only signals from the region after the first peak, i.e. its after pulse and the noise, are measured.*

The rate of the signals inside the peaks (Fig. 7.21) was determined by taking the anode rate in coincidence with the 400 ns long trigger signal (like in Fig. 7.17) because this is the region within the expected first peak. The rate seems to have the same behavior as the pulse amplitude (Fig. 7.14). Because the rate in Fig. 7.21 depends on the trigger rate the rate cannot be compared with Fig. 7.14. Assuming a uniformly distributed pulse amplitude the fraction of pulses larger than the threshold should be proportional to the pulse amplitude.

After pulses created by drift electrons causes by photons, that are emitted at the anode, by hitting the wall at the anode region, should have a delay of around $8\,\mathrm{mm}/(55\,\mu\mathrm{m}\,\mathrm{ns}^{-1}) = 150\,\mathrm{ns}$ ($8\,\mathrm{mm}$ = radius of anode region) WRT the signal pulse. This fixed delay is the feature which distinguished after pulses due to photoelectrons from those due to noise, which are uniformly distributed in time. Furthermore, this value agrees with the delay observed for the after pulses in Fig. 7.6a. Along the same line, for larger anode pulses the frequency of after pulses should increase and both pulses then merge - this is visible on the average pulse shape in Fig. 7.13b and 7.13c. This also explains why in Fig. 7.6b and c almost no after pulses are counted [Rei07].
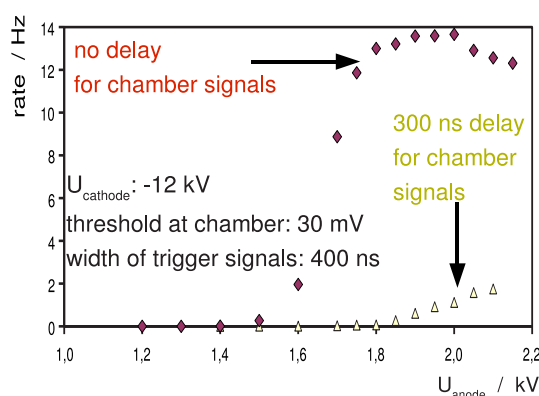
Figure 7.21.: *The pulse rate of the anode in coincidence with the 400 ns long trigger signal. In this way only signals up to the first peak are measured. In addition the data (lower curve from Fig. 7.20) for after pulses incl. noise in a delayed time window of same width are shown.*
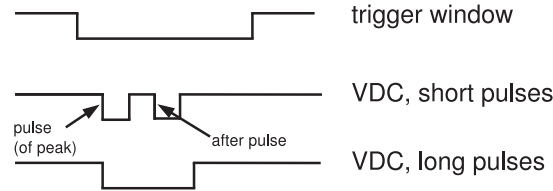
81

Figure 7.22.: *The anode rate depends on the length of the digital signals. Counting of after pulses is avoided by enlarging the length of the single VDC pulse.*

As shown in Fig. 7.22 a long digital anode signal will hide its after pulses because an additional pulse during a current pulse is not registered. By varying the anode signal length and comparing the rate with the rate with short ($\approx 5\,$ns) pulse length, the fraction the after pulses can be measured (Fig. 7.23). For digital signal lengths above 100 ns the fraction is constant, matching the distance between main pulses and after pulses in the drift time spectrum. By comparing to Fig. 7.15 after pulses should by visible only for time distances to the first pulse of more than 300 ns because they are masked by the first (analog) pulse. But if the amplitude of an analog pulse longer than 300 ns fluctuates the amplitude can drop below the predefined threshold and a second digital pulse is created that is seen as an after pulse (Remark in Fig. 7.13 the **average** of the analog anode pulses is shown.). Also the discriminator can cause such after pulses without that the analog pulse amplitude is below the threshold.
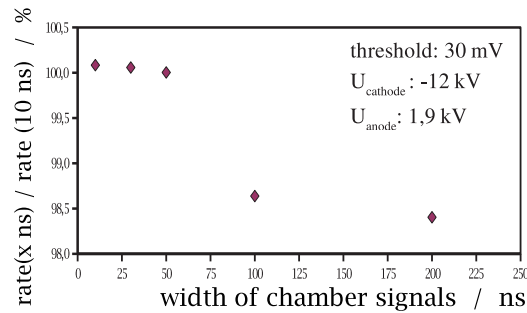
Figure 7.23.: *The fraction of the anode pulse rate of variable pulse length and 10 ns long anode signals. A large pulse length will mask the after pulse (threshold $= 30\,$mV, $U_{cathode} = -12\,$kV).*

With a long anode pulse only 1,5 % pulses are eliminated (Fig. 7.23), showing that in these runs the amount of vsible after pulses was small.

To determine effects of the anode voltage on the fraction of after pulses, the fraction of pulses when using long anode pulses (400 ns) to short pulses (10 ns) was measured as a function of the anode voltage (Fig. 7.24). The used anode pulse width of 400 ns (Fig. 7.24) includes approximately the arrival times of the after pulses t Fig. 7.6a. For the future work with the VDC the elimination of the after pulses out of the TDC data should be used because this is promised to be a more efficient method.
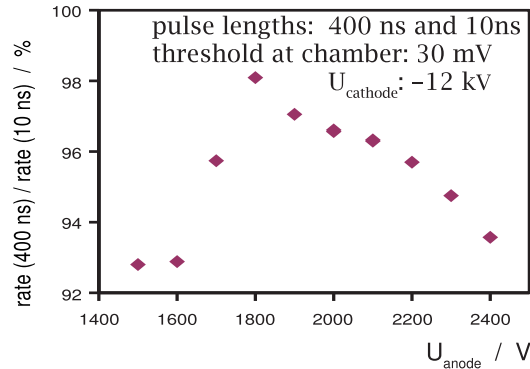
Figure 7.24.: *Ratio of anode signal rates for pulse width set to* 400 ns *and* 10 ns*, as a function of the anode voltage (threshold* = 30 mV*,* $U_{cathode} = -12$ kV*).*

A voltage around 1,9 kV was determined as an optimal value (Fig. 7.24) with a small fraction of after pulses for not too wide (digital) anode pulses.

7.3.5. Further Background and Noise Measurements

Noise from the anode will cause additional entries in the drift time spectrum. A non uniformly distributed noise and background can influence the position and shape of the peaks in the drift time spectrum.

The VDC is used in a "gated mode", i.e. only signals which arrive in a window (usually 2 µs) after the trigger are taken. Thus, for not time correlated noise and background only a small fraction of 0,2 ‰ for a trigger rate of 100 Hz of the noise is registered (2 µs · 100 Hz = 0,0002). There are two origins of background:

1. signals generated by β-electrons that have not activated the trigger

2. drift electrons caused by cosmic radiation or environment radiation.

There are two kinds of noise (signals not generated by drift electrons):

1. gas avalanches created by fluctuation in the gas (Sec. 7.3)

2. electronic noise

For the first origin of background see Fig. 7.8, where the anode rate was measured in an untriggered mode. Assuming a raw anode rate of 200 kHz, a trigger rate of 50 Hz and a trigger window of 2 µs, this background rate is 20 Hz including all after pulses.

The rate of cosmics (around 100 Hz/m^2) traversing the VDC is too low to have an effect on the rate.

In addition, the rate with radioactive sources, but without cathode voltage (Fig. 7.25) has been measured with a counter to determined effects of the anode field. For anode voltages larger than 1,8 kV a linear increase can be seen. The total rate is below 10 Hz. This could be affected by the electrical field of the anode which is (for a fixed distance) proportional to the voltage (Equ. 4.36). If the anode field reaches to the drift room it could appear as a (very small, see Sec. 7.3.1) drift field.

Figure 7.25.: *The raw anode pulse rate (untriggered) as a function of the anode voltage without cathode voltage ($U_{cathode} = 0\,V$) with the standard radioactive strontium sources as measured with a counter. The statistical error for each point is below $0,5\,Hz$ (duration of each measurement: $100\,s$).To scale the rate to the triggered mode ($50\,Hz$, $2\,\mu s$ window), the shown rates have to be multiplied by 10^{-4}.*

Redoing (Fig. 7.26) this without radioactive sources but with a cathode field ($U_{cathode} = -14\,kV$) results in a rate of around $50\,Hz$ and increases dramatically for anode voltages above $1,9\,kV$. A further examination of this effect at an anode voltage causing a high rate is done in Fig. 7.27.

Figure 7.26.: *The raw anode pulse rate as a function of the anode voltage ($U_{cathode} = -14\,kV$, without radioactive sources) measured with a counter (duration of measurement: $100\,s$). For a trigger rate of $50\,Hz$ and a window of $2\,\mu s$ only $0,07\,Hz$ from the maximum of the measured rate of around $700\,Hz$ would be inside the trigger window.*

To have more statistics and an automatic measurement (setting of voltages) the TDC was used for the next measurement. The anode rate without radioactive sources inside the VDC as a function of the cathode voltage was measured to examine effects of the drift field on the noise. Photoelectrons caused by UV-light emitted at the anode can knock out electrons (drift electrons) from the cathode. Potentially higher voltages at the cathode increase the probability for knocking electrons out off the cathode.

For a cathode voltage of around $U_{cathode} = -6\,kV$ the anode rate (Fig. 7.27) seems to have a minimum of around $0,5$ Hz while it increases up to $200\,Hz$ for $U_{cathode} = -15\,kV$ corresponding to the values in Fig. 7.26. For $U_{cathode} = -14\,kV$ there is a peak with a rate up to to $1\,kHz$. Without this peak there is some kind of plateau between $-14\,kV$ and $-15\,kV$.

Figure 7.27.: *The raw anode pulse rate without radioactive sources as a function of the cathode voltage ($U_{anode} = 1,9 \, \text{kV}$), measured with the TDC. For a trigger rate of $50 \, \text{Hz}$ and a window of $2 \, \mu\text{s}$ only $0,1 \, \text{Hz}$ from the maximum of the measured rate of around $1 \, \text{kHz}$ would be inside the trigger window.*

An increase depending on the cathode voltage of the probability for knocking electrons out of the cathode by UV-light could explain the increase of the rate. The plateau there can be some effect of saturation: When all UV-photons succeed in knocking out an electron, the number of created drift electrons should not increase anymore.

Another explanation for a contribution to Fig. 7.27 can be that the electronics noise depends on the cathode voltage. Thus, this effect can be associate to the first and second kind of noise. Since the maximum of the measured rate is still below $1 \, \text{kHz}$ and below $0,1 \, \text{Hz}$ inside the trigger windows ($50 \, \text{Hz}$ trigger rate, $2 \, \mu\text{s}$ window), the noise can be neglected compared to the backgrounds.

The measured rates of all kinds of backgrounds and noise are compatible with the entries outside the peaks of the drift time spectra (Fig. 7.6).

7.4. Effects of the Drift Field

The electrical field inside the VDC influences the drift velocity (Chap. 8). In addition there are some other effects.

Peak width as a function of the cathode voltage:
The distribution of the drifting electrons depends on the drift velocity. A larger drift velocity will cause a smaller transverse and longitudinal diffusion (Sec. 4.2). One effect of this are sharper peaks in the drift time spectrum. But this VDC effect is small compared to the effect of the collimator (for the β-beams) width: Given by the two collimators near the sources and the two collimator at the outlet slit for the β-beams, the beams of the β-electrons have a certain width B in the middle of the chamber. Thus, a variation of the drift time Δt_{drift} is given by

$$\Delta t_{drift} = \frac{B}{v_{drift}}. \tag{7.7}$$

Using this with an estimated value of $B = 1 \, \text{mm}$ for a gaussian distributed β-beam profile (instead of $B = 1,5 \, \text{mm}$ for an assumed sharp beam) and adding the diffusion given by Equ. 4.9, the expected peak width can be calculated (Fig. 7.28). The shape of the measured curve is described very well. For a better matching of the absolute values a more precise calculation of

the β-beam width, including effects of multiple scattering (Sec. 4.1.3) and δ-electrons is needed. In this case the real "sigma" of the beam with a width of $d = 1,5\,\text{mm}$ has to be calculated by the effective beam diameter to $0,4\,\text{mm}$.

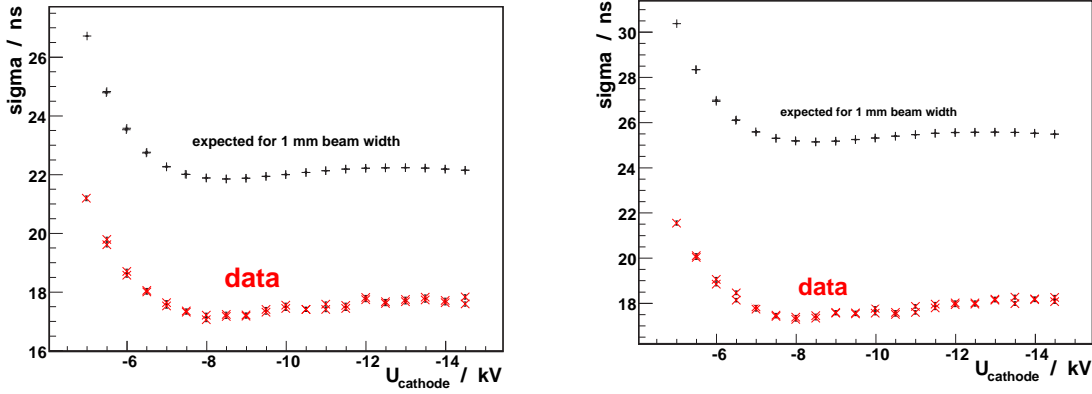By matching the beam width B to the data for σ a beam width of $0,75\,\text{mm}$ is calculated.

Figure 7.28.: *The peak width in the drift time spectrum corresponding to the radioactive source closer to the anode (left) and farer from the anode (right) as a function of $U_{cathode}$ and the theoretically expected curve. The expectation for a beam width (σ) of $1\,\text{mm}$ and diffusion following Equ. 4.9 with $D = 4\,\text{mm}^2/\text{s}$ [Kle05] is shown. Full agreement with the measured data is achieved for a beam width of $0,75\,\text{mm}$.*

Anode rate as a function of the cathode voltage:

A larger longitudinal diffusion for longer drift paths causes a larger pulse length (Sec. 7.3.2) because of a larger time difference between drifting electrons from one β-particle (page 74 of [Tav89]). Nevertheless, because of the small diffusion effects [Mag02], there should be no influence on the efficiency for detecting the drift electrons because of the lower drift electron density. In addition, the attachment of drift electrons to electronegative gases is a function of the drift velocity. Thus, the efficiency could be still influenced. In Fig. 7.29 the difference in the rate for an E-field range from $80\,\text{V/mm}$ to $220\,\text{V/mm}$ is below $10\,\%$.
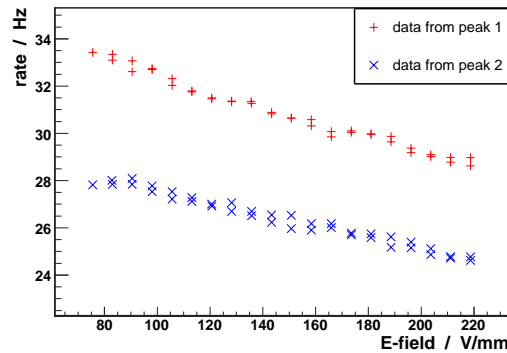
Figure 7.29.: *The signal rate of the VDC as a function of the E-field: The variation may be caused by a change of the cross section for attachment of drift electrons at different electron drift velocities. Here the oxygen volume fraction should be below $50 \cdot 10^{-6}$ as measured.*

7.5. TDC test

The time resolution and the behavior of the TDC [Caen05] were tested with a high precision delay generator. The delay generator generated two pulses, one was used as a trigger pulse and the delayed one was given as the signal to the TDC (Tab. 7.2).

delay at generator	average delay at TDC			$\mu_m - \mu_e$	steps in delay		
	expec. μ_e	measured μ_m	RMS_m		$\mu_{e,i}$ $-\mu_{e,i-1}$	$(\mu_{m,i}$ $-\mu_{m,i-1}$	$(\mu_{m,i} - \mu_{m,i-1})$ $-(\mu_{e,i} - \mu_{e,i-1})$
/ ns	/ TT	/ TT	/ TT	/ TT	/ TT	/ TT	/ TT
200,000	256,000	257,964± 0,005	0,465	1,964			
300,000	384,000	385,603± 0,005	0,489	1,603	128,000	127,639	-0,361
391,020	500,506	502,438± 0,007	0,714	1,932	116,506	116,835	0,329
400,000	512,000	513,518± 0,005	0,558	1,518	11,494	11,080	-0,414
500,000	640,000	641,585± 0,005	0,493	1,585	128,000	128,067	0,067
781,640	1000,499	1002,190± 0,004	0,467	1,691	360,499	360,605	0,106
800,000	1024,000	1025,680± 0,005	0,467	1,680	23,501	23,490	-0,011
1000,000	1280,000	1281,720± 0,004	0,449	1,720	256,000	256,040	0,040
1172,270	1500,506	1502,250± 0,004	0,445	1,744	220,506	220,530	0,024
1200,000	1536,000	1537,730± 0,004	0,445	1,730	35,494	35,480	-0,014
1500,000	1920,000	1921,800± 0,004	0,415	1,800	384,000	384,070	0,070
1700,000	2176,000	2177,830± 0,004	0,393	1,830	256,000	256,030	0,030
		average: 0,0047	0,483	1,733			-0,012
		StdDev: 0,0008	0,0837	0,1338			0,2081

Table 7.2.: *A test of the TDC [Caen05] with a high precision delay generator (TT= TDC Ticks = 25/32 ns. For each setting 10000 events with a rate of 1 kHz had been taken): Two signals with a certain delay (delay at generator) were given to the TDC. The measured delay μ_m is compared to the expected value μ_e. An average constant offset $\mu_m - \mu_e$ of 1,75 ns is observed. Between the expected $\mu_{e,i} - \mu_{e,i-1}$ and the measured $\mu_{m,i+1} - \mu_{m,i}$ differences between one value and the previous values the average of the difference $((\mu_{m,i} - \mu_{m,i-1}) - (\mu_{e,i} - \mu_{e,i-1}))$ is 0,2 ns. This is the error which will contribute to the drift velocity measurements.*

The observed constant offset between the expected delay and the measured one could be an effect of additional electronics (NIM to ECL converter) and has no influence on the drift velocity measurements because of the difference method. Any fluctuations from this additional electronics is included in the uncertainties of the present measurement. The TDC has a bin width of 0,8 ns. Assuming a perfect delay generator, for 10000 events a standard deviation of

$$\frac{0,8\,\text{ns}}{\sqrt{12}} \cdot \frac{\sqrt{4}}{\sqrt{10000}} = 4,6\,\text{ps} \tag{7.8}$$

is expected for the difference between the expected delay and the measured delay for two measurements at different delays ($\sqrt{4}$ for the 4 data points) [Rei07]. Subtracting the total time difference the measured value is 208 ps. Because the difference between two measurements at two delays has been measured the statistical effects are reduced. The measured deviation of 0,2 ns implies a systematic error for the absolute drift velocity measurement (Chap. 9).

7. Extended Commissioning

8. Drift Velocity Measurements with the VDC

8.1. Drift Velocity as a Function of the Drift Field

The drift velocity can be calculated with Equ. 4.18 if the cross section $\sigma(\epsilon)$ for the interaction of the drifting electrons with the gas atoms is known. The values measured with the VDC have been compared to simulations [Mag02] and also to other experimental results [Zha94].
The most interesting region is the plateau including the most relevant region, where the CMS DT chambers are measuring (180 V/mm to 260 V/mm [MUO97]). Thus, most data were taken for E-fields between 100 V/mm and 240 V/mm limited by the HV robustness of the VDC.

As explained before, the CMS VDC measures the time difference between two drift paths. The drift times for both drift lengths are shown in Fig. 8.1. The time of the first peak in the drift time spectrum is much less affected by the drift field because the drift path through the drift field is much shorter than the drift path of the drift electrons from the second peak. Thus, the drift velocity is mostly determined by the drift time of the second peak.
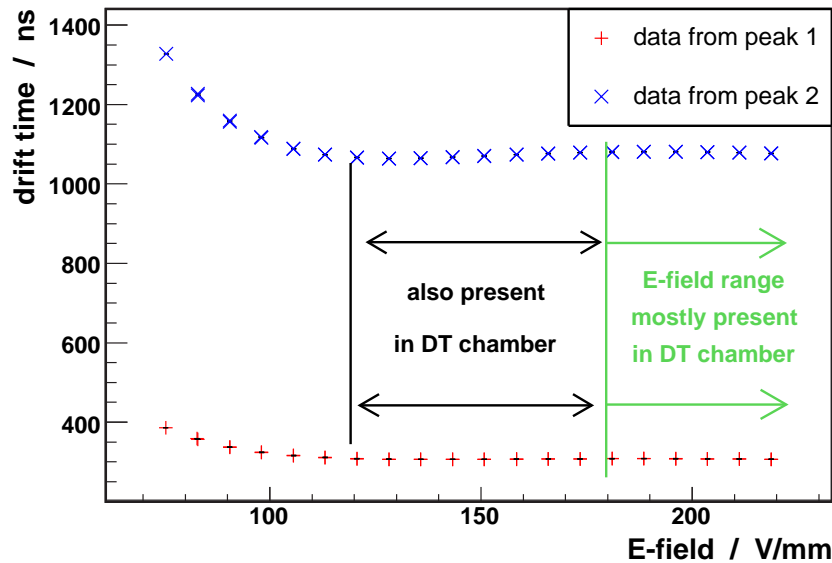
Figure 8.1.: *The drift times of the drift electrons originated at the two β-beams as a function of the drift field (E-field) E.*

For small E-fields the drift velocity is proportional to the E-field (Equ. 4.12). This can be seen in the first part of the curve in Fig. 8.2. For higher E-fields (> 80 V/mm) it becomes approximately constant. The gradient of v_{drift} can be used to determine the impact of uncertainties in the electrical field on the systematic errors (Chap. 9).

Figure 8.2.: *The drift velocity as a function of the electrical field.*
Left: linear, Right: logarithmic horizontal axis.
For low values of the E-field, the area where $v_{drift} \propto E$ can be seen.

8.2. Drift Velocity Dependence on Pressure

In the approximation (low E-fields) of Equ. 4.15 the drift velocity is a linear function of the pressure. The dependence for higher E-fields ($> 80\,\text{V/mm}$) is shown in Fig. 8.4).
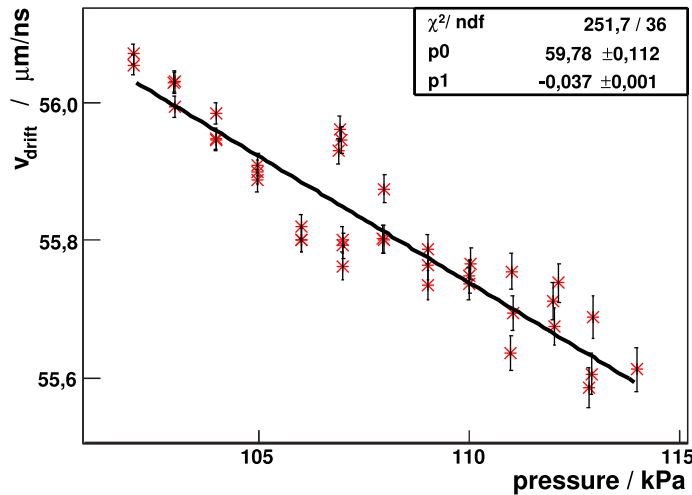
Figure 8.3.: *The drift velocity as a function of the pressure for an E-field of $212\,\text{V/mm}$ ($U_{cathode} = -14\,\text{kV}$): A linear correlation ($v_{drift} = p_0 + p_1 \cdot p$) can be seen. Only the error from the gaussian fit to the two peaks in the time distribution is shown. Cathode voltage and temperature are constant ($\Delta T,\ \Delta U_{cathode} < 1\ ‰$).*

Because for low E-fields v_{drift} is approximately proportional to E/p (see Equ. 4.15) v_{drift} is often plotted as a function of E/p. Although for higher E-field v_{drift} is often plotted as a function of E/p (Fig. 8.4).
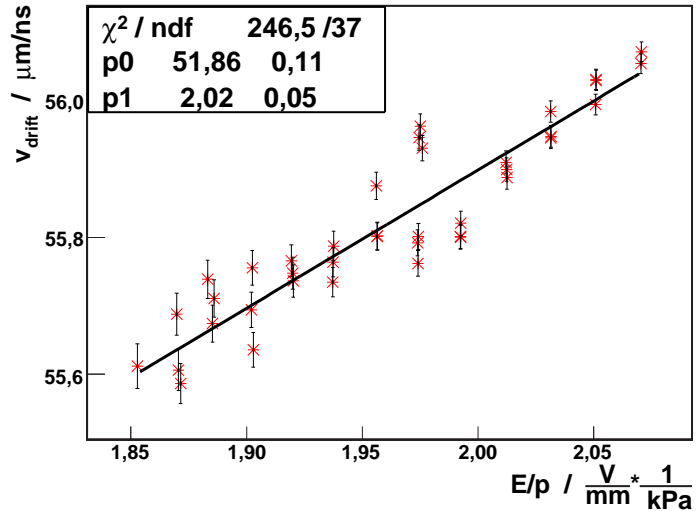
Figure 8.4.: *The drift velocity as a function of E/p. A linear fit ($v_{drift} = p_0 + p_1 \cdot E/p$) was done (same data sample as in Fig. 8.3, $E = const$).*

The drift velocity is (any) function of E/p. For the small region of E/p shown in Fig. 8.5 one can see that it is only approximately a linear function of E/p. For a further comparison v_{drift} has been plotted as a function of $1/p$ and E. The variation in E and p are in the same region (10 %) around the values of Fig. 8.4. Because for the small regions in the left part of Fig. 8.5 v_{drift} is approximately a linear function of the E-field, for small region of E and p the drift velocity is also for high E-field approximately a function of E/p.
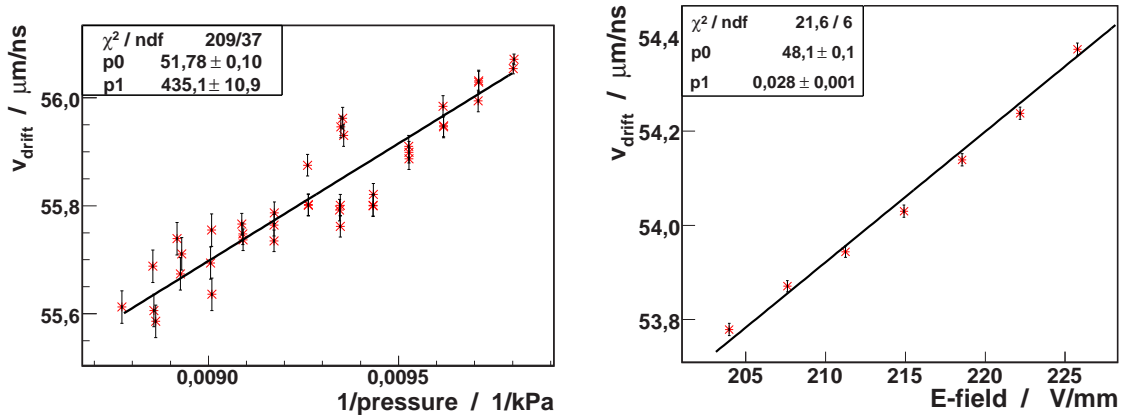
Figure 8.5.: *The drift velocity as a function of the E-field (left) and the inverse pressure (right) for not small E-fields. Both values have been varied by around 10 %. In both curves approximately a linear dependence can be seen.*

In general, the drift velocity can, following Fig. 8.6, approximated as a function of E/p. Thus, to include (limit) variations of the pressure, v_{drift} can be plotted as a function of E/p.
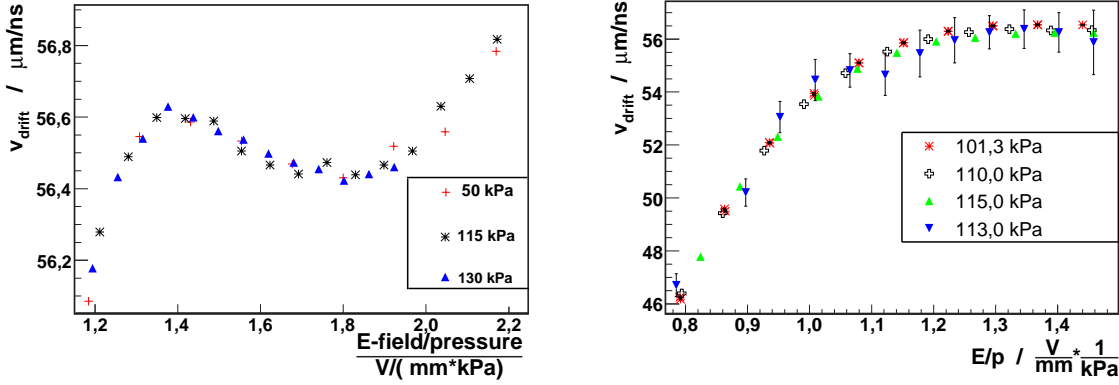
Figure 8.6.: *The drift velocity as a function of E/p. Each curve is plotted for the same pressure and variable E-field. In the Magboltz [Mag02] simulation (left) the deviations between the curves for different pressures are within the errors ($\approx 0,5$ ‰) given by the Monte Carlo integration method of Magboltz. For the measured values (right) this deviation is up to four standard deviations.*

8.3. Effects depending on the Pressure

An increasing pressure leads to a higher density of the gas and thus, in case of contamination of the used gas by oxygen, to a higher density of oxygen impurities. As one can see in Fig. 8.8 and the left part of 8.7, this decreases the signal rate. A larger oxygen density will cause more drift electron attachments in the gas (The average probability for electron attachment in oxygen is about four orders of magnitude higher than in carbon dioxide [Saul77].). The relative oxygen content for this measurement was $\approx 0,4$ ‰. The maximum relative oxygen content in the CMS DT chambers is $0,500$ ‰ [MUO97]. Drift velocities for several gas mixtures have been measured as described in Sec. 8.5. In addition a higher pressure causes more multiple scattering (because of the smaller radiation length, Equ. 4.6) for the β-beams and could lead to a smaller trigger rate.
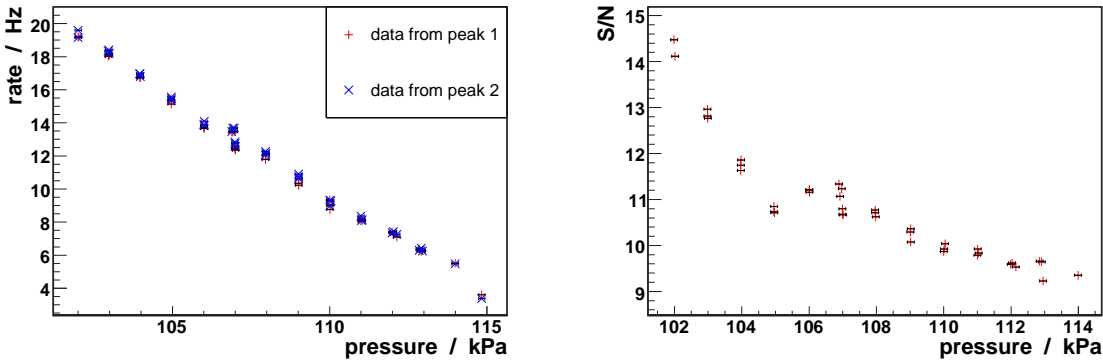
Figure 8.7.: *Left: The rate of triggered anode signals for each peak in the drift time spectrum. The errors are given by a one sigma environment of the gaussian fits. For each pressure value up to three measurements are plotted.*
Right: The signal to "noise" ratio (S/N) as a function of the gas pressure. This "noise" contains any random background and is measured outside the peak region. Same data sample as in Fig. 8.3.

In addition a higher pressure seems to increase the signal to "noise + background" ratio (right part of Fig.8.7). This dependence can be seen directly in the drift time spectra of Fig. 8.8. The number of after pulses seems to be increased by enlarging the pressure.

For the expected pressure variations at CMS ($< 0,3$ kPa) the variations in the rate and the signal to noise ratio of around 20 % do not limit the precision of the VDC. Because the height above sea level at CERN is larger, a lower absolute pressure is expected leading to a higher trigger rate and efficiency.
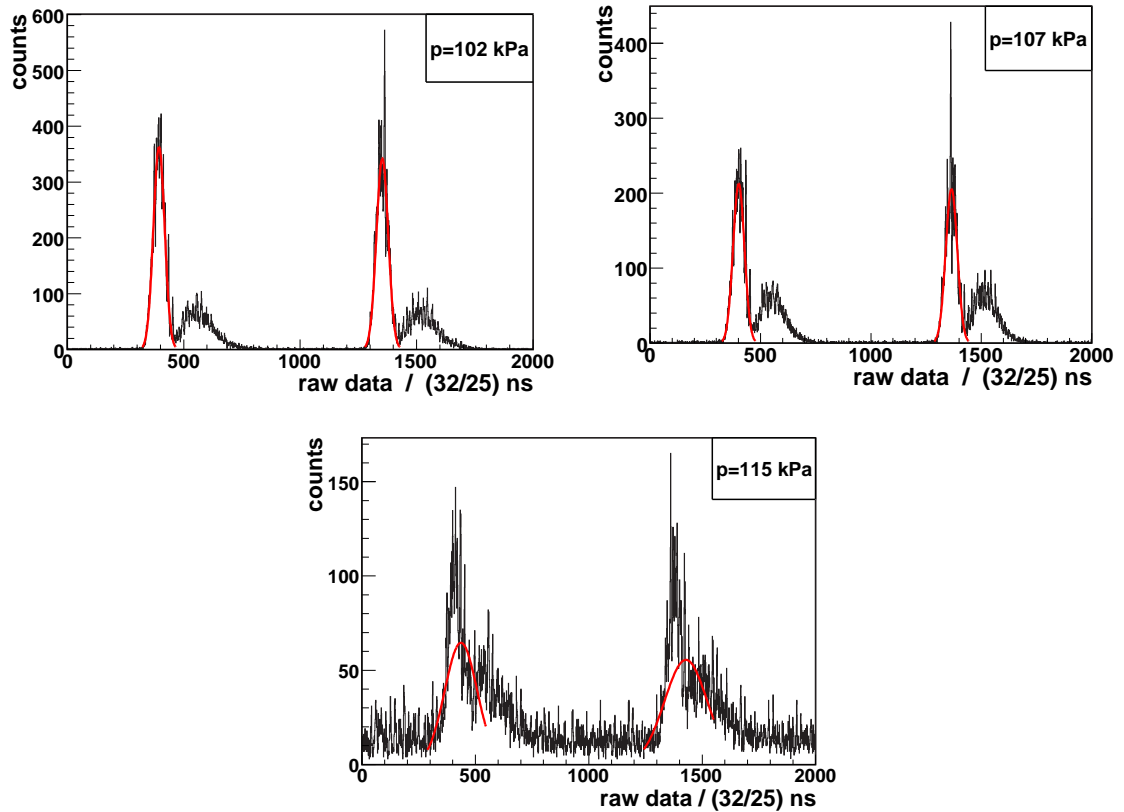
Figure 8.8.: *Drift time spectra for three different pressures (102 kPa, 107 kPa, 115 kPa, 10 min measuring time). At higher pressure more after pulses and a lower signal rate seem to be produced. The rate can be influenced by more drift electron attachment in the gas. The behavior of the after pulses cannot be explained. Same data sample as in Fig. 8.3 and Fig. 8.7.*
Parameters: $E = 212$ V/mm, $U_{anode} = 1,95$ kV, threshold at VDC: 30 mV, VDC digital signal length: 10 ns. Also the after pulse rate at normal pressure (≈ 100 kPa) is increased without having some visible reasons.

8.4. Drift Velocity dependence on Temperature
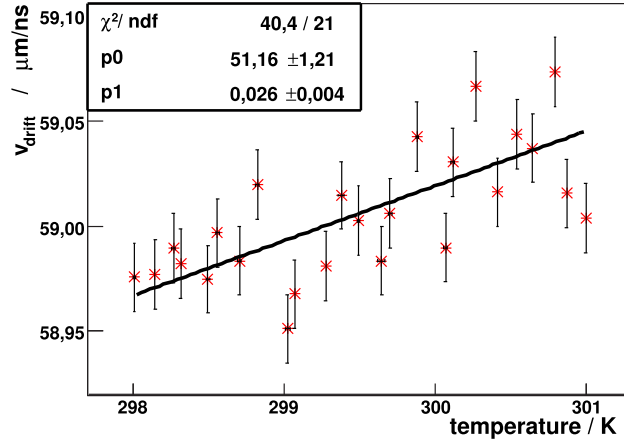
Figure 8.9.: *The drift velocity as a function of the temperature for an E-field of $212\,\text{V/mm}$ ($U_{cathode} = -14\,\text{kV}$): A linear correlation ($v_{drift} = p_0 + p_1 \cdot T$) can be seen. The slope p_1 is $(0{,}026 \pm 0{,}004)\,\mu\text{m ns}^{-1}\,\text{K}^{-1}$, i.e. $\Delta v_{drift}/v_{drift} \approx 0{,}5\,\text{‰/K}$. Cathode voltage and pressure are constant ($\Delta U_{cathode}/U_{cathode} < 0{,}2\,\text{‰}$, $\Delta p/p < 0{,}5\,\text{‰}$)*

Like the pressure the temperature influences the drift velocity (Equ. 4.15) linearly for small E-fields. In Fig. 8.9 v_{drift} is shown as a function of the temperature in the room temperature region for high E-fields. For small temperature variations the linear fit seems to be a good approximation. From the slope $(0{,}026 \pm 0{,}004)\,\mu\text{m ns}^{-1}\,\text{mm kPa kV}^{-1}\,\text{K}^{-1})$ the variation of v_{drift} for temperature in the room temperature region is got (see Chap. 9). Effects of thermal expansion, enlarging the distance between the β-beams, are included in this value. In Fig. 8.10 one can see that plotting v_{drift} as a function of $E \cdot T/p$ does not increase the quality of a linear fit. Because the air temperature fluctuations in the laboratory are very small ($< 1\,\text{K}$), they can be neglected compared to the pressure fluctuations.
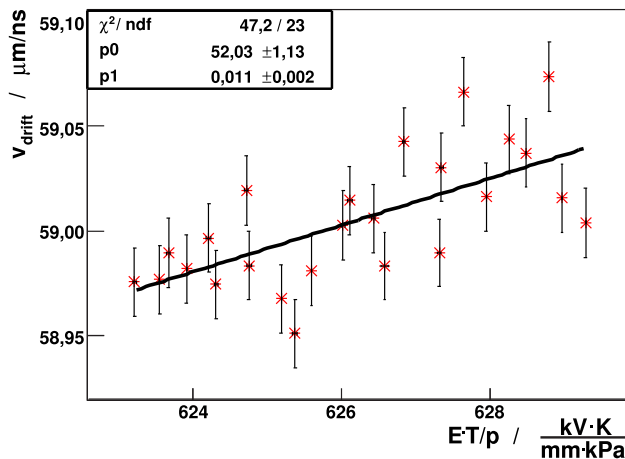
Figure 8.10.: *The drift velocity as a function of $E \cdot T/p$. A linear correlation ($v_{drift} = p_0 + p_1 \cdot E \cdot T/p$) can be seen. The gradient p_1 is $(2{,}02\pm0{,}05)\,\mu\text{m ns}^{-1}\,\text{mm kPa kV}^{-1}\,\text{K}^{-1}$ (same data sample as in Fig. 8.9).*

In general, v_{drift} does not seem to be a function of $E \cdot T$ (Fig. 8.11). But by comparing the right part (v_{drift} as a function of E for three different temperatures) and the left part (v_{drift} as a function of $E \cdot T$ for three different temperatures) of Fig. 8.11, one can see that especially for E-fields above 200 V/mm the deviations between the curves for the different pressure are smaller if v_{drift} is plotted as a function of $E \cdot T$ instead of E. Thus, plotting v_{drift} as a function of $E \cdot T$ can reduce the effects of temperature fluctuation (Sec. 8.7).
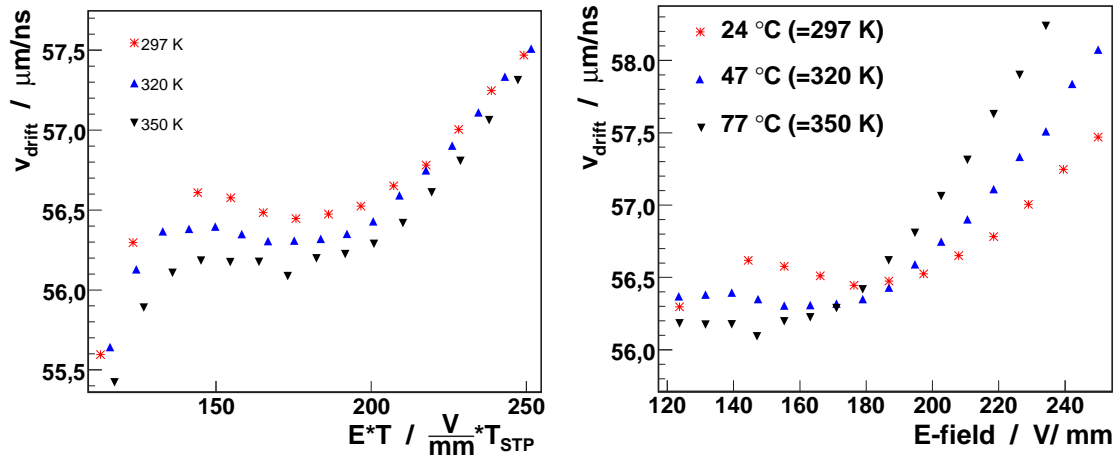
Figure 8.11.: *The drift velocity for different temperatures, simulated with Magboltz [Mag02]. v_{drift} is plotted as a function of $E \cdot T$ (left) and E (right). In the left part the deviation between the values for different temperatures seem to be smaller for E-fields above 200 V/mm*

8.5. Drift Velocity for Several Gas Mixtures

The measurements in Aachen were mostly done with a gas which is used for welding applications: $ArCO_2$ in ratio 85/15 with a nominal purity of 99,7 % and a maximum relative content of 0,08 ‰ H_2O. Assuming that the impurities are air, this leads to around 2,4 ‰ N_2 and 0,6 ‰ O_2. The relative content measured by the O_2-analyzer varies between 0,08 ‰ O_2 and 0,2 ‰ O_2. Because of these variations of the relative O_2-content of the gas bottles and the evolution of the gas tightness of the VDC, the gas purity has changed between the measurements. The relative oxygen content in the VDC was supposed to be the value measured with the O_2-analyzer at the outlet of the VDC. Assuming a contamination with air, the nitrogen content can be calculated from the oxygen content. For some measurements (Fig. 8.12) a bottle of 99,995 % clean gas (called class 4.5) was used. For those measurements the oxygen content at the outlet of the VDC was below 0,03 ‰ O_2. Measurements with $ArCO_2$ with different amounts of impurities have been done.

The deviations from another measurement [Zha94] are all smaller than 5 ‰ (Fig. 8.12) while the deviation from the simulation is up to 20 ‰.

The maximum expected impurity for the gas in the CMS DT-chambers is 0,5 ‰ O_2 [MUO97]. In Fig. 8.13 the measurement of the drift velocity for this (assumed) oxygen content is shown. Again the average deviation from the Magboltz simulation is large (< 10 ‰). Other measurement results have not been found.
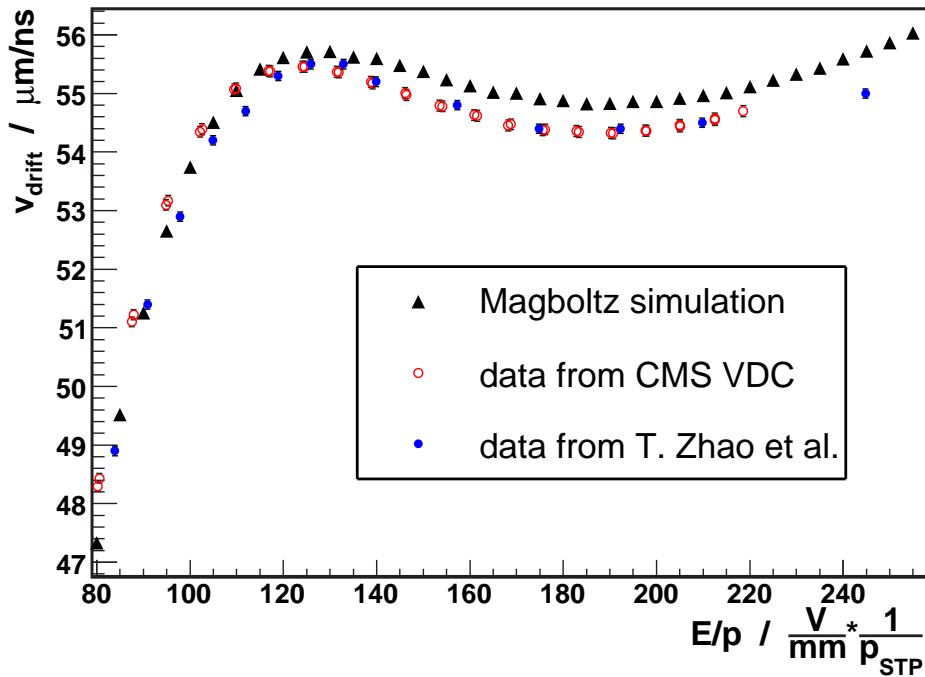
Figure 8.12.: *The drift velocity in clean $ArCO_2$ 85/15 with constant pressure (101,3 kPa):*
A simulation [Mag02] has been compared to the data from the CMS VDC prototype (with
$O_2 < 0,03$ ‰, $N_2 <0,12$ ‰ assuming contamination by air, $\Delta T < 1$ K, $\Delta p < 0,2$ kPa)
and data from T. Zhao et al. [Zha94] (with 99,999 % clean gas).
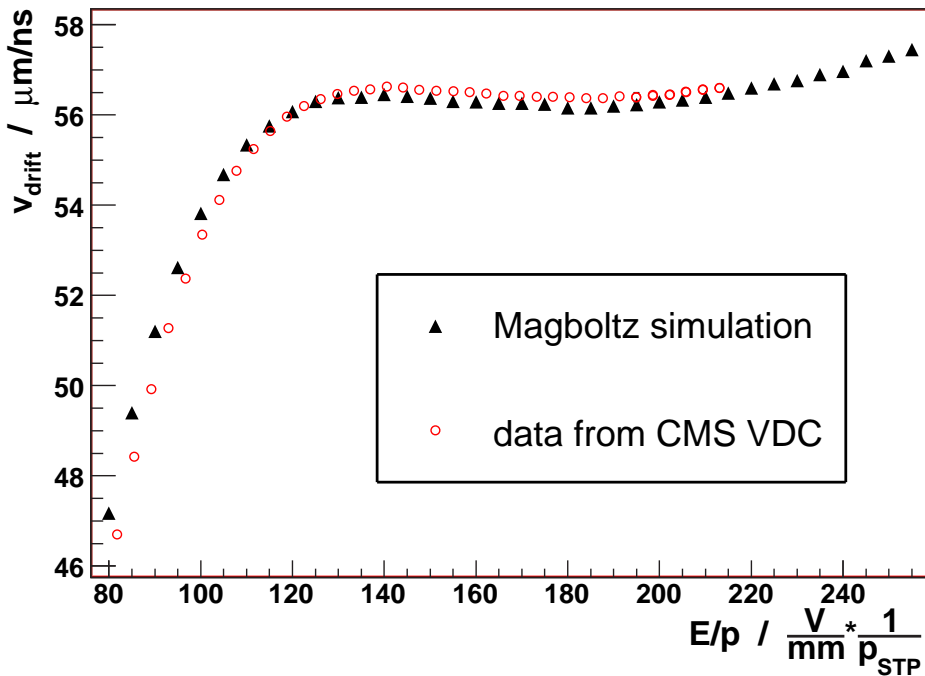*All values for STP=Standard Temperature and Pressure (101,325 kPa, 24 °C).*

Figure 8.13.: *The drift velocity in $ArCO_2$ 85/15 with impurities of 0,5 ‰ O_2 and 2 ‰ N_2 (The*
N_2-content is calculated from the oxygen content assuming a contamination with air.).
Simulation [Mag02] and data ($\Delta T < 1$ K, $\Delta p < 1$ kPa) for STP (=Standard Temperature
and Pressure, here 101,325 kPa, 24 °C).

After some improvements of the VDC prototype for the gas tightness and using a gas bottle with a low content of impurities, an oxygen content of around 0,15 ‰ was measured at the outlet of the VDC. In Fig. 8.14 this measurement is compared to other ones with measured relative oxygen contents of 0,03 ‰ (Fig. 8.12) and 0,5 ‰ (Fig. 8.13). Between the measurements for 0,03 ‰ and 0,5 ‰ O_2 deviations much larger than 10 ‰ in v_{drift} can be seen. This demonstrates the importance of the VDC for the CMS DT gas system: Even within the allowed relative oxygen content of 0,5 ‰, gas impurities affect the drift velocity to an amount that limits the precision of the DT chambers. Between the measurement with a relative oxygen content of 0,03 ‰ and 0,15 ‰ no significant difference can be seen. The reason might be the unknown contamination inside the drift volume:

- The oxygen content is measured at the outlet of the VDC. Between the outlet and the oxygen analyzer there is a (short) tube and some pipes. Leaks there will enlarge the measured oxygen content.

- The distribution of gas impurities coming into the VDC is unknown. Impurities entering the VDC near the gas inlet may have a larger influence than impurities entering the VDC near the outlet.

In addition humidity effects on the drift velocity can not be excluded because there was no humidity analyzer. But with a running air conditioning system, as used in the laboratory, the humidity of the air is low.
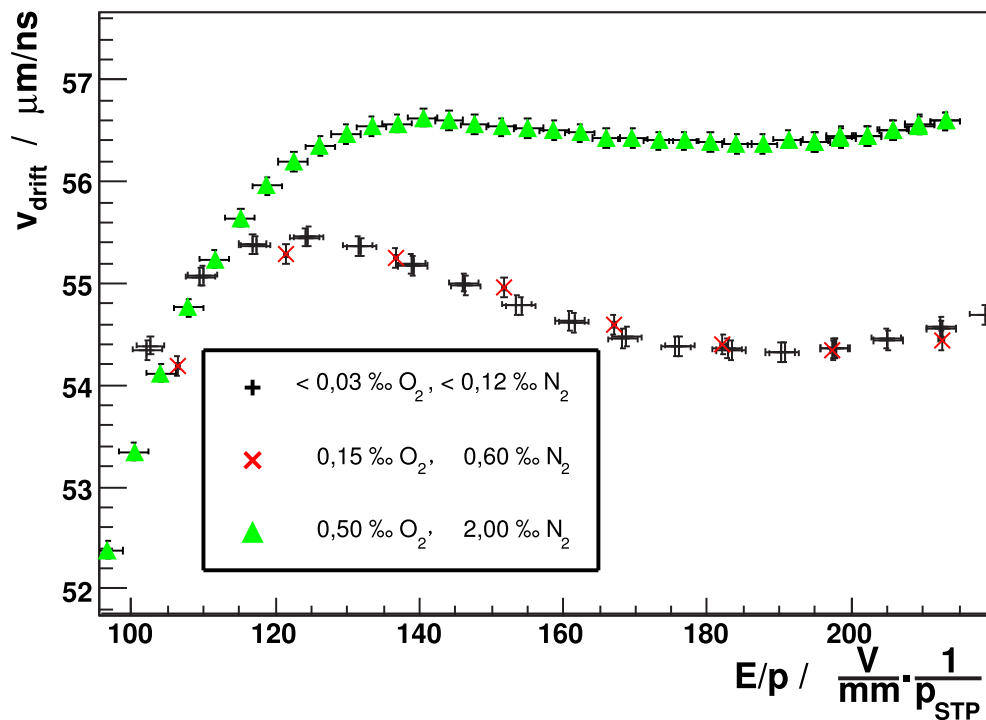
Figure 8.14.: *The measured drift velocity in $ArCO_2$ 85/15 with a relative content of 0,15 ‰ O_2, 0,6 ‰ N_2 and 0,5 ‰ O_2, 2 ‰ N_2 compared to clean Ar/CO_2 (constant pressure). A significant difference can be seen between the clean gas and the other two gas mixtures.*

8.6. Drift Velocity in Magnetic Fields

In the gas control room where the VDCs are located at CMS, a magnetic field from the CMS magnet coil of at most $4\,\mathrm{mT}$ is expected [Rei07]. This could have an influence on the drift velocity and the trigger rate due to deflection of the β-beams or inside the photomultipliers. Although inside the DT chambers there will be at some places a magnetic field, the VDC should measure the drift velocity at $B = 0$ to have a defined value for approximating the drift velocity in the DT chambers. A constant magnetic field will not affect the measurement of the relative drift velocity. But the assumption of a constant magnetic field is not realistic because for some times the CMS magnet is switched off. Also during these periods the VDC should be operated. Simulations of the drift velocity with Magboltz for a magnetic field of $10\,\mathrm{mT}$ showed no significant changes compared to $B = 0\,\mathrm{mT}$ (effects smaller than $0{,}2\,‰$). A linear approximation of the difference between $B = 0$ and $B = 1\,\mathrm{T}$ for $E = 200\,\mathrm{V/mm}$ ($10\,\%$) leads to a value of $1\,‰$ at $10\,\mathrm{mT}$. This is nearly the resolution of the VDC (Sec. 8.7). And a linear approximation of the difference between $B = 0$ and $B = 0{,}1\,\mathrm{T}$ for $E = 200\,\mathrm{V/mm}$ ($1\,‰$) leads to values of $0{,}1\,‰$ at $10\,\mathrm{mT}$.

To measure the effect of the magnetic fields a Helmholtz coil pair was placed around the VDC. With a magnetic field of nearly $10\,\mathrm{mT}$ orthogonal to the drifting electrons inside the VDC and parallel to the β-beams in the VDC no significant change of v_{drift} could be seen (Fig. 8.15). The effect is estimated to be smaller than $0{,}5\,‰$. For the system at CERN, the rack will provide some shielding effect for the magnetic field. Thus, the magnetic field is probably below $2\,\mathrm{mT}$ [Rei07] and the magnetic field should cause no significant changes, estimated to be below $0{,}1\,‰$) of the measured drift velocity.
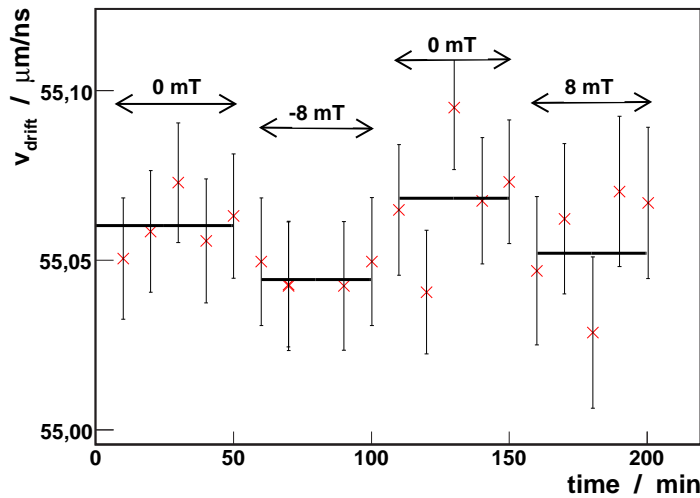

Figure 8.15.: *The drift velocity in a series of measurements with and without a homogeneous magnetic field of around $8\,\mathrm{mT}$ orthogonal to the E-field and parallel to the beams of β-electrons. No significant effect can be seen. ($\Delta T < 1{,}5\,\mathrm{K}$, $\Delta p < 150\,\mathrm{Pa}$, $10\,\mathrm{min}$ per measurement)*

The trigger was influenced by the magnetic field although the photomultipliers were covered with magnetic shielding (μ-metal). The rate drops by around $30\,\%$. By using photodiodes instead of photomultipliers this dependence should be eliminated.

8.7. Long Time Stability

To check if the deviations of several measurements are in the region of the statistical errors a series of consecutive measurements with a duration of 10 min has been done (Fig. 8.16, left). For the whole duration a slope of $(-1,99 \pm 0,75) \cdot 10^{-5}$ µmns^{-1}min^{-1} was fitted. This lead to a difference of $(0,214 \pm 0,081)$ ‰ which is less than the statistical error for one measurement of around 0,8 ‰. The maximum deviation between two consecutive values that should hardly be influenced by changes of temperature, pressure or gas mixture is around two standard deviations. The gas mixture can depend for example on the humidity in the room because of a non perfect gas tightness. A linear fit gives a slope of $(3,58 \pm 1,09) \cdot 10^{-3}$ µm n^{-1}s min^{-1}, with a $\chi^2/ndf < 1,5$. The maximum deviation from the fitted straight line is two standard deviations. All this proves that for short time intervals the fluctuations of the measured drift velocity are within the statistical error.

Plotting the drift velocity as a function of $E \cdot T/p$, as can be seen in Fig. 8.16 on the right, takes into account the fluctuations caused by changes of temperature and pressure. There is no significant deviation between values for the same $E \cdot T/p$, agreeing with the fact that v_{drift} should be a function of E/p. A linear function was fitted (Fig. 8.16, right) resulting in a slope of $(1,99 \pm 0,75) \cdot 10^{-5}$ V K mm^{-1} kPa^{-1} with a satisfactory $\chi^2/ndf < 1,5$. The maximum deviation from the fitted line is two standard deviations. This demonstrates that the fluctuations in v_{drift} for short time intervals are given by the statistical error.
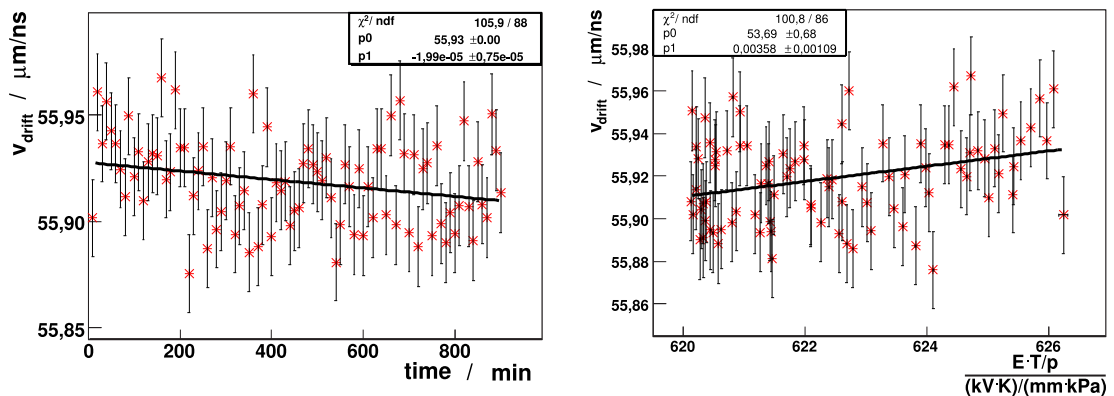
Figure 8.16.: *A series of measurements of the drift velocity with a duration of 10 min each. The small variations are within statistical uncertainties.*

To test the stability of the measured v_{drift} and the whole VDC system in Aachen, a long time measurement of around two weeks (250 h) has been performed (Fig. 8.17, left), subdivided in measurements of 6 h. These measurements were done unattendedly and at normal run parameters ($U_{cathode} = -14$ kV) to simulate the situation while operating at CMS.

Because of the long duration of each run there is much more statistics leading to a very small statistical error of 0,005 µm ns^{-1} (0,1 ‰). Now the maximum deviation between two consecutive values is around ten standard deviations (1 ‰). This is due to the fact that during a 6 h time interval several parameters are changing. The global curve can be explained by looking at the pressure (Fig. 8.17, right). The temperature variations can be neglected. The drift velocity varies between around 55,85 µmns^{-1} and 56,05 µmns^{-1} (~ 4 ‰), the pressure decreases from 101,5 kPa to 99,0 kPa (25 ‰).
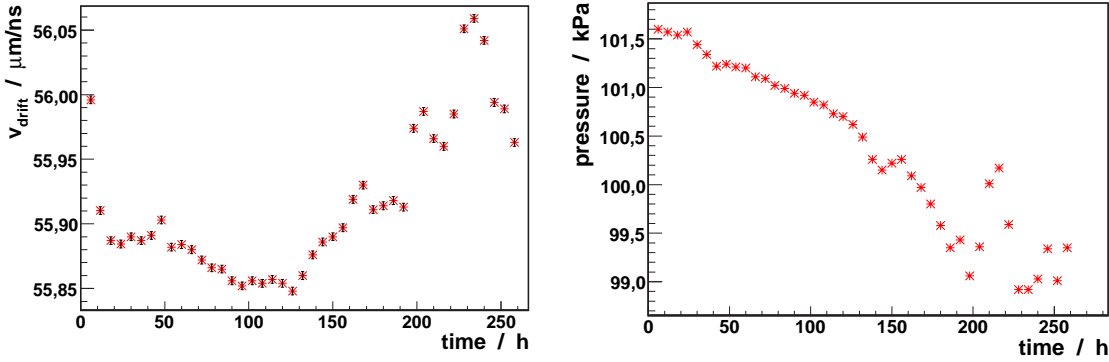
Figure 8.17.: *A long time test of around two weeks for the VDC by running a series of 6 h measurements of the drift velocity. The change of the pressure in the same period is shown on the right.*

Plotting again v_{drift} as a function of $E \cdot T/p$ (8.18), the local deviation, between consecutive values is (except one stray bullet) below 1 ‰. No linear dependence can be seen although the region on the x-Axis is very small and for "good" functions small regions can be linearly approximated. This could indicate that the gas tightness has to be improved to reduce the influence of environmental effects (like a non constant humidity in the room). Hopefully there are no ununderstood effects.

The required relative precision of 10 ‰ has been reached. For the design value of the relative precision of 1 ‰ further studies and improvements (e.g. the gas tightness) are necessary.
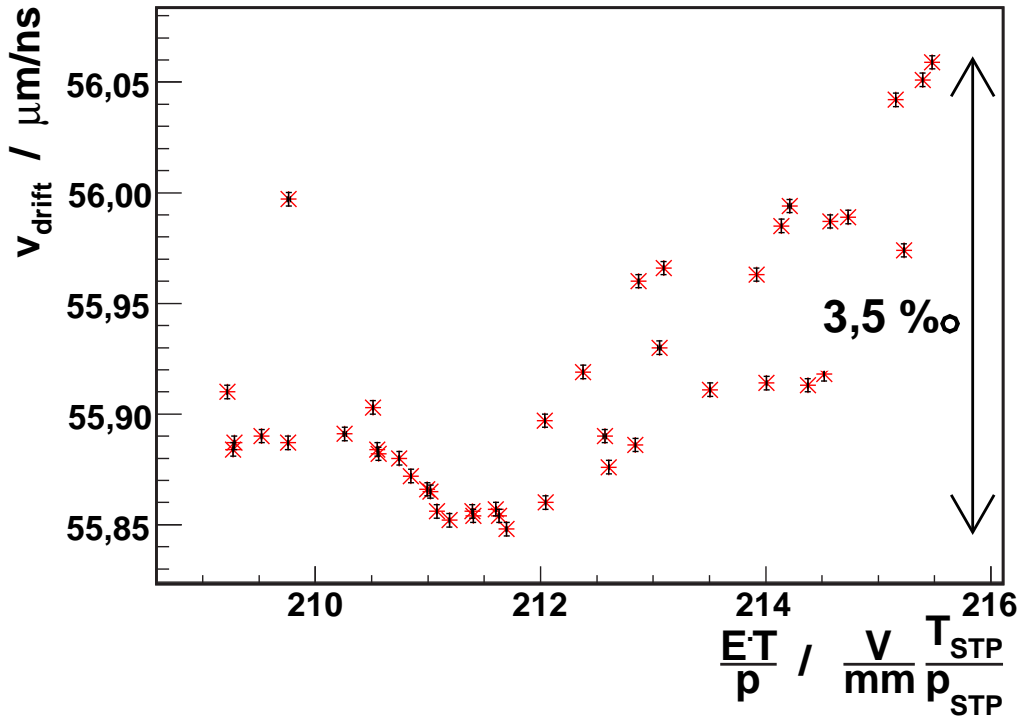
Figure 8.18.: *The long time test of around two weeks for the VDC: The drift velocity is plotted as a function of $E \cdot T/p$.*

9. The Systematic Errors

9.1. Homogeneity of the E-field

The inhomogeneity of the E-field is 1,5 ‰ along the central path of the VDC (Fig. 5.7) and below 3 ‰ at a distance of 4 mm from this symmetry axis [Alt07]. Drifting electrons with a distance larger than 2 mm from the central path cannot reach the anode because of the slit which has a width of 2,5 mm. The transversal diffusion of the drifting electrons reaches about 2 mm[Mag02], meaning that even electrons passing at the border of the slit, i.e. at 1,25 mm from the central path, never were 4 mm away from the central path. Thus, the E-field outside 4 mm from the central path does not affect the measured drift velocity.
Most of the inhomogeneities of the electrical field are symmetrical around the average. Thus, the drift velocity will also have some periodical inhomogeneities around its averages.
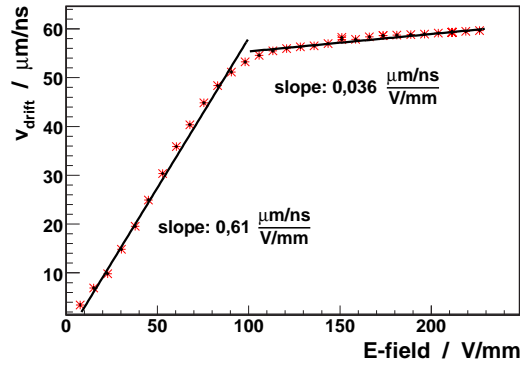
Figure 9.1.: *Fitting straight lines to a measured HV curve (drift velocity as a function of the electric field) to determine the slope.*

The slope of v_{drift} as a function of the E-field is around $(0,036 \pm 0,004) \frac{\text{µm/ns}}{\text{V/mm}}$ for an E-field from 100 V/mm to 230 V/mm and $(0,61 \pm 0,06) \frac{\text{µm/ns}}{\text{V/mm}}$ for an E-field from 8 V/mm to 100 V/mm. Thus, in the worst case assuming the inhomogeneities of the E-field are unsymmetrical this would result in an error at an E-field of 200 V/mm of

$$\Delta v_{drift} = 0,036 \frac{\text{µm/ns}}{\text{V/mm}} \cdot 200 \text{ V/mm} \cdot 0,0003 = 0,021 \text{ µm/ns} \triangleq 0,3 \text{ ‰} \qquad (9.1)$$

and outside the plateau in an error at an E-field of 20 V/mm of

$$\Delta v_{drift} = 0,61 \frac{\text{µm/ns}}{\text{V/mm}} \cdot 20 \text{ V/mm} \cdot 0,0003 = 0,037 \text{ µm/ns} \triangleq 3,7 \text{ ‰}. \qquad (9.2)$$

There are seven oscillations of the E-field around its average between the two slits. Let be assumed that only the inhomogeneities at the borders of the drift volume cause effects to v_{drift} because here the inhomogeneities are not symmetrical and that the inhomogeneities have a linear

impact on v_{drift}. These inhomogeneities affect only 1/7 of the path and hence their impact is reduced by a factor seven. Thus, for a E-field of 200 V/mm, which is the region the CMS VDC has been constructed for, the error caused by inhomogeneities of the drift field is about 0,04 ‰. All following estimations are done for an E-field of 200 V/mm and a v_{drift} of 55 µm/ns. The exact value of the E-field is derived from simulations, since at the moment there are no possibilities to actually measure the E-field with high precision directly, e.g. by using beta beams at more than two positions.

Effects of space charges can be neglected, as shown in [Alt06].

The E-field is also influenced by the mechanical precision and by the values of the resistors of the voltage divider between the grids. Effects of misalignment, up to 20 µm, cause only negligible effects on the homogeneity of the E-field [Alt06]. The electrical resistance between the grids (49 MΩ) has been tuned to a precision of 20 kΩ corresponding to 0,41 ‰. If the electrical resistance between the power supply and the first grid, or between the last grid and the ground, varies by 20 kΩ the change to the E-field at this position is smaller than 1,5 ‰ (calculated from Fig. 6.11 of [Alt06]). A wrong value for the resistance will cause a non symmetrical inhomogeneity of the E-field here. So the error can be estimated, in the same way as the error for inhomogeneities of the E-field with correct resistors, to be smaller than 0,02 ‰. Assuming that four of the eleven values for the electrical resistance have the maximal deviation this error will be enlarged to $\sqrt{4} \cdot 0{,}02$ ‰$=0{,}04$ ‰.

9.2. Electronics Effects

9.2.1. TDC Effects

The systematic error of the time difference measurement of the TDC is around 208 ps (Sec. 7.5). The error Δv_{drift} for the drift velocity is

$$\Delta v_{drift} = \frac{s}{t^2} \cdot \Delta t. \tag{9.3}$$

For a drift velocity of 55 µm/ns this corresponds to an error of

$$\Delta v_{drift}/v_{drift} = \frac{s}{t^2} \cdot \frac{\Delta t}{v_{drift}} = \frac{\Delta t}{t} = \frac{\Delta t}{s} \cdot v_{drift} = \cdot \frac{208\,\text{ps}}{48\,\text{mm}} \cdot 55\,\text{µm/ns} \approx 0{,}24 \text{ ‰}. \tag{9.4}$$

9.2.2. Additional Electronics Effects

Other electronics effects, e.g. run time fluctuations in the discriminators, are canceled when measuring a time difference and thus they have no impact on v_{drift}.

9.3. Mechanical Precision

The mechanical precision of the distance between the middle of the outlet collimators for the beta beams is given by the mechanical precision of the holes for both collimators and the precision of the holes of the collimators (four surfaces) itself. The mechanical precision of one work piece is around 10 µm to 15 µm. Thus, the uncertainty of the slit distance is around $\sqrt{6} \cdot 10$ µm ≈ 25 µm to $\sqrt{6} \cdot 15$ µm ≈ 38 µm. Using a measuring microscope the precision given by the production

could be improved by knowledge. Anyway, effects of thermal expansion must also be accounted for $(48\,\text{mm} \cdot 23{,}8 \cdot 10^{-6}\,\text{K}^{-1} \cdot 5\,\text{K} \approx 6\,\mu\text{m})$. An error of $30\,\mu\text{m}$ leads to a relative variation of the measured drift velocity

$$\frac{\Delta v_{drift}}{v_{drift}} = \frac{25\,\mu\text{m}}{48\,\text{mm}} \approx 0{,}6\text{\textperthousand}. \tag{9.5}$$

9.4. Trigger System Effects

There are three parts of the trigger system which can generate differences in time, from the point of time when a beta electron leaving the VDC penetrates the scintillator until a signal is sent to the TDC:

1. Runtime fluctuations of the scintillation light inside the scintillator

2. Runtime fluctuations inside the photodetectors

3. Runtime fluctuations within the electronics (amplifiers, discriminator, cable lengths, ...)

The runtime fluctuations in the scintillator are very small. In a scintillator with a refractive index of 1,6 light can propagate up to an angle of around $45°$ to one surface without loss. Thus, the total path length for a distance of $150\,\text{mm}$ from the point of hitting beta beams to the farthest end is smaller than (Chap. 6) $\approx 0{,}8\,\text{ns}$. Simulations have shown that the runtime fluctuations of the light are smaller than $150\,\text{ps}$, which can be neglected for an amount of 10000 data points. This error would also have only been a statistical error. Measurements of the run times have not been done with the TDC because the time difference between the arrivals of the light created by one beta electron at the two photomultipliers would have to be measured. This would have required more than one TDC channel for readout, which was not available at this time. In addition, the TDC has a resolution of only $800\,\text{ps}$. A measurement was done using the oscilloscope (Fig. 6.9) and led to a runtime difference of $200\,\text{ps}$.

The photomultipliers have a time resolution (FWHM) of around $500\,\text{ps}$ [Rei07][1]. For 10000 signals that results in an error for v_{drift} of $0{,}006$ \textperthousand. In case of using photodiodes this error can be reduced by a factor 1,5. Then there is an additional error of the preamplifiers. Their signal rise time is $< 1\,\text{ns}$ [Pho06]. Assuming a pulse amplitude of $150\,\text{mV}$ and a threshold at the discriminator of $100\,\text{mV}$, for fluctuations of the threshold or the signal of $5\,\text{mV}$ this causes a maximum error of $1/30\,\text{ns}$ corresponding to $\Delta v_{drift}/v_{drift} \approx 0{,}04$ \textperthousand.

Propagating time variation in the preamplifiers of assumed maximal $100\,\text{ps}$ would lead to $\Delta v_{drift}/v_{drift} \approx 0{,}1$ \textperthousand.

9.5. Effects of Environment Values

9.5.1. Temperature

The upper limit and lower limit specification for the error of the temperature sensor is $\pm 0{,}5\,°\text{C}$ at most, but the typical error (in the room temperature region) is below $0{,}1\,°\text{C}$ [Dal07]. The measured temperature variation during one hour is below $0{,}1\,°\text{C}$ and during one day is (because of the air conditioning) below $0{,}5\,°\text{C}$. The influence of the temperature on the drift velocity (Sec. 8.4)is $0{,}026\,\mu\text{m}\,\text{ns}^{-1}\,\text{K}^{-1}$. For an error of $0{,}5\,\text{K}$ this causes an error $\Delta v_{drift}/v_{drift}$ of around $0{,}2$ \textperthousand.

---

[1]measured by using two pairs of PMs connected to one scintillator and comparing the coincidences of both pairs

9.5.2. Pressure

The measurement of the relative pressure is very precise ($< 0{,}01 \mathrm{kPa}$). The fluctuations during short measurements ($< 1\,\mathrm{h}$) are much smaller than $0{,}1\,\mathrm{kPa}$. The absolute pressure measurement is less precise because the pressure device used for this had not been calibrated for a long time. Thus, it has been tried to calibrate it using informations from a nearby whether station [RWTH06]. Using this, the assumed absolute precision of the pressure measurement is $0{,}1\,\mathrm{kPa}$. The effect of the pressure on to the drift velocity (Sec. 8.2) is $2{,}02\,\mu\mathrm{m}\,\mathrm{ns}^{-1}\,\mathrm{kPa}^{-1}$. This causes an error $\Delta v_{drift}/v_{drift}$ of around $3{,}7$ ‰. Using the precision for the relative pressure measurement $\Delta v_{drift}/v_{drift}$ is around $0{,}37$ ‰.

9.5.3. Gas Flow

The error of the gas flow is between $5\,\%$ to $10\,\%$. Effects of the gas flow related to the flow of incoming impurities into the VDC have not been considered.

9.5.4. Magnetic Fields

No effect of magnetic fields up to $10\,\mathrm{mT}$ to the drift velocity could be measured. Errors derived from simulations are smaller than $0{,}1$ ‰ for $B < 4\,\mathrm{mT}$, which is the maximum expected value at the location of the VDCs at CMS.

9.5.5. Cathode Voltage

The measured standard deviation is around $2\,\mathrm{V}$. The nominal resolution of the power supply is $4\,\mathrm{V}$ [Caen07]. A controlling measurement with a second voltmeter could not be done. Assuming an absolute error of $5\,\mathrm{V}$ ($0{,}36$ ‰, calculated as in Sec. 9.1), the error of the drift velocity is $0{,}05$ ‰. HV flashovers, which warp the drift field, take place only in a very small fraction of the readout time. Additionally created drift electrons are uniformly distributed in time and hence do not contribute to systematic errors.

9.5.6. Anode Voltage

For a working area of $250\,\mathrm{V}$ around the working point for the anode voltage the change in the drift velocity (Tab. 7.1) is around $0{,}50\,\mu\mathrm{m/ns}$ according to around 10 ‰. This error dominates all other errors. This effect needs further analysis for the mass production VDCs. For the relative v_{drift}-measurement and a precision of the anode voltage of $2\,\mathrm{V}$ the relative error $\Delta v_{drift}/v_{drift}$ is smaller than $0{,}04$ ‰.

9.6. Summary of Errors

Not all systematic errors that are listed here (Tab. 9.1) increase the uncertainty of a measurement, as needed to monitor changes in the drift velocity. In the future, for using the measured drift velocity also for the track reconstruction in the CMS DT chambers, also the precision of the absolute drift velocity is important.

	effect on v_{drift} in $10^{-3}\,\mu m/ns$	effect on v_{drift} in ‰	comment
inhomogeneities of E-field	2,2	0,04	
uniformity of electrical resistance	2,2	0,04	
electronics	13.1	0,24	
mechanical precision	33	0,6	
trigger system	5,9	0,11	
temperature measurement	11,0	0,2	
pressure measurement	20,2	3,7	will be improved
B-field	5,5	0,1	only at CMS
cathode voltage	2,75	0,05	
anode voltage	2,2	0,04	needs further analysis
anode pulse shape ($U_{cathode}$)	NA	NA	

Table 9.1.: *All estimated maximal systematic errors for the **absolute drift velocity measurement** at assumed values of around: $E = 200\,V/mm$, $U_{cathode} = -14\,kV$, $U_{anode} = 1,9$ kV and $v_{drift} = 55\,\mu m/ns$. For the error caused by the anode voltage see the text.*

The error cause by the dependence of v_{drift} on the anode voltage is around 10 ‰. If this effect is also present for the series production chambers this will be the dominating error for the measurement of the absolute drift velocity.

Neglecting this effect of a not fixed anode voltage and pulse shape variations, the sum of squared errors[2] is $< 3,8$ ‰. With a perfect calibrated pressure measurement device the error would be reduced to $< 0,8$ ‰.

	effect on v_{drift} in $10^{-3}\,\mu m/ns$	effect on v_{drift} in ‰	comment
temperature measurement	5,5	0,1	
pressure measurement	5,5	0,37	
cathode voltage	2,75	0,05	
anode voltage	2,2	0,04	needs further analysis
anode pulse shape (E-field)	NA	NA	

Table 9.2.: *All estimated maximal systematic errors for the **relative drift velocity measurement** at assumed values of around: $E = 200\,V/mm$, $U_{cathode} = -14\,kV$, $U_{anode} = 1,9$ kV and $v_{drift} = 55\,\mu m/ns$. The other systematic errors nearly cancel for relative drift velocity measurement.*

---

[2]assuming the errors are statistically independent

9. The Systematic Errors

The sum of squared systematic errors for a measurements of the relative drift velocity (Tab. 9.2) is 0,4 ‰.

total systematic errors	3,8 ‰ without effects of non fixed anode voltage (0,8 ‰ for perfect calibrated pressure measurement device)
systematic errors for relative measurements	0,4 ‰
statistical errors for 10000 events (4 min measurement)	0,4 ‰

Table 9.3.: *Summary of errors.*

By comparing the data from several series production VDCs most of the systematic error for the absolute and relative measurement of v_{drift} can be measured. This can be done before the VDCs are delivered to CMS.

Summary:
For the basic operation of the CMS VDCs, the monitoring of the drift velocity, meaning the measurement of the relative drift velocity, the systematical error are estimated to be below 0,4 ‰ (Tab. 9.3). A statistical error of 0,4 ‰ is achieved in less than 4 min (Appendix D).
For a measurement of the absolute drift velocity the effects of the anode voltage need further analysis. Neglecting this at CERN the absolute drift velocity can be measured with a precision of 0,8 ‰.

10. Summary and Outlook

Starting with the prototype chamber for drift velocity measurements (VDC), several improvements were done to the chamber using the experiences from the first measurements. During these tests the physical characteristics of the chamber have been determined. By systematic measurements, optimal run parameters have been determined and the foundation for the series production was set.

Measurements of the drift velocity for different parameters have shown that the results for the drift velocity in Ar/CO_2 (85/15) agree with results from a published measurement. Dependences of the drift velocity on pressure and temperature have been measured, which can be useful for the DT chamber gas system at CMS as well.

The statistical error of the VDC ($< 0,5$ ‰ in v_{drift} for a $5\,\mathrm{min}$ measurement) is very small for the current trigger system. Therefore comparisons of the drift velocity during short time intervals can be made, which have shown that the stability of the drift velocity is at the level of 1 ‰. A long term uninterrupted test, measuring over a period of two weeks, showed similar results.

Some measurements seem to be influenced by a non optimal gas tightness of the chamber. For the series production this problem is being fixed.

The systematic errors for measurements of the drift velocity are estimated to be smaller than 1 ‰. Comparing the result of several VDCs it will be possible to measure most of these uncertainties directly.

The measurements for relative contents of 0,03 ‰ and 0,5 ‰ O_2 showed deviations much larger than 10 ‰ in v_{drift}. This demonstrates the importance of the VDC for the CMS DT gas system: Even within the allowed oxygen content, gas impurities affect the drift velocity to an amount that limits the precision of the DT chambers.

Another important part of the VDC system is the trigger system. The results show that a compact trigger system using silicon photomultipliers could be a realistic and promising candidate for the trigger system, featuring several advantages WRT the present photomultiplier-based one. The schedule is to deliver a fully operating system of six VDCs to CMS in time of the first test of the whole CMS detector foreseen at the end of 2007.

After the successful positive tests (gas tightness and HV robustness) of VDCs the delivery of six VDCs to CMS in summer 2007 is foreseen. For the complete VDC system some work on the read out software, the electronics and the trigger system still has to be done.
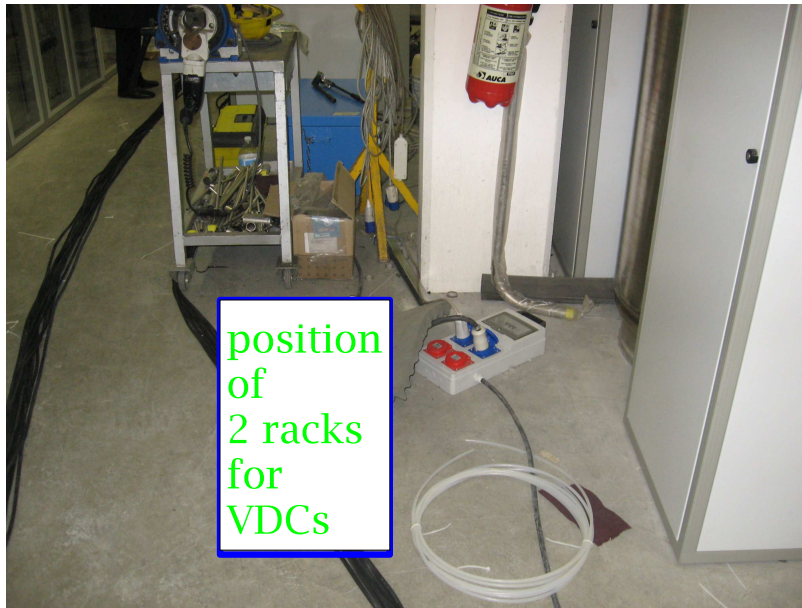
Figure 10.1.: *The position in the USC gas room where the racks with the VDCs are going to be installed. Just an empty piece of floor at the moment ...*

A. Description of the Functionality of Plastic Scintillators

In a plastic scintillator a material with benzene rings, the primary scintillator, with a relative mass content of around 1%, is added to a substrate. Those have deallocated π-orbitals. The electronic ground state is called S_0. The higher singlett states are called $S_1, S_2, \ldots$. There are also triplet states (two electron in spin1-configuration) denominated with $T_0, T_1, T_2, \ldots$. Decay from T_0 to S_0 is prohibited by spin selection rule $\Delta S = 0$. Each state is divided into several vibrational and rotational states. The process follows this scheme (see Fig. A.1):

1. A traversing particle excites π-orbitals[1]. The electrons are exited into the electrical states S_1 and higher (eV range corresponding to light with a wave length of $300\,\text{nm}$ to $600\,\text{nm}$) states combined with vibration states ($0{,}1\,\text{eV}$ range). The energy is transformed into phonons (Förster processes).

2. S_2 and higher states decay without emitting radiation into the state S_1 (*internal degradation*).

3. The state S_1 decays under fluorescent emission of light. This is the scintillation light.

4. The probability that a state S_1 does not decay in the ground state S_0 but into an exited vibration substate is very high.

The emitted light has not enough energy to excite electrons from the ground state S_0 to the first excited state S_1 because the energy was lost in form of vibrational ΔE. Thus, the emitted light is not absorbed itself in the scintillator, the material is transparent for its own light [Kra05].
In addition, triplet states T_i can be excited including excited vibration states. The T_1 and higher states decay without emitting radiation into the ground state T_0, a metastable state. Direct decays from T_0 into S_0 are not allowed because of the spin selection rules.
Instead, exited molecules in T_0 states interact with other molecules in state T_0 ($T_0 + T_0 \rightarrow S_0 + S_1 + phon$
This process leads to a phoshorent emission of light [Kra05].

---

[1] π-orbitals are occupied by two electrons
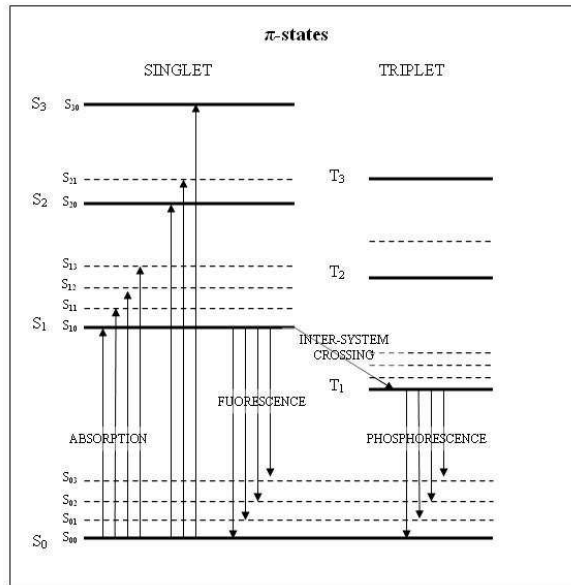
Figure A.1.: *Energy states and transitions in an organic scintillator [Wik07].*

B. The Root Analysis Software

The offline analysis software for the data from the VDC system (in Aachen) was the most time-consuming work for the VDCs. The software was designed to calculate the drift velocity from the raw data, to get all additional data (e.g. pressure date), to calculate composed values and to write an output file for the analysis. For making plots and histograms another program is used which reads the analysis output files. The software should do all this for several raw data files automatically.

The Data File Format for the Raw Data

The raw data include the time informations from the TDC from which the drift velocity is created. This is the largest part of the data. Additional the read out data from all the sensors (pressure, temperature), time information for the measurement and information about manual setting (threshold at discriminators, gas flow, ...) are written here. Because the data for the HV supply (cathode and anode) are taken by another PC these data are written to another file which is integrated into the first file offline.

Shortened example of a raw data file:

```
// header block containing general informations
$$FILENAME vdc_060324_1500.txt          // 1 space between key word and value
$$TDC_READOUT_MODE GATED_MODE
//comments are possible everywhere
$PROGRAMMED_STARTTIME 15:00:00
$PROGRAMMED_ENDTIME 18:00:00
$PROGRAMMED_VOLTAGE_AT_CATHODE_IN_V 15000
// unit are added to the value name
$STARTDATE 20060324
$STARTTIME 15:00:00.000
// 2 empty lines after header and before end block
//
$BEGIN_BLOCK_VDC1     // one block for each VDC
$ELAPSED_TIME_IN_S 000000.000      // this block in certain time intervals
$TEMPERATURE_IN_K 293.00           // always try to use SI basic units
$NUMBER_OF_TRIGGER_SIGNALS 000333355
$END_BLOCK_VDC1
//1 empty line before and after data block
$BEGIN_DATA
$DATA_HEADER 3 t_anode_VDC1 t_PM1_VDC1 t_PM2_VDC1
$DATA_UNIT 3 ns*25/32 ns*25/32 ns*25/32
```

```
$DATA_CHANNELS 3 _000 _001 _009        // channels read; from 000 to 127
625_000 670_000 46_001 47_009          // comments also allowed within data block
// Note: 1 line per event; this is the long part of the file...
// Note that for an event the TDC data may contain
// 0, 1, 2, ... entries in any channel,
// which with the proposed format are easily recognized and identified.
// Any other variable value can also be identified
// via the user-defined "data_channel"
// name (it is in reality a character string appended to the numerical value).
$$END_DATA
//
$$ELAPSED_TIME_IN_S 000000.000
$$TEMPERATURE_IN_K 293.00
$$NUMBER_OF_TRIGGER_SIGNALS 000333355
//
// endblock
$ENDTIME 18:00:00.000
$END_OF_FILE
```

Class Description

DataRead: Loads all VDC raw data files in the directory.
Detect data: Finds the data blocks. The TDC data are filled into histograms. The additional data are sent to the "Detect signal values" class.
Detect signal values: Sorts the additional data using the signal words marked with a $.
Comments: Removes the comments from the data and puts them into a list.
Peak Search: Analyzes the data in the histograms. The two peaks in the drift time spectrum are searched and analyzed.
Statistics: Calculates statistical values from C++-vectors.
Tools: E.g. can transform numbers to strings.
Dataoperations: Can move one then entries in one peak of the drift time spectrum to the position of the other peak.
Data output: Collects all values and writes the analysis output file.

Analyzing the Data

As the first step in the drift time spectrum, the highest value averaging over few (five) values is searched. The second step is finding the second highest value. Both values are assumed to be the maximum of the two peaks corresponding to the signals from the two radioactive sources. By searching the first value on the left and on the right of those maximums which is smaller than two times the average value a first set of borders for a gaussian fit is get. Then the gaussian fit is done iteratively by using the mean $\mu \pm 3\sigma$ as new peak borders. If this algorithms has been converged the last parameter set is used and the mean μ is used for the peak time.

Data Output File Format

For the analysis data output a flexible human readable Unicode (uft8) text file data format was chosen. The data are sorted in block groups by "families" of values like pressure data, timing data etc. The block are in tabular forms where in the lines the date is sorted by the number of the measurement and the number of the VDC.

Shortened example of analysis data output format:

```
$FILENAME VDC_analysis_20061020_1915.txt
$STARTTIME 19:15 // start time of the first measurement
$ENDTIME 17:00 // end time of the first measurement
$NUMBER_OF_FILES 2 // =number of measurements
//
//  2 empty lines
$\$BEGIN_FILENAMES        // list of all analyzed files (=measurements)
001 vdc_20060817_0907.txt // all data values are sorted by the filenames
002 vdc_20060817_0920.txt
$END_FILENAMES
// -------------------------------------------------------------------------------
// BEGIN_EXPLANATIONS BLOCK
// STRUCTURE:
// - In any block evaluated data of similar values are listed by their numbers
//   given by their filenames and then by the number of the VDC
//   (1 to 6 , p=prototype)
// - In the header of each block the values are named
//   in the form "value_kind_suffix(_suffix)".
// - Values are (usually) physical values, the kind is the corresponding device
// LETTERS:
// - values (prefix): t=time, p=pressure, U=voltage, I=current, R=rate,
//   T=temperature, E=electrical field
// - E=errors: this suffix makers the error for a value
// _PROG = suffix for programmed values
// END EXPLANATIONS BLOCK
// -------------------------------------------------------------------------------
$BEGIN_DATA
// 1 empty line
// informations about the real runtime of the measurements
$BEGIN_TIMING_DATA
$DATA_HEADER 04 STARTDATE  STARTTIME ENDDATE    ENDTIME  DURATION
$DATA_UNITS  04 date       time      date       time     s
001             2006/08/17 09:07:00  2006/08/17 09:17:00 600
002             2006/08/17 09:20:00  2006/08/17 09:27:00 600
$END_TIMING_DATA
//
$BEGIN_DRIFT_VELOCITY_DATA
```

```
$DATA_HEADER 08 U_CATHODE U_CATHODE_E       E   E_E VDRIFT VDRIFT_E
$DATA_UNITS  08          V           V    V/mm V/mm µm/ns  µm/ns
001          1  11050.22          1.52 231.32 0.22 55.232 0.056
001          2  11000.33          1.22 200.23 0.32 55.263 0.026
002          1  11050.22          1.52 211.37 0.22 55.232 0.056
002          2  11000.33          1.22 200.43 0.32 55.263 0.026
$END_DRIFT_VELOCITY_DATA
//
$BEGIN_PRESSURE_DATA
$DATA_HEADER 06 p_INSIDE p_INSIDE_E   p_ROOM p_ROOM_E
$DATA_UNITS  06      kPa        kPa      kPa      kPa
001          1 101.4452      0.013 100.2342    0.007
001          2 101.4652      0.012 100.2742    0.010
002          1 101.4452      0.013 100.2342    0.007
002          2 101.4652      0.012 100.2742    0.010
$END_PRESSURE_DATA
//
$END_DATA
//
//  2 empty lines
$END_OF_FILE            // no empty lines at end of the file
```

C. Electronics
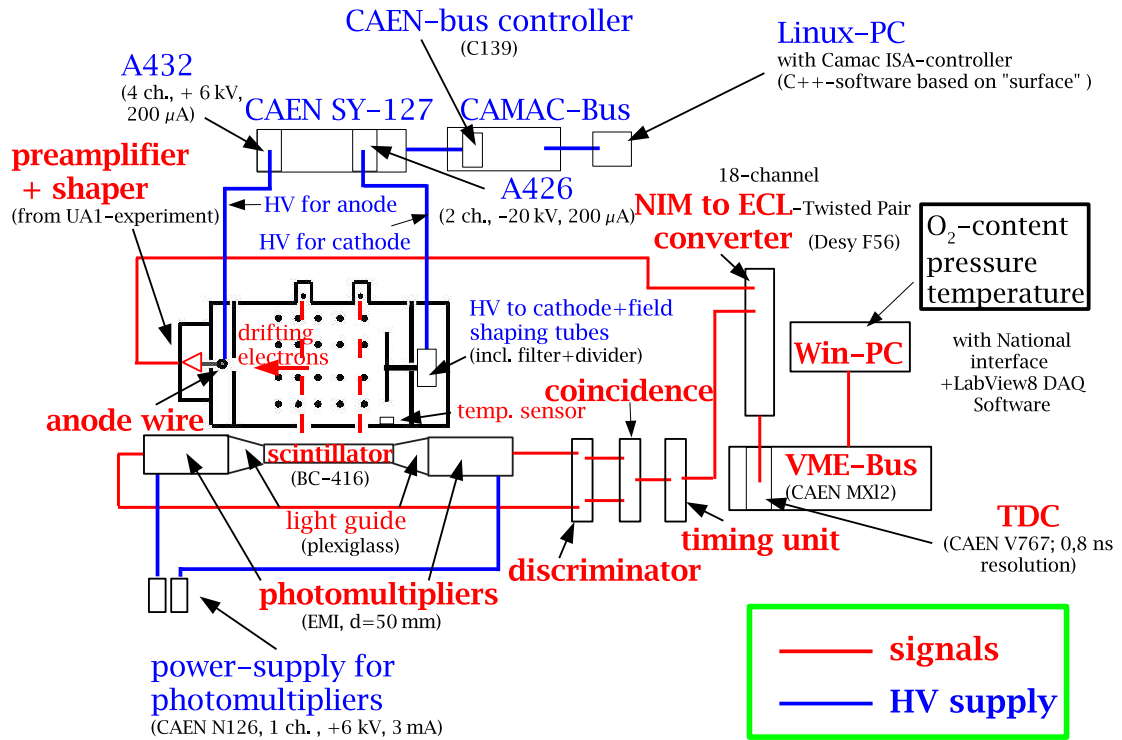
Figure C.1.: *The electronic system used for the VDC prototype: readout system, HV supply and gas control.*
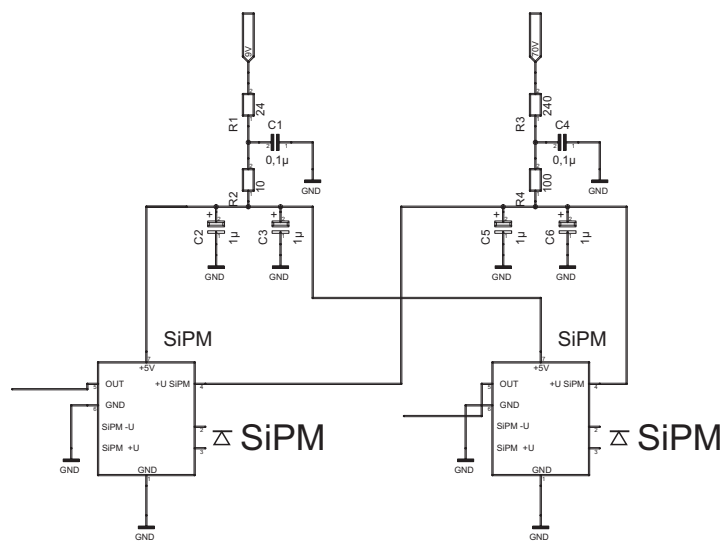
Figure C.2.: *The electrical setup of the "U"-form fiber trigger setup [Bru07, Ada06, Hil07].*

Figure C.3.: *The front plates of the designed VME-modules for the final VDC system at CERN [Hil07].*

D. Systematic Effects in Statistical Errors

The statistical errors depend on the amount of data contained in the two peaks of the drift time spectrum. The error of the gaussian fit resulting in an estimate of the mean μ depends on the width σ of the peak and the number N of data points inside the peak. (For the tails of the peaks a 3σ environment is assumed because for a gaussian distribution the amount of data outside this environment is only 0,27 %.) The error $\Delta\mu$ of the mean of the drift time, is given by

$$\Delta\mu = \frac{\sigma}{\sqrt{N}}. \tag{D.1}$$

In Fig. D.1 the statistical errors are plotted as a function of the cathode voltage (corresponding to the electrical field). Because the drift velocity is calculated from the mean times t_1, t_2 of the two peaks and the slit distance s by

$$v_{drift} = \frac{s}{t_2 - t_1}, \tag{D.2}$$

the corresponding error is

$$\Delta v_{drift} = \sqrt{\left(\frac{1}{t_2 - t_1} \cdot \Delta s\right)^2 + \left(\frac{s}{(t_2 - t_1)^2} \cdot \Delta t_1\right)^2 + \left(\frac{s}{(t_2 - t_1)^2} \cdot \Delta t_2\right)^2}. \tag{D.3}$$

Setting $\Delta t_1 = \Delta t_2 = \Delta t$

$$\Delta v_{drift} = \sqrt{\left(\frac{1}{t_2 - t_1} \cdot \Delta s\right)^2 + \left(\frac{2s}{(t_2 - t_1)^2} \cdot \Delta t\right)^2}. \tag{D.4}$$

Setting the systematic error Δs to 0 to isolate the statistical errors:

$$\Delta v_{drift} = \left|\frac{2s}{(t_2 - t_1)^2} \cdot \Delta t\right| = 2v_{drift}^2 \cdot \frac{\Delta t}{s}. \tag{D.5}$$

For a constant Δt the error Δv_{drift} of the drift velocity decreases with an increasing $t_2 - t_1$. Thus, Δv_{drift} should increase with v_{drift}. This can be seen by comparing Fig. D.1 to a plot where v_{drift} is shown as a function of $U_{cathode}$ (or E-field, e.g. Fig. 8.2).
In addition to this, the relative change of the peak width $(\sigma_{max} - \sigma_{min})/\sigma$ (Fig. 7.28) is smaller than 25 %. Following Equ. D.1, the statistic error can be reduced by taking more statistics. To achieve a statistical error $\Delta_{vdrift, \, stat}$ smaller than the systematical error $\Delta_{vdrift, \, sys}$, N has to be large enough. Inserting Equ. D.1 into Equ. D.5 results

$$N = \frac{4v_{drift}^2}{\Delta v_{drift}^2 \, s^2} \cdot \sigma^2. \tag{D.6}$$

For $\Delta_{v_{drift}, \, sys} < 0,4$ ‰ (Sec. 9.6), $s = 48\,\text{mm}$, $\sigma = 17\,\text{ns}$ (at $200\,\text{V/mm}$) and $v_{drift} = 55\,\mu\text{s/ns}$ the requirement $\Delta_{v_{drift}, \, stat} < \Delta_{v_{drift}, \, sys}$ is achieved for $N \gtrsim 10000$. For a trigger rate of $50\,\text{Hz}$ this can be reached in less than $4\,\text{min}$.

D. Systematic Effects in Statistical Errors
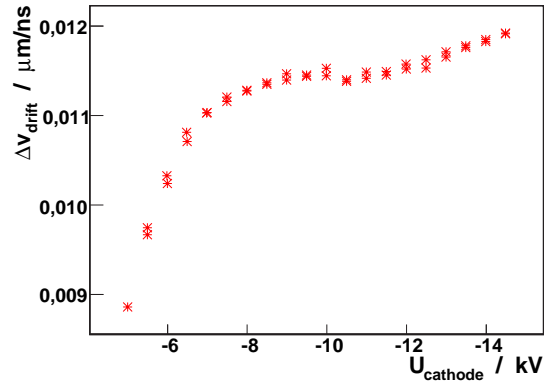
Figure D.1.: *The measured statistical error of v_{drift} as a function of the cathode voltage $U_{cathode}$. Note that the statistics contained within each measurement point of $U_{cathode}$ are similar (differences $< 10\%$).*

All effects of multiple scattering (Sec. 4.1.3), δ-electron production (Sec. 4.4.3) and diffusion (Sec. 4.2) have the same impact on data from both beta beams. Thus, their effects are included in the statistical errors.

Bibliography

[Ada06] Franz Adamczyk, 2007. III. Physikalisches Institut A, RWTH Aachen, *private communication*

[Alt06] George Altenhöfer, *Development of a Drift Chamber for Drift Velocity Monitoring in the CMS Barrel Muon System*, May 2006. Diploma Thesis, III. Phys. Inst. A, RWTH Aachen.

[Alt07] Georg Altenhöfer, 2007. III. Physikalisches Institut A, RWTH Aachen, *private communication*

[Altas94] Atlas, *Technical Proposal for a General-Prupose pp Experiment at the Large Hadron Collider at CERN*

[Art06] A. Artikov et al. *New generation large area muon scintillation counters with wavelength shifter fiber readout for CDF*. `http://www1.jinr.ru/Pepan_letters/panl_3_2006/07_artikov.pdf`

[BC05] Saint Gobain Crystals, *datasheet - BC400, BC404, BC408, BC412, BC416 Premium Plastic Scintillators*, 01/2005. `http://www.detectors.saint-gobain.com`

[Berg02] Christoph Berger, *Elementarteilchenphysik*, 2002, ISBN 978-3540231431

[Berg03] Christoph Berger, lecture *Experimentalphysik 4*, 2003

[Bern05] Werner Bernreuther, lecture *Quantenfeldtheorie I* (quantum field theory), 2005

[BNL07] The E821 Muon (g-2) Home Page, `http://www.g-2.bnl.gov`

[Böh89] Albrecht Böhm et al. *drift velocity monitoring for the L3 experiment* [Tav89, Göt91]

[Bru07] Michael Brunzel, 2007. III. Physikalisches Institut A, RWTH Aachen

[Buz01] P. Buzhan, B. Dolgoshein et al, *The Advanced Study of Silicon Photomultiplier*, 2001. `http://www.slac.stanford.edu/pubs/icfa/fall01/paper3/paper3.pdf`

[Caen05] Caen, *TDC MOD. V767 128 CH. GENERAL PURPOSE MULTIHIT TDC*. `http://www.caen.it/nuclear/printable.php?mod=V767&fam=vme&fun=tdc`

[Caen07] Caen, *datasheets*. `http://www.caen.it/nuclear/products.php`

[CER07] CERN webpage. *document server*. `http://www.cern.ch`

[COS06] Cosmol multiphysics. `http://www.cosmol.com`

[Cow98] Glen Cowan, *Statistical Data Analysis*, Oxford Science Publications, 1998, ISBN 9780198501558

Bibliography

[Dal07] Dallas, *DS18S20 temperature sensor with direct digital output.* `http://www.produktinfo.conrad.com/datenblaetter/175000-199999/176168-da-01-en-DS_1820_1820S.pdf`

[Dem05a] Wolfgang Demtröder, *Experimentalphysik I*, 4. Auflage, 2005, ISBN 978-3540260349

[Dem05b] Wolfgang Demtröder, *Experimentalphysik III*, 3. Auflage, 1998, ISBN 978-3540214731

[Dem06] Wolfgang Demtröder, *Experimentalphysik II*, 4. Auflage, 2006, ISBN 978-354033794

[Fey87] R.P. Feynman. *Vorlesungen über Physik,* Oldenburg, München 1987

[Flu07] Fluke 8846A 6,5-Digits precision multimeter, `http://www.fluke.com`

[Gar05] *Garfield - simulation of gaseous detectors.* `http://garfield.web.cern.ch/garfield`

[Goe87] Johann Wolfgang von Goethe, *Faust*, Weimarer Ausgabe, 1887

[Göt91] Peter Göttlicher. *Entwicklung und Bau eines rechnergesteuerten Gassystems für die Spurkammer des L3-Experiments.* PhD thesis. III. Phys. Inst. A, RWTH Aachen, November 1991

[Gro06] Josef Grooten, 2007. III. Physikalisches Institut A, RWTH Aachen, *private communication*

[Hal84] Halzen & Martin, *Quarks and Leptons*, 1984, ISBN 978-0471887416

[Ham07] Hamamatsu (photonics), *datasheets*, 2005, `http://www.hamamatsu.com`

[Her91] Ulrich Herten. *Hochauflösende Driftkammern.* PhD thesis. III. Phys. Inst. A, RWTH Aachen, February 1991

[Hil07] Günther Hilgers, 2007. III. Physikalisches Institut A, RWTH Aachen, *private communication*

[I3A82] 3. Physikalisches Institut, 1982. *self development by Günther Hilgers et al.*

[I3A07] 3. Physikalisches Institut, 2007. *self development by Günther Hilgers et al.*

[Kle05] Kleinknecht, *Teilchendetektoren*, 4. Auflage, 2005, ISBN 978-3835100589

[Kra05] Manfred Krammer, lecture *Detektoren in der Hochenergiephysik*, SS 2005, Institut der Hochenergiephysik der ÖW, Wien

[Krohne07] Krohne, `http://krohne-mar.com`

[Kul03] Hans-Jörg Kull, lecture *Theoretische Physik I* (mechanics), 2003. `http://llp.ilt.fhg.de/skripten/mechanik050503.pdf`

[Kul06] Hans-Jörg Kull, lecture *Theoretische Physik II* (electrodynamics), 2006. `http://llp.ilt.fhg.de/skripten/ed06/ed_profile.pdf`

[Lam07] Rainer Lampe, 2007. III. Physikalisches Institut A, RWTH Aachen, *private communication*

[LHB07] *LHCb - A High Energy Physics Experiment Studying CP Violation at CERN's Large Hadron Collider.* `http://lhcb-public.web.cern.ch/lhcb-public`

[LHC07] *LHC - THE LARGE Hadron Collider Project.* `http://lhc.web.cern.ch/lhc`

[Mag02] Magboltz2, a plug in program for Garfield which simulatates drift velocities in gas mixtures, `Nucl. Instr. and Meth. A421 (1999) 234-240.`

[Mün06] Astrid Münnich, 2006. III. Physikalisches Institut B, RWTH Aachen, *magboltz script for computing drift velocities*

[MUO97] CMS Collaboration. *The Muon Project - Technical Design Report.* CERN/L-HCC 97-32, December 1997. `http://cms.cern.ch/iCMS/jsp/page.jsp?mode=cms&action=url&urlkey=CMS_TDRS`

[Orb97] Orbissphere, *Orbissphere 3600 $O_2-content device$*, 1997, `http://www.orbisphere.com`

[PDG06] Particle Data Group. *Review of particle physics*, W-M Yao et al 2006 J. Phys. G: Nucl. Part. Phys. **33** l

[Pho06] Photonique SA - Advanced Solutions in Photon Detections, *datasheets*, `http://www.photonique.ch`

[Poo06] Oliver Pooth, 2007. III. Physikalisches Institut A, RWTH Aachen, *private communication*

[PTB04] Physikalisch Technische Bundesanstalt, *german law of units based on [SI06]* . `www.ptb.de/de/publikationen/download/si_v1.pdf`

[PTD06] CMS Collaboration. *CMS Physics - Technical Design Report.* Volume 1: Detector performance and software. `http://doc.cern.ch//archive/electronic/cern/preprints/lhcc/public/lhcc-2006-001.pdf`

[Raab07] Natascha Raab, Bernd Reinhld, 2007. III. Physikalisches Institut B, RWTH Aachen.

[Reb04] Eckhard Rebhan, *Theoretische Physik II*, 2004, ISBN 978-3827402479

[Rei07] Hans Reithler, 2007. III. Physikalisches Institut A, RWTH Aachen. *private communication*

[Roo97] R. Brun and F. Rademakers. *Root - An object oriented data analysis framework. Nucl. Instr. and Meth. A, 389:81-86,* 1997

[Rop07] Gregorio Roper-Yearswood, 2007. I. Physikalisches Institut B, RWTH Aachen, *private communication*

[RWTH06] Rheinisch-Westfälische Technische Hochschule Aachen, *whether station.* `http://www.klimageo.rwth-aachen.de/wtst/timecheck.php`

[Saint06] Saint-Gobain Crystals. `http://www.bicron.com`

[Saul77] F. Sauli. *Principles of Operation of Multiwire Proportional and Drift Chambers.*, CERN 77-09, 1977.

Bibliography

[Sas90] Manfred Sassowsky, *Überwachung von Driftkammergasen mit einer Testkammer*, September 1990. Diploma Thesis, III. Phys. Inst. A, RWTH Aachen.

[Scha04] Stefan Schael, *Eur Phys J C 333, s01, s194-s166*, 2004. `http://www.springerlink.com/content/ha9809wl8jaaa4h9/fulltext.pdf`

[Schm95] Peter Schmüser, *Feynman Graphen und Eichtheorien für Experimentalphysiker*, 1995. ISBN 978-3540584865

[Scho04] Ulrich Schollwök, lecture *Theotische Physik III* (quantum mechanic), 2004

[Seg90] E. Segre, *Experimental Nuclear Physics, Vol. I, S. 252 ff.*, 1990

[SI06] Bureau International des Poids et Mesures *The international system of Units (SI) - 8. edition*, 2006. `http://www.bipm.fr/utils/common/pdf/si_brochure_8_en.pdf`

[Sowa03] Michael Sowa, *Aufbau, Kalibration und Anwendung einer Messapparatur zur Überwachung des Gasdrucks in den CMS-Myonkammern*, Jan 2003. Diploma Thesis, III. Phys. Inst. A, RWTH Aachen.

[Sowa06] Michael Sowa, 2007. III. Physikalisches Institut A, RWTH Aachen,

[SUR02] Cristian Autermann, *C++-program "surface"*, program used for testing HV robustness of barrel muon chambers in Aachen

[SZC04] Henry Szczesny, 2004. III. Physikalisches Institut A, RWTH Aachen,

[Tav89] Andrea Tavenrath, *Bau einer Driftkammer zur Überwachung der Gasqualität in der L3-Vertexkammer*, April 1989. Diploma Thesis, III. Phys. Inst. A, RWTH Aachen.

[Tek96] Tektronix *Benutzerhandbuch - Digitalisierungsoszilloskope TDS 500B, 6000B und TDS 700A*, 1996. `http://www.tektronix.com`

[Tsi06] Oleg Tsigenov, 2007. III. Physikalisches Institut A, RWTH Aachen, *private communication*

[Wik07] *Wikipedia, the free encyclopedia*, 2007. `http://www.wikipedia.org`

[Zha94] T. Zhao et al.; Nucl. Instr. and Meth. in Phys. Research A349(1994) 485-490

[Zil07] Gyula Zilizi, Univerity of Debrecen, 2007. *private communication*

Acknowledgments / Danksagung

First of all I would like to thank Professor Hebbeker for giving me the opportunity to work in such a huge collaboration as CMS is and to be a part of one of the biggest experiments in the world.
Also thanks to him and Professor Wiebusch for being my first and second referee of this diploma thesis.

A great thanks goes to my brilliant supervisor, with whom I had the opportunity to work, to talk, to discuss with most clearly ends and to take place in a lot of small meetings. He tried to teach my as much as possible about measurement procedures, planning details, data analyzing and administrative details: Dr. Hans Reithler.

The subject of my thesis was the further development of a drift chamber, which design was originally from the VDC of the L3 experiment of LEP. Therefore thanks to Professor Böhm. Also thanks to Dipl.-Phys. Georg Altenhöfer for development of the CMS VDC and optimizing the electric field. By the way thanks to Georges Charpak for the development of the multi wire proportional chamber, the groundwork for today's gas detectors.

Ebenso vielen Dank an Dipl.-Ing. Barthel Philipps für die Planung von vielen Details der VDC und für die Anfertigung der Konstruktionspläne und natürlich an die eigentlichen Hersteller, Mechanikermeister Josef Grooten und Mechaniker Ralf Kupper. An Herr Grooten einen besonderen Dank für das Zusammensetzen der Kammer und die vielen Verbesserungen am Prototypen. (Wie oft musste er auseinander nehmen und wieder zusammensetzen?) Er war außerdem die „richtige" Person für die immense Arbeit bei der Entwicklung einer Auslese basierend of Fotodioden und ein idealer Ansprechpartner, um über mechanische Details und Verwirklichungsmöglichkeiten[1] zu reden. Auch an Mechaniker Hans Frohn vielen Dank für die vielen Zuarbeitungen bei vielen Teilen der VDC und die ständige Versorgung mit Gas für meine Messungen.

Eine mechanisch noch so gute Kammer wäre ohne entsprechende Elektronik leider nur ein Ausstellungsstück. Deshalb vielen Dank an alle Elektrotechniker, Elektroniker und Techniker des Institutes. An Betr.-Ing. Günther Hilgers vielen Dank für die Beratung bei vielen Details der Kammer, der Erprobung der Anwendbarkeit von Fotodioden und die Arbeit an der noch laufenden Entwicklung von neuen, sicherlich hervorragend werdenden, VME-Modulen. Zusätzlich möchte ich mich für die vielen ausgiebigen Erklärungen über elektronische Schaltungen, Bauteile und Arbeitsweisen bedanken. Er hat sich dabei immer genauso so viel Mühe gegeben wie mit jedem seiner vielen Auszubildenden.
An Techniker Franz Adamczyk ein Dankeschön für die große Unterstützung bei elektronischen Messungen und Tests im Labor, die fast 7-mal-24h-Verfügbarkeit, die unzähligen Umbauten bei

---

[1]„Alles ist möglich, es ist nur eine Frage des Aufwands."